Multi-Material Discrimination Using Photon Counting Spectral Computed Tomography

by
Nathaniel Raymond Fredette

A dissertation submitted to the Department of Biomedical Engineering,

College of Engineering

in partial fulfillment of the requirements for the degree of

Doctor of Philosophy
in Biomedical Engineering

Chair of Committee: Mini Das

Committee Member: Howard Gifford

Committee Member: Yingchun Zhang

Committee Member: Nuri Ince

Committee Member: Thomas Hebert

University of Houston
August 2020

DEDICATION/EPIGRAPH

Many of life's failures are people who did not realize how close they were to success when they gave up.

Thomas A. Edison

ACKNOWLEDGMENTS

First of all I would like to extend my gratitude to my Ph.D. adviser, Dr. Mini Das, whose continued support and wealth of research ideas were pivotal to the completion of my degree. I would like to thank her for providing opportunities for career growth by encouraging me to attend numerous conferences and networking events. Finally, I would like to acknowledge her funding sources (NIH, NSF and DOD) without which this work would not have been possible.

Next, I would like to acknowledge my committee for their commitment to reviewing my work and fruitful discussions. I would like to specifically thank Dr. Howard Gifford for interesting topical discussions at UH and at conferences and for his help providing an understanding of the basics of statistics and medical imaging through coursework. I would also like to thank Dr. Yingchun Zhang and Dr. Nuri Ince for their insight into signal and image processing and general availability for meetings. Finally, I would like to thank Dr. Thomas Hebert for serving as my out-of-department committee member and for his insightful comments during my prospectus and defense.

I would like to also acknowledge our collaborators in Dr. Chandra Mohan's laboratory at the University of Houston. Dr. Mohan and Yanping Chen's knowledge of working with mice was instrumental in the culmination of my work with a practical real-world application of a method for the diagnosis of arthritis and possible monitoring of treatment response.

Finally, I would like to acknowledge my family for their support during this journey. Particularly, I appreciate the interest of my mother, Denise Fredette, in my work and the discussions we had when I encountered challenges along the way. I am grateful for the financial support that I received from my mother and father, Mark Fredette, during my time as a doctoral student. I would also like to extend my gratitude to my sister, Jackie Fredette, for fruitful discussions about projects and her general generosity with her time.

ABSTRACT

Quantitative volumetric mapping of multiple materials with spectral computed tomography (CT) has applications in many areas including biomedical imaging, defense and security, geophysical imaging of rock composition and in materials and chemical imaging. Dual or multi-kVp x-ray exposure when using an energy-integrating detector has been proposed and demonstrated in the past for biomedical imaging. X-ray dose and imaging time, along with insufficient spectral separation, limits dual and multi-kVp applications and their ability for accurate quantitation. When using photon-counting spectral detectors (PCDs), some of these limitations can be overcome. However, low dose and computationally efficient mechanisms to yield volumetric maps of more than two or three materials remain as a significant challenge. Recently, our group has proposed a multi-step method for virtual discernment between the materials of an object termed material decomposition for short. Experimental implementation of this method adds new challenges including reliable detector spectral corrections. This work presents initial simulation studies, experimental validation and detailed methods to successfully implement this multi-material decomposition technique. Here we show examples with virtual separation of up to six materials in simulations and five materials in experiments on our benchtop spectral CT system. For comparison, a conventional single-step decomposition was also performed on the same synthetic and experimental data. Results show a significant reduction in decomposition errors with low noise over the single-step approach. Finally, a biological specimen of a chicken heart was injected with tantalum and gadolinium (likely candidate contrast agent materials) and multi-step decomposition was also successfully conducted on this sample. These studies offer validations required for robust utility of the method in imaging applications requiring separation of multiple materials.

TABLE OF CONTENTS

LIST OF TABLES

LIST OF FIGURES

Chapter 1

Introduction

The focus of this work is using multi-energy computed tomography acquired with a photon counting detector to virtually separate materials within the imaged object. In Chap. 2, some background on x-ray image formation and x-ray interactions is presented. Chapter 3 describes the major technology that permits spectral x-ray measurements of photon counting detectors with a focus on the Medipix3RX detector. After that, in Chap. 4 we will discuss some basics of computed tomography with PCDs. In Chap. 5, the specifics of the process of virtual discernment and quantification of materials within the imaged object from spectral CT measurements or material decomposition is presented. In the following chapter (Chap. 6) our novel multi-step approach to material decomposition is discussed with results of simulated multi-material phantoms decomposed with both the multi-step method and a conventional single-step approach to explore the new method. Experimental validation of the technique is presented in Chap. 7 with various multi-material and biological samples. Finally, concluding remarks are summarized in Chap. 8.

Chapter 2

Fundamentals of Medical X-ray Imaging

2.1 General Description

X-ray imaging is one of the oldest medical imaging modalities with its origin dating back to December 22, 1895 when Wilhelm Roentgen took the first single-projection radiograph of his wife's hand. X-ray imaging took another huge leap forward with the advent of computed tomography (where multiple radiographs are acquired at various angles around the sample) in 1971 when Godfrey Houndsfield and his team imaged a woman with a suspected brain tumor with an early CT scanner design. Since then x-ray has been widely adopted as a non-invasive imaging method due to its high penetrating power, relatively low cost, short imaging and processing times, portability and high resolution [87]. Many advances in x-ray source and detector technologies as well as software-based image processing algorithms continue to improve this imaging modality, but the governing physics behind x-ray image formation remains the same. The succeeding sections will serve as a review of some x-ray imaging fundamentals.

2.2 Beer's Law

The governing material property for x-ray imaging is x-ray attenuation. X-ray attenuation is the sum of all x-ray interactions with matter that result in the removal of photons from the incident beam. Different materials respond to x-ray differently and thus, have

different x-ray attenuations. The attenuation of a material is also energy-dependent as generally materials block low energy x-rays with higher probability than high energy x-rays. Thicker objects block more x-rays than thinner objects of the same material. Since medical x-rays generally interact with bound electrons, materials with higher atomic numbers, as well as higher densities, produce higher x-ray attenuation. The process of x-ray image formation is governed by Beer's law, as seen in

$$I(E,\vec{r}) = I_0(E,\vec{r})e^{-\int \mu(E,\vec{r})dl}, \tag{2.1}$$

where the transmitted number of photons, $I(E,\vec{r})$, is equal to the incident number of photons, $I_0(E,\vec{r})$, reduced exponentially by the negative line integral of the object attenuation, $\mu(E,\vec{r})$. The object attenuation is the sum of the probabilities of all x-ray interactions with the material. In Eqn. 2.1, E represents the energy of the beam and $\vec{r}$ is the spatial variable.

2.3 Medical X-ray Physics

Four primary interaction mechanisms can occur when an x-ray passes through matter at the medically relevant range of energies (≈20-150 keV) [86]. The first is that the x-ray passes through the object with no interaction. This can be seen in Fig. 2.1(a). The second is photoelectric absorption where a photon collides with a tightly bound electron and is fully absorbed. In this process, the electron is ejected from the atom with kinetic energy equal to the difference in energy between the photon energy and the binding energy of the inner shell electron leaving a vacancy in the inner shell. This electron vacancy is filled by an outer shell electron. In this process, the excess energy possessed by the outer shell electron is released in the form of a secondary photon with energy equal to the difference in binding energy between the inner and outer shells [Fig. 2.1(b)]. In photoelectric absorption, the incident photon must have energy greater than or equal to the binding energy of the electron for the photoelectric effect to occur. When the photon energy is equal to the binding energy of the electron, photoabsorption becomes feasible and a sharp increase in

the material attenuation can be noticed. As the photon energy increases beyond this binding energy, the probability of photoelectric absorption decreases. The term K-edge represents the sharp increase in the absorption cross section when photon interaction with a K-shell electron becomes possible. Similarly, the L-edge represents the jog in the attenuation curve when photoabsorption with a L-shell electron is plausible. The electron binding energies are different for different materials because of their different atomic numbers or the number of protons and electrons in the atom. More massive atoms have stronger atomic forces between inner shell electrons and protons than smaller atoms. Elements of the periodic table form a spectrum of different K-shell and L-shell binding energies and some (like iodine, barium, gadolinium, etc.) fall in the medical imaging range of energies. The third x-ray interaction is Rayleigh or coherent scattering where the incident photon interacts with an atom of the object causing it to become excited. This excess energy of the atom is immediately released in the form of an emitted photon with the same energy as the initial photon with only a small change in direction as seen in Fig. 2.1(c). The fourth x-ray interaction is Compton or incoherent scattering. In this process, a photon collides with a loosely bound electron (which is considered free or unbound) of an atom, but only transfers some of its energy to the electron. The photon is deflected from its original direction by some angle, as described by

$$E_{\gamma'} = \frac{E_\gamma}{1 + (E_\gamma / m_e c^2)(1 - \cos(\theta))}, \tag{2.2}$$

where the energy of the scattered photon, $E_{\gamma'}$, depends on its energy before scattering, E_γ, and the scattering angle, θ. In Eqn. 2.2, $m_e c^2$ represents the rest mass of an electron of 511 keV. The interacting electron is also redirected at some other angle, ϕ [Fig. 2.1(d)]. The photon can be scattered in any direction, but the recoil electron can only be forward directed. As explained by Eqn. 2.2, low energy photons are preferentially backscattered, mid energy photons are isotropically scattered and high energy photons are more likely to be forward scattered. At low energies, most of the energy remains with the scattered photon, but as energy increases more energy is transferred to the recoil electron. Since Compton scattering occurs between photons and free electrons, the likelihood of the interaction is

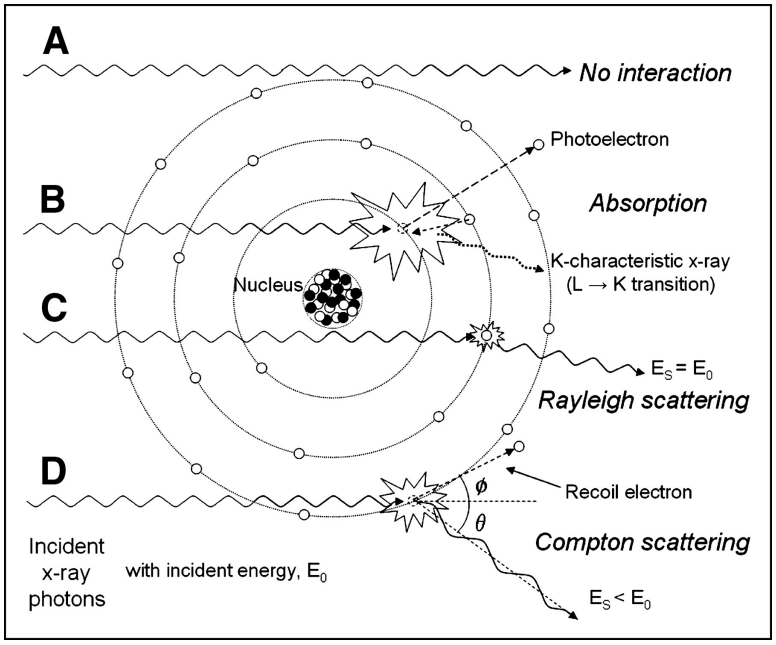

Figure 2.1: X-ray interactions with matter at medically relevant energies. This figure was taken from [77].

proportional to the electron density of the material.

The x-ray attenuation is then described by

$$\mu = \tau + \sigma_R + \sigma, \tag{2.3}$$

where τ is the photoelectric cross section, σ_R is the Rayleigh scattering cross section and σ is the Compton scattering cross section with units of inverse length. Eqn. 2.3 describes a material's x-ray attenuation in the medical imaging range of energies. There exist more interactions for photons of energies outside this range that also contribute to x-ray attenuation, but these are ignored here for simplicity.

The predominant interactions in the medical imaging range of energies are photoelectric absorption and Compton scattering (Fig. 2.2) for two materials of interest for medical imaging of water and iodine. Notice the K-edge discontinuity of iodine at 33.2 keV. It can be seen here that Rayleigh scattering only contributes to a small fraction of the total mass attenuation and therefore, is often ignored. At low energies, the total attenuation cross section is dominated by photoelectric absorption and at high energies the attenuation cross

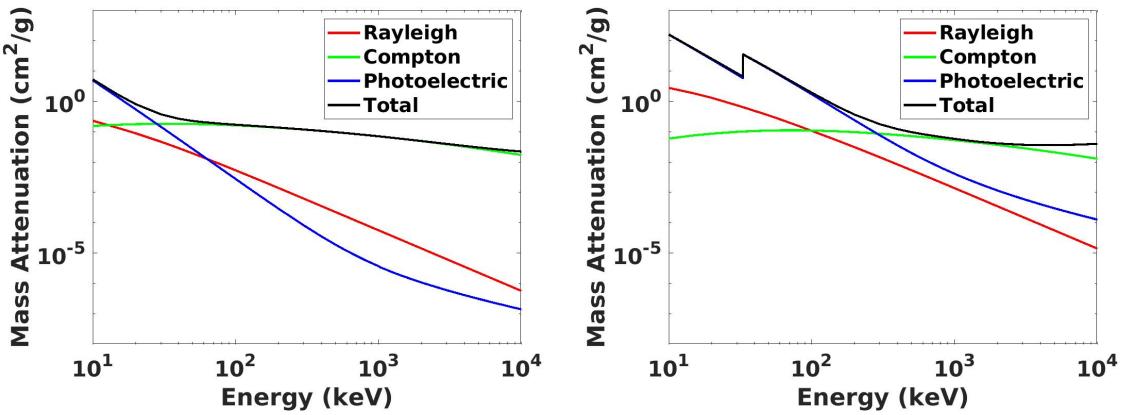

Figure 2.2: Energy distributions of medical x-ray interactions in mass attenuation [cm^2/g] for (a) water and (b) iodine.

section is dominated by Compton scattering. As we can seen here, the contributions from both effects are different for different materials.

2.4 Challenges in Medical X-ray Imaging

One major challenge in conventional medical imaging is poor soft tissue contrast. The various soft tissue-like materials of fat, water, breast and even cancer all possess x-ray attenuations with similar magnitudes (Fig. 2.3). This makes differentiating between these tissues rather challenging and leads to the reason why contrast agents are used. Contrast agents such as iodine possess drastically different x-ray attenuations from soft tissues making them easily identifiable when introduced to the body. Another approach involves making use of the refractive properties of tissues rather than only their attenuation referred to as phase contrast imaging. Phase sensitive x-ray imaging benefits from higher soft tissue contrast because the real part of the refractive index which governs phase contrast imaging is several orders of magnitude greater than the imaginary part which governs attenuation contrast imaging.

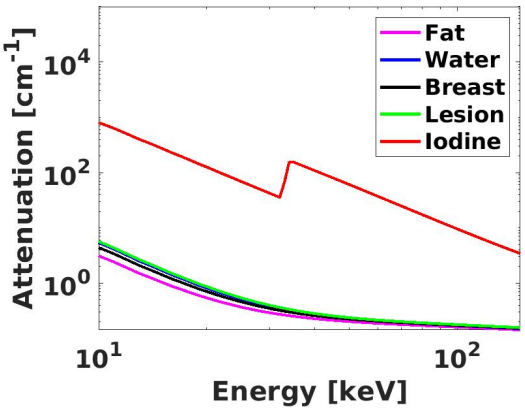

Figure 2.3: Energy-dependent linear attenuation curves for more materials of interest in medical imaging.

2.5 Chapter Summary

To review this chapter, the relationship describing image formation, Beer's Law, that relates the image of the photons exiting the object to the image of the photons entering the object was described. Some basic medical x-ray physics was also presented with a focus on the interactions that dominate at medical imaging energies of photoelectric absorption and Compton scattering. The x-ray material property, attenuation, was described as the summation of all x-ray interactions. The chapter concluded with a short discussion on one major challenge with conventional medical x-ray imaging of poor soft tissue contrast.

Chapter 3

Photon Counting Detectors (PCDs)

3.1 Current Detection Technologies Available in Clinics

X-ray detectors can be classified based on how they convert photons into a measurable signal. This process can be described as indirect and direct detection. As the photon impinges on an indirect conversion system, its energy is first converted into visible light via a segmented scintillating crystal and then that light is measured by a light sensitive device such as a photodiode. The amount of light generated in the scintillator is proportional to the incident photon energy. In direct detection, the photon interacts in a semiconductor material freeing electrons from atoms which migrate to the anode under an external voltage bias. The movement of the charges within the crystal causes a measurable current to be produced at the electrodes. Clinical x-ray detectors can be either indirect (gadolinium oxysulfide or cesium iodine scintillators) or direct (amorphous selenium).

X-ray detectors can also be distinguished by how they process the electrical signal created by the photodiode or the migration of the charge within the semiconductor. In energy-integrating systems, the detected signal is integrated over the full time of the x-ray exposure. In this case, the energy information of the photons is lost in the integration process. The electrical signal is also proportional to the energy of the incoming photon, so higher energy photons are given more weight that lower energy photons. Dark current noise is integrated into the signal limiting the dynamic range and signal to noise ratio (SNR) of the imaging system. One benefit however, is that energy integrating systems can operate in high flux

conditions typical of clinics where imaging time is of great concern.

3.2 General Description of PCDs

Photon counting detectors (PCDs) are a relatively new technology that permit the collection of not only spatial x-ray distributions, but also capture spectral information. In photon counting systems, the electrical output of each photon is counted individually. The electrical circuit is comprised of a pulse shaping amplifier followed by a group of discriminators and counters. When a signal is processed by the amplifier, the resulting pulse height is proportional to the initial x-ray energy. This pulse is then compared with an electronic threshold specified by the user in the discriminator to determine if a count is recorded. The counter is then incremented if the pulse height is above said threshold and otherwise it is not. Traditionally, clinical x-ray detectors are energy integrating detectors although some prototype photon counting systems are becoming available. Therefore, energy discrimination is only possible through dual energy approaches such as kVp switching, dual-layer detectors, dual sources or source filtering which suffer from challenges such as incomplete spectral separation or the need for additional hardware or software [60]. Photon counting systems overcome some of these challenges and allow for energy selective measurements which make them an attractive next generation of medical imaging devices. Current fabrication techniques limit the ability to grow large semiconductor crystals with high atomic numbers, so the size of today's PCDs can be rather small. However, tiling several smaller detectors in a strip or array is being investigated to increase the field of view of these PCDs [42]. Raster scanning and image stitching is commonly employed to generate larger field of view images. The multi-energy information collected from PCDs has many applications such as K-edge subtraction imaging [78, 79, 102, 73, 90], phase contrast imaging [88, 20] and phase retrieval [38, 21, 92] and material decomposition [49, 50, 51, 1, 64, 56, 98, 24, 32]. This dissertation will focus one application of photon counting detectors of material decomposition using the Medipix3RX line of photon counting detectors developed at CERN (Geneva, Switzerland).

Figure 3.1: Picture of the Medipix chip and sensor [11].

3.3 Medipix3RX

The Medipix3RX detector consists of a semiconductor active layer bump-bonded to the Medipix3RX application specific integrated circuit (ASIC). A picture of a Medipix3RX detector is shown in Fig. 3.1. As a photon impinges on the semiconductor, electrons are dislodged from the semiconductor lattice creating clouds of electrons and holes where the number of electron-hole pairs generated is proportional to the incident photon energy. Under an electric field created by an external voltage bias, the electrons and holes migrate to the opposite electrodes (Fig. 3.2). As these charges migrate, a measurable voltage pulse is created within the sensor that is compared with a preset threshold to determine whether a count is recorded. The Medipix3RX photon counting detector operates by totaling all photon interactions within the sensor which produce a measurable voltage greater than this preset threshold, as described in

$$I^{int}(E_j) = \int_{E_j}^{\mathrm{kVp}} \Phi(E) D(E) dE, \tag{3.1}$$

where $I^{int}(E_j)$ is the total counts over threshold for threshold energy E_j, $\Phi(E)$ is the spectrally dependent incident x-ray flux and $D(E)$ is the detector response function.

However, because the charge spreads out as it drifts within the sensor, these charge

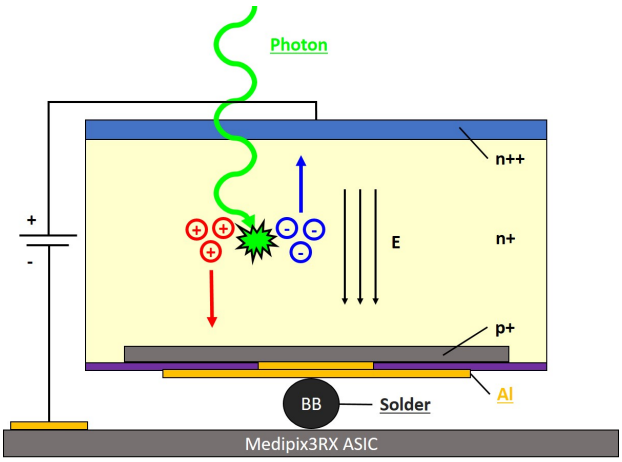

Figure 3.2: Description of PCD physics under x-ray illumination. This figure represents the photon detection process for one photon interacting with one pixel.

clouds can spill over into multiple pixels. This problem is referred to as charge sharing and is left uncorrected in the legacy mode of operation of the Medipix detector of single pixel mode (SPM). New to the Medipix3RX detector is charge summing mode (CSM) which provides a hardware level algorithmic correction for charge sharing where simultaneous counts in neighboring pixels (originating from the same single incident photon) are compared and the total charge is allocated to the primary pixel [4]. Figure 3.3 displays three scenarios where an incident photon with energy of 100 keV interacts at the junction between pixels of the Medipix3RX detector in SPM and CSM. The threshold is set to 20 keV in (a), 40 keV in (b) and 60 keV in (c). As can be seen in the figure, in scenario (a), SPM records a count in three pixels with energies of 25 keV, 30 keV and 50 keV from the same original single photon. In this scenario in CSM, the arrival time between the multiple events is recognized as one event and all of the charge is allocated to the pixel with the greatest fraction. In scenario (b), the threshold is increased to 40 keV so only one pixel receives a count of 50 keV in SPM. The full charge and energy are correctly assigned to the primary pixel in CSM in case (b) as well. Finally, in scenario (c) the threshold is increased to 60 keV so no counts are recorded in SPM because the fraction of charge received in any one pixel does not exceed 60 keV. However, in CSM the primary pixel still receives a count because the total charge exceeds 60 keV and it is assigned to the primary pixel.

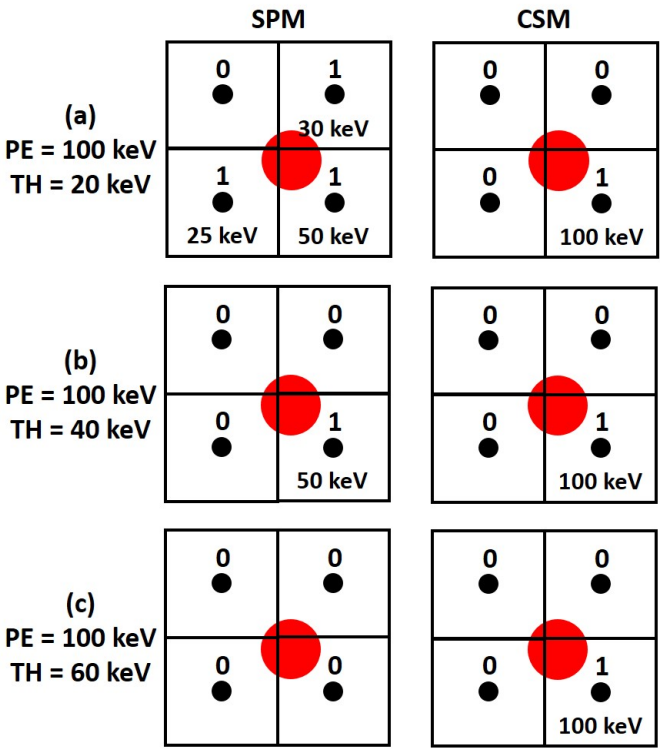

Figure 3.3: Depiction of the charge summing logic implemented in Medipix3RX detector.

Both of the Medipix detectors considered here possess 55 μm bump-bonding or the semiconductor is physically connected to the ASIC at 55 μm pixel pitch. In addition to SPM and CSM, the detector can also be operated in either fine pitch mode (FPM) or spectroscopic or color mode (CM). In FPM, all pixels are actively connected to the ASIC with 55 μm pixel pitch and each pixel has two thresholds. In CM, pixels are grouped in fours such that sensor is connected to the ASIC with 110 μm pixel pitch, but all eight thresholds from the four pixels of the group are available for multi-energy measurement. The discussed Medipix operation modes lead to four combinations of SPM-FPM, SPM-CM, CSM-FPM and CSM-CM. More thresholds are available in SPM than CSM because half of these discriminators are dedicated to the inter-pixel communication logic in CSM. In this dissertation, we use two detectors of a Medipix3RX detector with a 675 μm thick silicon sensor and a WidePix detector comprised of a row of 5 Medipix3RX chips with 1 mm thick cadmium telluride sensors. We operate these detectors in various modes of SPM-FPM, SPM-CM and CSM-FPM. In Sec. 3.7, we will discuss a spectral correction technique

that can correct for spectral distortions such as charge sharing. This correction method is universal and can be applied to data collected in all modes of operation.

3.4 Spectral Image Quality

With the energy-resolving capability of photon counting detectors, image quality can now be analyzed not only spatially, but also along the energy dimension. Here we present modulation transfer function (MTF) curves for various threshold energies of (a) 10 keV, (b) 20 keV, (c) 30 keV, (d) 40 keV, (e) 50 keV and (f) 60 keV [Fig. 3.4]. The MTF represent the response of the imaging system to different spatial frequencies. It is generally Gaussian shaped with largest values for zero frequency and smaller values for higher frequencies. It can also be thought of as the amount of blurring introduced by an imaging system. An imaging system with a sharp, narrow MTF will introduce more image blurring than an imaging system with a broad, wide MTF. The MTFs calculated here were computed using the tilted opaque edge method as described in [72]. A steel knife ($\approx$1 mm thick) was placed in the beam 86 cm from the source and 2 cm from the detector and tilted at a 10° angle with respect to the detector pixel columns. Two collimators were placed in the beam to reduce scatter. The image of the edge was flat field corrected and then reprojected along the edge direction to obtain a pre-sampled edge spread function (ESF). The ESF was then fit with a logistic function which has an analytical derivative [53]. The derivative of the logistic function was calculated to obtain the line spread function (LSF). Finally, the fast Fourier transform (FFT) of the LSF was computed and normalized by the DC component to obtain the MTF. These calculations are conducted for two detectors of the 675 μm thick silicon detector operated in SPM-FPM and the WidePix detector with 1 mm thick cadmium telluride sensors operated in both SPM-FPM and SPM-CM. The tube peak voltage was set to 80 kVp for the data collected with the silicon detector and 100 kVp for the data collected with the WidePix detector because of the higher absorption efficiency of cadmium telluride at high energies. These experimental conditions are relevant to the multi-material phantom measurements described in Chap. 7.

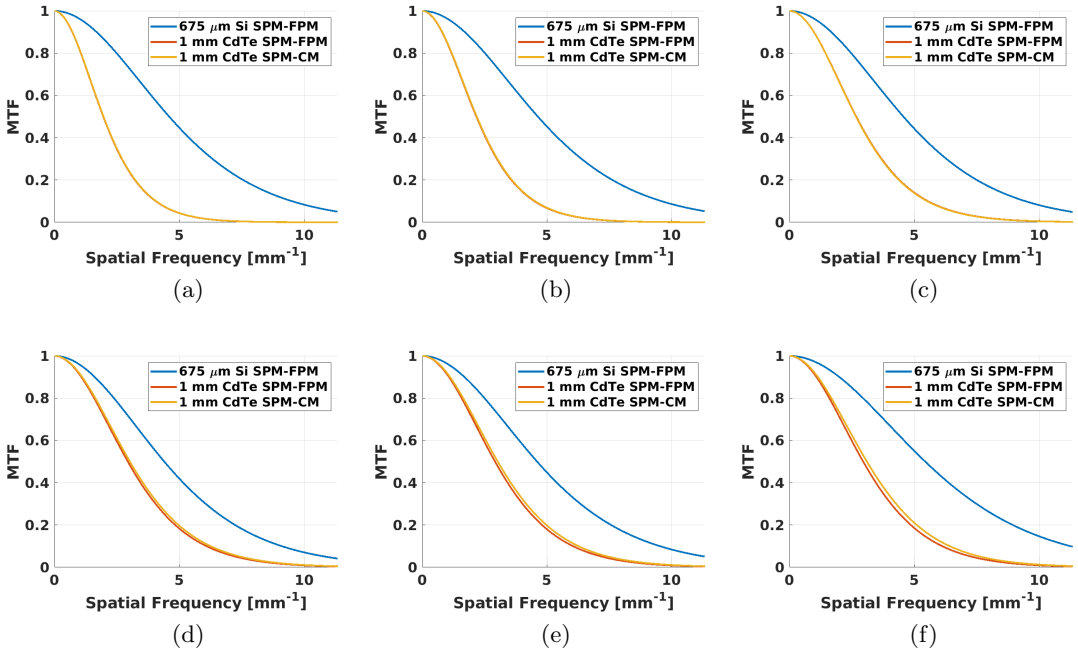

Figure 3.4: Modulation transfer functions for two detectors in two different modes where the threshold energy was set to (a) 10 keV, (b) 20 keV, (c) 30 keV, (d) 40 keV, (e) 50 keV and (f) 60 keV.

A higher spatial resolution is seen for the silicon detector as compared with the cadmium telluride WidePix detector. The sensor fabrication process for silicon is much more mature leading to a much more uniform pixel response across the slab. Cadmium telluride on the other hand suffers from non-uniformities such as zero or bad pixels and sensor polarizations [3] that lead to vein-like structures across the sensor that are time-dependent and difficult to avoid. These spatial non-uniformities degrade the spatial resolution of the cadmium telluride detector. However, we do not see much of a difference in performance in terms of spatial resolution across the two modes of operation of the WidePix detector. Another observation is that spatial resolution improves as the threshold energy is increased. This can be attributed to the fact that less instances of charge sharing (which degrades spatial resolution) are recorded as the threshold energy increases. This effect is more apparent for the cadmium telluride detector because of the fluorescences of cadmium and tellurium which cause additional charge sharing at low energies.

3.5 Energy Calibration

In order to use the detector's spectral capability, a correlation between the detector thresholds and the true particle energy must be obtained. Common techniques for detector energy calibration include x-ray fluorescence [14], K-edge calibration [34] and radioactive source [29] techniques. Here, we use the newly developed DIR method [95], which uses the K-edges of a few metallic foils (Sn [29.2 keV], Nd [43.6 keV], Gd [50.2 keV] and W [69.5 keV]) or the x-ray tube peak voltage to determine the linear relationship between detector threshold and particle energy. This method also requires no system geometry changes as are required in x-ray fluorescence and relaxes the requirement of controlling the x-ray flux as required by Panta [66]. A fine step size threshold scan of these metallic foils along with a flat-field is first obtained with the detector of interest. Adjacent threshold images are then subtracted and flat-field correction is performed for each foil. The average pixel response is calculated by averaging each flat-field corrected image (although pixel-by-pixel calibration is also possible). This one-dimensional normalized counts curve [Fig. 3.5(a)] for each metal is then differentiated to obtain differential intensity ratio (DIR) curves [Fig. 3.5(b)]. Peaks in the DIR curve correspond to the K-edges of the foils and the kVp of the x-ray source. The centroid of each of these peaks can be found by Gaussian fitting and plotted against the known energies of the K-edges of each of the materials. Linear fitting can then be used to obtain the relationship between the incident particle energy and the detector thresholds [Fig. 3.5(c)]. These linear fits can then be used to inform decisions of which thresholds to use for computed tomography measurements of decomposition phantoms as well as which energies to use for material decomposition. The DIR calibration shown here was conducted for threshold number 0, but a similar calibration could be obtained for threshold number 1.

3.6 Energy Resolution

Using the same procedure as in the energy calibration process in Sec. 3.5, the spectral detector energy resolution can be obtained. This energy resolution can be conventionally

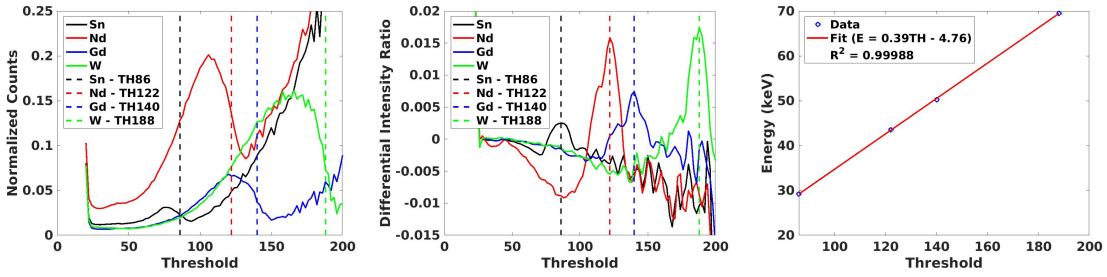

(a) (b) (c)

Figure 3.5: (a) Normalized counts used to calibrate the silicon detector. (b) Differential intensity ratio (DIR) curves used to determine the location of the K-edges. (c) Resulting threshold-to-energy calibration relationship.

obtained through x-ray fluorescence [14], K-edge calibration [34] and radioactive source [29] techniques. But, because we operate the detector in SPM where resolving monochromatic incidences such as in x-ray fluorescence is not possible [48], we opt to again base our calculations on the DIR curves. From the same Gaussian fits used to obtain the centroids of the K-edge peaks, we obtain the full width at half maximum (FWHM) of each of these peaks. These FWHMs can then be plotted against the known K-edge energies of the metallic foils and again fit with a line to obtain detector energy resolution across a range of energies. Here (Fig. 3.6) we present energy resolutions for threshold number 0 of the silicon detector operated in SPM-FPM, threshold number 0 of the cadmium telluride WidePix detector operated in SPM-FPM and threshold number 0 of the cadmium telluride WidePix detector operated in SPM-CM. Similar energy resolutions can be obtained for the other thresholds of these detectors which are not shown. The silicon detector has higher energy resolution than the cadmium telluride detector as expected. The energy resolution is also rather similar across the two modes of the cadmium telluride WidePix detector. The energy resolutions are calculated to be about 12.6 keV at 100 keV, 31.3 keV at 100 keV and 32.4 keV at 100 keV for the silicon, cadmium telluride WidePix in SPM-FPM and cadmium telluride WidePix in SPM-CM, respectively. These energy resolutions may seem rather poor, but since their are only two predominant x-ray interactions in the medically relevant range of energies, only a few energy-resolved measurements are required. Therefore, these energy

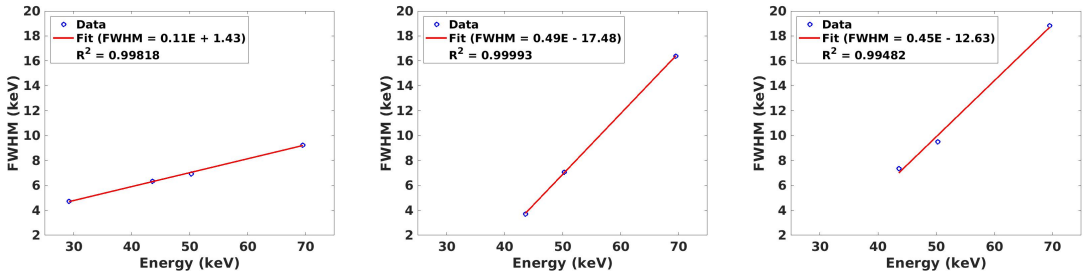

(a) (b) (c)

Figure 3.6: Energy resolution curves for (a) the silicon detector operated in SPM-FPM, (b) the cadmium telluride WidePix detector operated in SPM-FPM and (c) the cadmium telluride WidePix detector operated in SPM-CM.

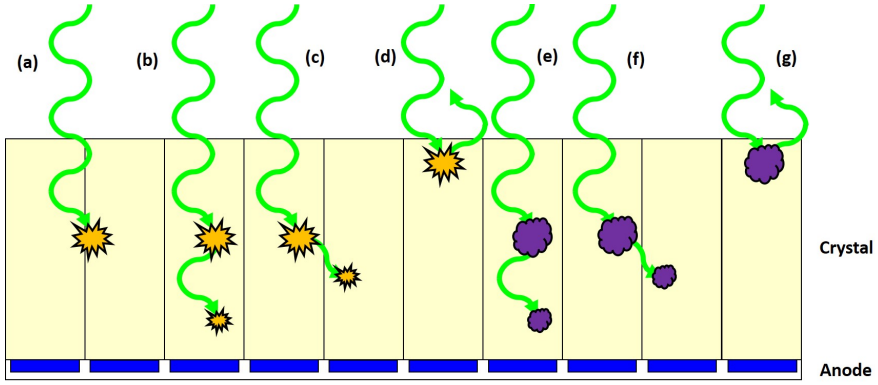

Figure 3.7: Depiction of various cases of charge sharing and incomplete photon energy deposition.

resolutions are acceptable for generating enough energy-resolved measurements with distinct effective energies and minimal noise correlations. Also, we operate the detector in SPM which is known to have poorer energy resolution than CSM. If operated in CSM with this improved energy resolution, energy bins with sharper edges are expected leading to less spectral overlap and better material separation. These energy resolutions will again be discussed in Sec. 7.5 where the results of the five-material decomposition phantoms is presented.

3.7 Spectral Distortions and Correction

Photon counting detectors offer many advantages such as providing spectral information with high spectral resolution, but they also introduce some new challenges in the form of

detector spectral distortions [89]. The first of these distortions is charge sharing, which is caused by the overflow of charge into neighboring pixels as the charge packet drifts within the sensor under the external voltage bias. Several phenomena can cause charge sharing which are depicted in Fig. 3.7 as (a) represents a photon incidence on the boundary between pixels, (b) represents an incidence with a fluorescence event which is absorbed in same pixel, (c) represents an incidence with a fluorescence where the fluorescence photon is absorbed in a neighboring pixel, (d) represent an incidence with a fluorescence where the fluorescence photon escapes the detector, (e) represents an incidence followed by Compton scattering where the scattered photon is absorbed in the primary pixel, (f) represents an incidence followed by Compton scattering where the scattered photon is absorbed in a neighboring pixel and (g) represent an incidence followed by Compton scattering where the scattered photon escapes the detector. In Fig. 3.7, fluorescence events are shown in yellow and Compton scattering events are shown in purple. The photons here represent different energies where the energy of the fluorescence photons matches that of the detector sensor material and the likelihood of Compton scattering increases with increasing energy. The sizes of the yellow explosions or the purple clouds is meant to indicate the energy of the photon as some energy will be lost after a fluorescence or Compton scattering event. Since the size of the charge packet is proportional to the incident x-ray energy, this problem becomes more severe as the incident x-ray energy increases. Other sensor design characteristics such as thickness and pixel dimension also affect the amount of charge sharing. Smaller pixel detectors suffer more from charge sharing than larger pixel detectors as the charge is more likely to spread across the smaller pixels. The same goes for thicker versus thinner sensor detectors as thicker sensors allow the charge to spread out more because the drift lengths are longer on average. Other than design considerations to limit the amount of charge sharing, hardware level algorithmic approaches exist that provide anti-charge sharing logic which can reduce the severity of this problem [48].

The second major detector distortion is pulse pileup where two or more photons arrive at a pixel of the detector within the detector's resolving time. Because the detector is unable to

Table 3.1: Flux rates [$\times 10^6$ photons/mm^2/s] for the multi-material experiments presented as an example.

TH (keV)	675 μm Si SPM-FPM	1 mm CdTe SPM-FPM	1 mm CdTe SPM-CM
8	2.881	48.142	11.970
16	1.779	26.054	6.008
24	0.618	14.677	3.890
32	0.207	7.430	2.126
40	0.070	4.228	1.091
48	0.021	2.403	0.735
56	0.006	1.337	0.305
64	0.001	0.664	0.174

respond to the additional photons during its dead time (≈ 4.2 μs for Medipix3RX detectors with 1 mm cadmium telluride sensors [95]), the pulse generated by these succeeding photons can be combined and misinterpreted by the detector as a single photon of higher energy. This effect is shown schematically in Fig. 3.8 as the pulses generated by two photons close in arrival time are combined into one pulse which is larger in magnitude. Detector technology is continuously evolving to reduce these dead times, but common ways to reduce pulse pileup are to reduce pixel sizes and x-ray flux. Therefore, there exists a trade-off in terms of pixel size between making pixel sizes large enough to reduce charge sharing and making pixel sizes small enough to reduce pulse pileup. Smaller pixel sizes are desired to increase spatial resolution and higher x-ray fluxes are desired to reduce imaging times. With our low flux micro focus x-ray tube (Hamamatsu L12161-07) and the source to detector distances used in our experiments, pulse pileup is usually not a big concern with 2.5×10^4 counts/s/pixel representing the flux for significant pulse pileup for the same 1 mm cadmium telluride detector [95]. Table 3.1 displays some representative detected count rates for some of the experiments conducted in this dissertation. In all cases, the source to detector distance was pretty much the same. The count rates are lower for the silicon detector than the cadmium telluride detector because of its lower absorption efficiency. The tube peak voltage was 80 keV for the silicon measurement and 100 keV for the cadmium telluride measurements. The effective pixel size is 55 μm for the FPM measurements and 110 μm for the CM measurements.

Because of the known spectral distortions introduced by the Medipix detector, a spectral

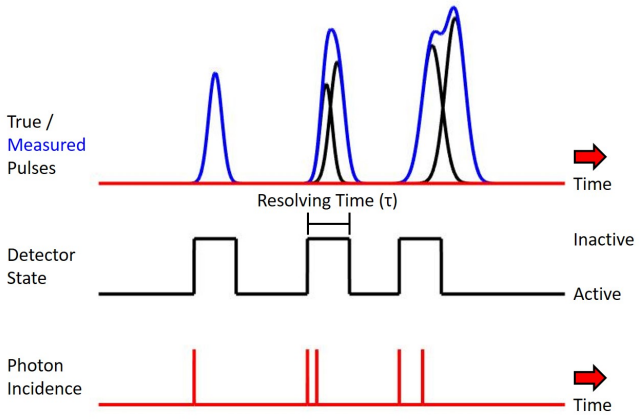

Figure 3.8: Depiction of pulse pileup where multiple photons arrive at the detector within the detector's dead time resulting in the loss of counts.

correction method similar to [22, 23] was implemented. In this previous work, differentiation of the data to create energy bins was first conducted, but in our implementation correlations between experimental and simulated counts were calculated using the raw data. We found that the additional noise due to this subtraction can significantly degrade image quality, because the subtraction of two independent Poisson distributed images yields images with Skellam noise statistics [85]. Simply, the idea is to correct the distorted counts measured by the detector to have more ideal behavior free from distortions. This can be accomplished by exposing the detector to different fluxes (with peak values displayed in Tab. 3.1), simulating the same and then determining the polynomial relationship between the distorted and undistorted counts. It is crucial to accurately model the source spectrum in terms of filtering materials such that the only differences between the simulated and measured spectra are caused by detector distortions and object scatter so that these effects can be isolated. Different fluxes can be achieved by measuring and simulating PMMA slabs of differing thicknesses at the same energies as the CT scans. We use our analytical code which uses Spektr [83] for x-ray spectrum generation, extended ellipsoids with National Institute of Standards and Technology (NIST) x-ray attenuation properties [13, 12] for object modeling and a pixelated semiconductor slab for detector modeling. By simulating the x-ray transmission through these slabs at every keV from 8 to 80 keV and then summing these counts into the threshold projections, we can recreate the measurements without distortions. We

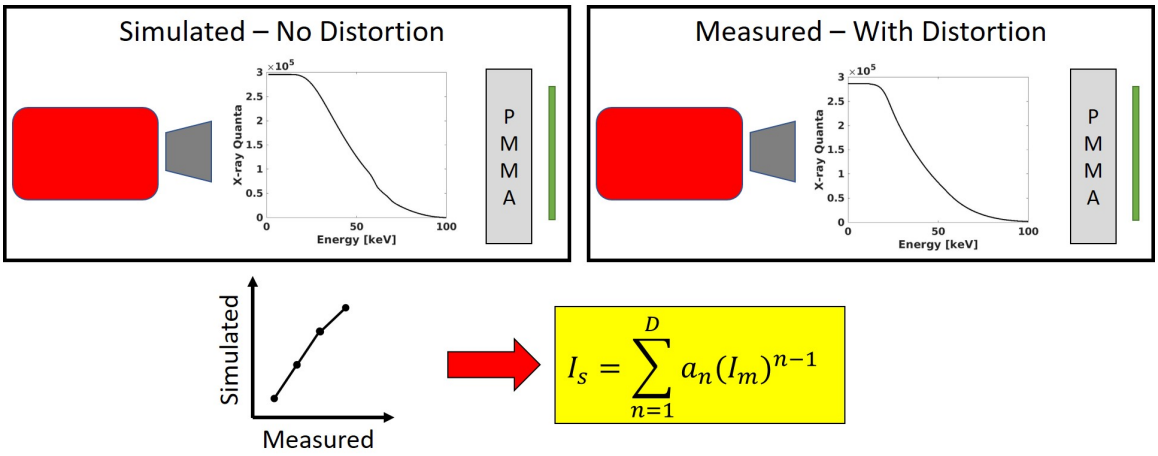

Figure 3.9: Illustration of steps in the spectral correction technique.

first match the counts of the two flat-field cases of the synthetic and measured data for the lowest energy threshold projection and then simulate all other PMMA slab thicknesses maintaining this same measured flux. Once we have determined the transmitted counts for all slab thicknesses and threshold energies in both simulations and measurements, we find the polynomial relationship between the simulated and measured counts for each threshold energy where each point on these curves represents a different flux (PMMA thickness). The polynomial fits for each threshold energy are then applied to the CT data of the material decomposition phantoms to adjust this data to possess more ideal spectral properties with minimal distortions. The spectral correction process is illustrated via schematic in Fig. 3.9. In the equation in Fig. 3.9, I_s is the corrected counts which should agree with simulation, a_n are the D coefficients of the polynomial fit indexed by n and I_m is the raw measured counts before correction. The coefficients of the polynomial are determined from fitting the simulated versus measured counts curves for the PMMA slabs. The measured counts represent the pixel values from the object and flat-field threshold projections for the data corresponding to object of interest. The degree of the polynomial can vary and ranges from one to three for the experiments described in this work.

Simulations and measurements of PMMA slabs of six different thicknesses (0 cm, 0.913 cm, 1.841 cm, 2.436 cm, 3.349 cm and 4.277 cm) were used to determine the correlation between simulated and measured counts for various fluxes [Fig. 3.10(a)] for a sample 8-80

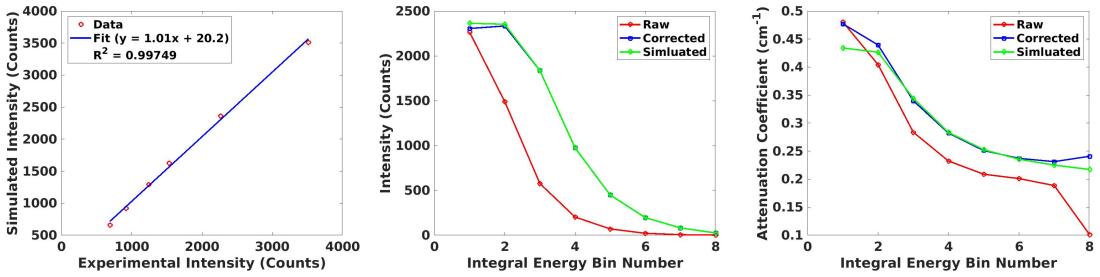

(a) (b) (c)

Figure 3.10: (a) Sample spectral correction relationship. (b) Comparison of raw, corrected and simulated counts for a sample flux. (c) Comparison of raw, corrected and simulated attenuation for a sample flux.

keV bin. Polynomial relationships were found for all eight threshold energy bins (8-80, 16-80, 24-80, 32-80, 40-80, 48-80, 56-80, 64-80) keV. To verify the correction technique was properly modifying the spectral behavior of the PMMA slab data, the counts [Fig. 3.10(b) for one PMMA thickness of 0.913 cm] and linear attenuation [Fig. 3.10(c) for one PMMA thickness of 0.913 cm] of the uncorrected, simulated and corrected cases were compared for each thickness of PMMA. The corrected counts and linear attenuation agree better with simulation than the raw data indicating that the correction is successful. This spectral correction method is further explained in [33].

3.8 Chapter Summary

As a summary of this chapter, we first described the current detector technologies available in clinics as energy integrating detectors. We then presented some background on photon counting detectors with a focus on the Medipix3RX. The process of photon interaction within the sensor, the charge creation and drift the to electrodes and the circuitry used to process the current pulse was discussed. Two modes of operation of the Medipix3RX were presented of single pixel mode and charge summing mode. The ability to acquire multiple energy-resolved measurements simultaneously in color mode was also discussed. The spatial and energy resolutions of the Medipix3RX were presented to compare the performance of different sensor specifications. Finally, challenges when working with PCDs in

the form of spectral distortions were presented along with an offline method for correcting these distortions.

Chapter 4

Computed Tomography with PCDs

4.1 General Description

Computed tomography (CT) is the process of acquiring x-ray radiographs at a number of angles around the sample [44]. This can be accomplished by either rotating the source and detector in unison or by rotating the object. The former is more of the clinical strategy where rotation of a patient would be cumbersome and the later is the strategy for our benchtop micro-CT. The configuration of our micro-CT is depicted in Fig. 4.1.

We have created a CT simulation tool with a photon counting detector model in addition to acquiring data with our laboratory micro-CT system. In either case by acquiring projection images from different angles around the object and employing a process called image reconstruction, one can obtain a three-dimensional (3D) image of the object representing the material properties of the object for the medium used to generate the image (ie: x-ray attenuation). The Radon transform describes the forward projection process for a two-dimensional (2D) parallel beam x-ray imaging system and is shown in equation form in

$$p_\theta(r) = \int_{-\infty}^{\infty}\int_{-\infty}^{\infty} f(x,y)\delta(x\cos\theta + y\sin\theta - r)dxdy. \tag{4.1}$$

In this equation, $p_\theta(r)$ represents the 1D projection of the object at projection angle θ and detector coordinate r, $f(x,y)$ is the spatially resolved 2D object with x- and y-coordinates and the delta function serves to sample the object along rays from the source to the detector. There is a double integral over space because of the two-dimensional nature of the object.

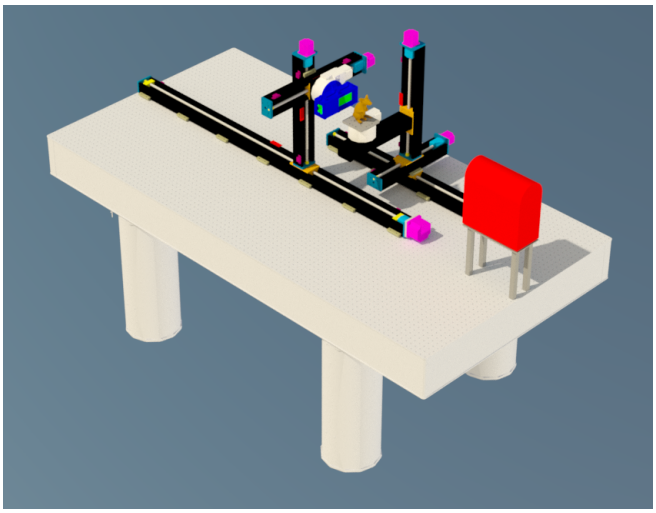

Figure 4.1: Three-dimensional model of the x-ray workbench with x-ray tube, sample stage and detector depicted.

An image of the object can be recovered using the inverse Radon transform (again assuming parallel rays and a 2D object) as seen in

$$f(x,y) = \frac{1}{2\pi}\int_0^{\pi} g_\theta(x\cos\theta + y\sin\theta)d\theta, \tag{4.2}$$

where g_θ represents the derivative of the Hilbert transform. Only 180° is required to reconstruct the object and the other half of the CT scan arc produces redundant information (again assuming parallel rays), hence the integral ranges from 0 to π. A general matrix form of the 3D computed tomography problem can also be seen in

$$\mathbf{p} = \mathbf{M}\mathbf{f} + \mathbf{n}, \tag{4.3}$$

where $\mathbf{p}$ are the 2D projections for each angle, $\mathbf{f}$ is the 3D image with x-, y- and z-dimensions, $\mathbf{M}$ is a forward projector matrix that relates the projections to the images and $\mathbf{n}$ is a noise term that accounts for non-idealities in the measurement. The process of reconstruction is another inverse problem as the goal is to find $\mathbf{M^{-1}}$ and apply it to $\mathbf{p}$ such that we can recover $\mathbf{f}$. Analytical techniques such as filtered backprojection (FBP) and the Feldkamp algorithm for cone beam CT [28] can be used, but these analytical approaches do not account for the

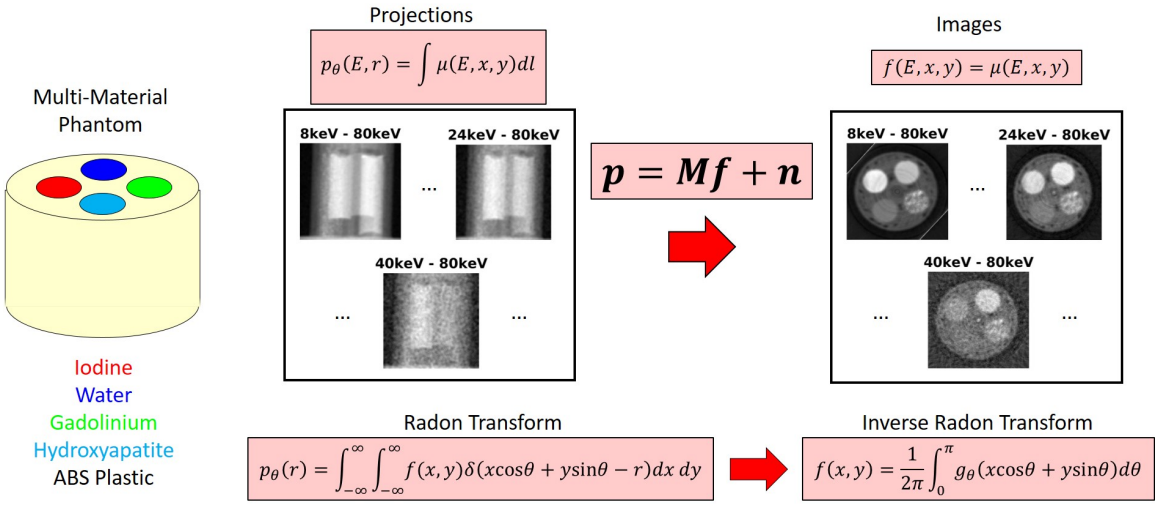

Figure 4.2: An illustration of the reconstruction process using a cylindrical multi-material phantom as an example.

noise term. Alternatively, statistical techniques exist which can model the noise in the data and provide high accuracy reconstructions even under low dose conditions. However, the price to be paid is that statistical approaches require more time and computing resources which has limited their applicability to the clinical setting. Therefore, we will mostly employ the Feldkamp algorithm in the dissertation which is simply an adaptation of filtered backprojection for cone beam CT.

For conventional energy integrating detectors, one would obtain one set of projections and through image reconstruction, one corresponding 3D image. Because of the energy-resolving capability of PCDs, one can obtain multiple sets of projections corresponding to each energy measurement and after reconstruction, the same number of 3D images. These multi-energy projections and reconstructions can be used for material decomposition. Here, we consider image domain decomposition techniques conducted after image reconstruction. An example of the cylindrical multi-material phantom (shown on the right) is displayed where the x-ray projections are taken from the side of the phantom as it rotates (Fig. 4.2). An example of a reconstructed slice is shown on the right as viewed from the top of the phantom.

4.2 CT Simulation Platform and PCD Model

The simulation platform derives from a serial cascade model [82] where the source, object and detector were all treated analytically [93, 19]. The source was modeled using the tungsten anode spectral model using interpolating polynomials (TASMIP) method. An aluminum filter was applied to the source spectrum to reduce lower energy photons which only minimally contribute to image formation and significantly increase patient dose. A total CT dose of 7.92 mGy was applied to 360 projections over a full arc of 360°. The object was modeled as cylinders of various tissue-like or contrast agent materials. Cylinders can be modeled as elongated ellipsoids whose projections are mathematically described as follows:

$$P_{\theta,\gamma}(t,r) = \frac{2\rho ABC}{a^2(\theta,\gamma)}\Bigg[a^2(\theta,\gamma) - t^2(C^2\cos^2\gamma + (B^2\cos^2\theta + A^2\sin^2\theta)\sin^2\gamma) - r^2(A^2\cos^2\theta + B^2\sin^2\theta)\left(\frac{7+\cos(4\gamma)}{8}\right) - 2tr(\sin\gamma)(\cos\theta)(\sin\theta)(B^2 - A^2)\Bigg]^{1/2}, \quad (4.4)$$

where $a^2(\theta,\gamma)$ is defined as

$$a^2(\theta,\gamma) = C^2(B^2\sin^2\theta + A^2\cos^2\theta)\cos^2\gamma + A^2B^2\sin^2\gamma. \quad (4.5)$$

In Eqn. 4.4, $P_{\theta,\gamma}(t,r)$ is the projection of the ellipsoid for projection angle θ and detector tilt angle γ. t and r are detector coordinates and A, B and C are the axis lengths of the ellipsoid in the x-, y- and z- directions. For x-ray imaging, ρ represents the attenuation of the ellipsoid material. The detector was modeled with a cadmium telluride (CdTe) sensor with square pixels of dimension 55 μm or 110 μm, a thickness of one millimeter and capable of simultaneously recording photon counts for up to eight energy bins similar to the Medipix3RX. Here we use the maximum number of energy bins simultaneously provided by the Medipix detector to maximize the information recorded. Otherwise, the detector was modeled to have an ideal response with the corresponding CdTe efficiency. The absorption

efficiency or detector gain was modeled as:

$$G(E) = 1 - e^{d\tau(E)}, \tag{4.6}$$

where G is the efficiency which is a function of energy, E, d is the sensor thickness and τ is the probability of photoelectric absorption for the sensor material.

Before performing image reconstruction and material decomposition, energy-resolved, raw flat-field and object projection data must be simulated or measured with eight energy bins. This was done by simulating the x-ray projections at every keV until the tube peak voltage. In some cases equal count bins were then defined by dividing the simulated x-ray energy spectrum into eight bins and the data at each keV was then summed to form the data corresponding to each bin. Data in this form is called energy binned data and can be obtained from a PCD by subtracting adjacent energy bins. In other cases, data was simulated to be more similar to the raw data as collected by the PCD where each energy measurement is comprised of all photons from the threshold energy to the kVp. Data in this form is referred to as counts-over-threshold data and can offer improved noise characteristics over the energy binned data (Poisson vs. Skellam [85] noise). These two differing forms of the data are displayed in Fig. 4.3 overlaid on the simulated TASMIP source spectrum where (a) represent binned mode and (b) represent counts-over-threshold mode. Notice the bins overlap in counts-over-threshold mode but do not in binned mode.

Poisson noise was then added to the binned flat-field and object data so that the data would have suitable statistics. Poisson noise is described by the following distribution:

$$\Pr(X = k) = \frac{\lambda^k e^{-\lambda}}{k!}, \tag{4.7}$$

where $\Pr(X = k)$ is the probability that the discrete random variable X is equal to a natural number k and λ is the mean and variance of the Poisson distribution. In the case of a photon counting measurement, X is the measured photon counts which is sampled from the probability mass function in Eqn. 4.7 with mean λ and variance λ. The focal spot

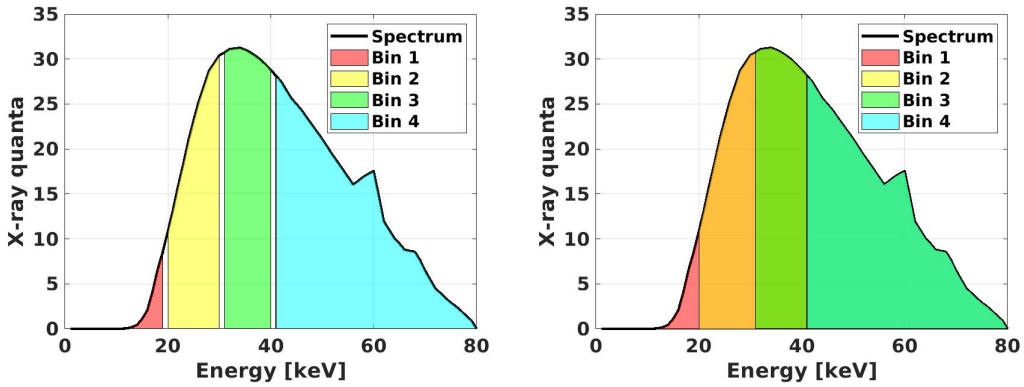

(a) (b)

Figure 4.3: Different forms of data generated from the PCD simulation model with (a) representing binned mode and (b) representing counts-over-threshold mode.

size of the source was modeled via a Gaussian blur. If unequal count bins were obtained, a simple weighting scheme based on contrast to noise ratio (CNR) could be employed to overcome the unequal noise statistics [74, 75, 45]. The degraded projection data was then filtered via a Wiener or bilateral filter [26] to reduce the impacts of this Poisson noise. The bilateral filter is described by

$$I^{\text{filtered}}(x) = \frac{1}{W_p} \sum_{x_i \in \Omega} I(x_i) f_r(||I(x_i) - I(x)||) g_s(||x_i - x||), \tag{4.8}$$

where the normalization term, W_p, is defined as

$$W_p = \sum_{x_i \in \Omega} f_r(||I(x_i) - I(x)||) g_s(||x_i - x||). \tag{4.9}$$

In Eqn. 4.8, $I^{\text{filtered}}(x)$ represents the value of the filtered image at coordinate x, I represents the input image, Ω represents the filter domain centered on x where x_i is another pixel in the domain, f_r is the range kernel for smoothing differences in intensity and g_s is the spatial kernel for smoothing differences in coordinates. Both f_r and g_s are typically Gaussian functions. The synthetic data produced by this simulation tool is now ready for image reconstruction.

4.3 Geometry, Alignment and Data Acquisition of Physical X-ray Micro-CT

A small magnification geometry (≈ 1.2) was employed throughout this dissertation (Fig. 4.1). The object was placed in the beamline approximately 60 cm from the source and the detector was placed in the beamline approximately 10-15 cm beyond the object. The source was fixed in place and the sample was placed on a rotation stage to allow for computed tomography measurements. The detector was mounted on an X-Y translation stage to permit raster scanning to image larger objects. In this small-magnification geometry, the major contributor to image formation is attenuation and can be modeled as such neglecting the effects of refraction. If a larger magnification were used such as 2 or 3, the contributions to image formation are now a combination of both attenuation and phase contrast. Therefore, when modeling data one must consider both effects. Soft-tissue contrast is higher for phase-sensitive measurements as the real part of the refractive index (which is related to phase contrast) is several orders of magnitude greater than the imaginary part of the refractive index (which is related to attenuation contrast). However, phase contrast measurements are more time-consuming and doses are higher. Data modeling also becomes more complex when refraction is added.

With our high-resolution PCDs with pixels sizes down to 55 μm, alignments of the micro-CT components becomes important. A rough system alignment to ensure that the object and detector lie close to the center of the beamline is first conducted by eye. The sample rotation stage is then leveled such that the axis of rotation is vertical. Then, using a straight edge placed on the leveled object stage, the detector is rotated in the plane normal to the beamline until the projection of the straight edge on the detector aligns with one column of pixels. This rough axis alignment is followed by a more precise axis alignment using a phantom made of three ball bearings. The ball bearing phantom is placed off-center on the rotation stage and a scout CT scan is acquired with a coarse angular sampling ($\approx 10^\circ$ step). The centers of trajectories of each of the ball bearings are pin-pointed by examining all projections and the detector is again rotated until all of these centers lie in the same pixel column. If the ball bearings prescribe an elliptical path rather than a line, the detector

and sample are translated up or down (y-direction) until the projection of the trajectory of the ball bearings each prescribe a horizontal line. Finally, the detector is translated in the x-direction to center the projection of the rotation axis (as defined by the centers of the trajectories of the ball bearings) to the center of detector.

Once the system is aligned, a CT scan can commence. This requires communication between the sample rotary table and Medipix3RX detector. We employ a step and shoot strategy for image acquisition where object rotation and image acquisition are done sequentially. The CT scan of the object is usually conducted over at least a 250° arc with a 1° step size, but the rule of thumb is the arc of the CT scan should be at least 180° plus cone angle [44]. Because of temporal and temperature related fluctuations in detector performance, it is also recommended to acquire multiple flat-fields in the same process as the object CT scan. Usually 30-50 flat-fields is sufficient. This offers more flexibility when it comes to processing the CT data, but I find that averaging these flat-fields and flat-field correcting each object projection with the average flat-field works pretty well.

4.4 Three-Dimensional Filtered Backprojection

In the beginning of this chapter, we described some basics of image formation and reconstruction for a 2D object imaged with parallel x-rays. However, our laboratory x-ray source emits conical x-rays rather than parallel x-rays. Therefore, the proper reconstruction algorithm which accurately models this cone-beam geometry must be applied to achieve accurate reconstructions. In this section, we described an adaptation of filtered backprojection (FBP) for cone-beam imaging systems. The description of 3D FBP presented in the section pertains to [28] and [44]. The reconstruction is described with regards to filtering and backprojecting a single plane within the cone beam of the source. Each elevation within the cone (described by z or ζ) is considered separately and the final 3D reconstruction is the sum of the contributions of all tilted fan beams to the object. The coordinate system describing the 3D FBP reconstruction can be seen in Fig. 4.4.

We start from the filtered backprojection algorithm for equispatial rays. In our case, each

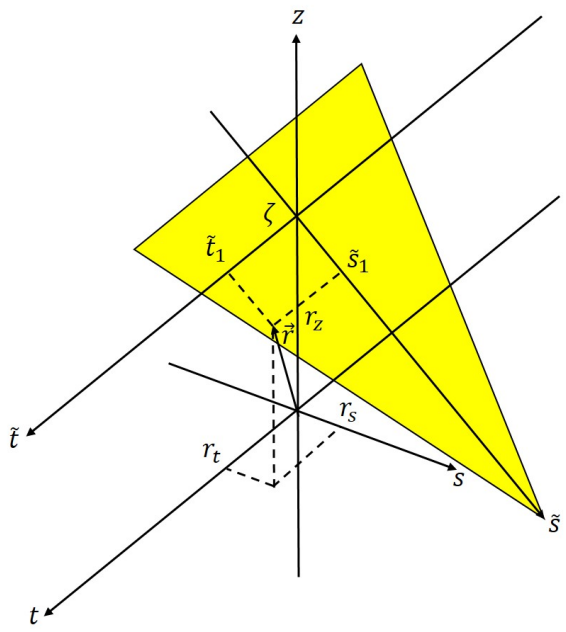

Figure 4.4: The $(\tilde{t}, \tilde{s})$ coordinate system describing a point in the object with respect to a tilted fan beam.

fan is angled out of the source-detector plane of rotation. Starting from the two-dimensional fan beam FBP reconstruction formula for point (r,ϕ) [44], the filtered backprojection algorithm can be described by

$$g(r,\phi) = \frac{1}{2}\int_0^{2\pi} \frac{1}{U^2}\int_{-\infty}^{\infty} R_\beta(p)h(p'-p)\frac{D_{SO}}{\sqrt{D_{SO}^2+p^2}}dpd\beta, \tag{4.10}$$

where $g(r,\phi)$ is the reconstructed image in polar coordinates described by radius r and angle ϕ. U is the ratio of the distance of the projection of the source-to-pixel line on the central ray to the source-to-origin distance where the origin is defined as the center of rotation of the CT scanner. β describes the projection angle about the origin and D_{SO} is the source-to-origin distance. $R_\beta(p)$ is the fan beam projection on the detector and $h(p'-p)$ describes the ramp filter used to overcome the unequal radial sampling of the projections in Fourier space. p' and p describe the position on the detector for the fan beam projection and equivalent parallel projection, respectively. p', $h(p)$ and U are further defined as:

$$p' = \frac{D_{SO}r\cos(\beta-\phi)}{D_{SO}+r\sin(\beta-\phi)}, \tag{4.11}$$

$$h(p) = \int_{-W}^{W} |\omega| e^{j\omega p} d\omega, \tag{4.12}$$

and

$$U(r, \phi, \beta) = \frac{D_{SO} + r\sin(\beta - \phi)}{D_{SO}}. \tag{4.13}$$

$h(p)$ is the filtering kernel which is the inverse Fourier transform of $|\omega|$ in the frequency domain where ω is the radial spatial frequency variable in polar coordinates. We now replace the (r, ϕ) coordinate system by the rotated coordinates, (t, s), where t and s represent positions of the reconstruction based on the source-detector rotation angle, β. The expressions are

$$t = x\cos\beta + y\sin\beta, \tag{4.14}$$

$$s = -x\sin\beta + y\cos\beta, \tag{4.15}$$

$$x = r\cos\phi, \tag{4.16}$$

and

$$y = r\sin\phi, \tag{4.17}$$

where x and y are the object rectangular spatial coordinates. These equations lead to new expressions for p' and U as described by

$$p' = \frac{D_{SO} t}{D_{SO} - s}, \tag{4.18}$$

and

$$U(x, y, \beta) = \frac{D_{SO} - s}{D_{SO}}. \tag{4.19}$$

The fan beam reconstruction is then rewritten as

$$g(t, s) = \frac{1}{2} \int_0^{2\pi} \frac{D_{SO}^2}{(D_{SO} - s)^2} \int_{-\infty}^{\infty} R_\beta(p) h\left(\frac{D_{SO} t}{D_{SO} - s} - p\right) \frac{D_{SO}}{\sqrt{D_{SO}^2 + p^2}} dp d\beta. \tag{4.20}$$

We now adapt this fan beam reconstruction to cone beam by first accounting for the tilt

angle of the fan out of the plane of rotation of the source and detector. This changes the size of the fan and coordinate system of the reconstruction point. The new coordinate system is $(\tilde{t}, \tilde{s})$ which represents the location of the reconstructed point with respect to the tilted fan (Fig. 4.4). The changing fan size results in a change in the source to origin distance and source-detector rotation angle differential as described by

$$D_{SO}^{\prime 2} = D_{SO}^2 + \zeta^2, \tag{4.21}$$

where ζ is the height of the fan beam above the center of the plane of rotation. The increment of angular rotation $d\beta'$ also changes to

$$d\beta' = \frac{d\beta D_{SO}}{\sqrt{D_{SO}^2 + \zeta^2}}. \tag{4.22}$$

Then substituting D'_{SO} for D_{SO} and $d\beta'$ for $d\beta$ and writing the projection data as $R_{\beta'}(p, \zeta)$, the cone beam reconstruction equation becomes

$$b(\tilde{t}, \tilde{s}) = \frac{1}{2} \int_0^{2\pi} \frac{D_{SO}^{\prime 2}}{(D'_{SO} - \tilde{s})^2} \int_{-\infty}^{\infty} R_{\beta'}(p, \zeta) h\left(\frac{D'_{SO}\tilde{t}}{D'_{SO} - \tilde{s}} - p\right) \frac{D'_{SO}}{\sqrt{D_{SO}^{\prime 2} + p^2}} dp d\beta'. \tag{4.23}$$

This equation can then be converted back into the original (t, s, z) coordinate system as shown in

$$b(t, s) = \frac{1}{2} \int_0^{2\pi} \frac{D_{SO}^2}{(D_{SO} - s)^2} \int_{-\infty}^{\infty} R_{\beta}(p, \zeta) h\left(\frac{D_{SO}t}{D_{SO} - s} - p\right) \frac{D_{SO}}{\sqrt{D_{SO}^2 + \zeta^2 + p^2}} dp d\beta. \tag{4.24}$$

Therefore, we can now describe the steps of cone beam reconstruction as 3D filtered backprojection. In step 1, the projection data $R_\beta(p, \zeta)$ are multiplied by the function $(D_{SO}/\sqrt{D_{SO}^2 + \zeta^2 + p^2})$ to obtain the weighted projections which accounts for the tilted fan geometry. In step 2, the weighted projections are convolved with $h(p)/2$ (the ramp filter) by multiplying their Fourier transforms with respect to p. Convolution is conducted for each elevation, ζ, separately. In the third and final step, each projection is backprojected over the 3D reconstruction grid.

4.5 Beam Hardening and Scatter

Beam hardening results from the preferential absorption of low energy x-rays by the object, which leads to a shift in the energy spectrum to higher energies as the photons traverse the object. After reconstruction, beam hardening is observed as cupping artifacts where the object attenuation is depressed near the center relative to the edges of the object. Beam hardening can also be observed as streaking artifacts near high-attenuating materials such as bone or metal implants. Analytical reconstruction techniques such as filtered backprojection are derived for monoenergetic x-rays. The polychromatic nature of most clinical and laboratory x-ray tubes thus leads to discrepancies between the assumptions of the reconstruction and reality. Common techniques exist to estimate the effective energy of the polychromatic x-ray source [61, 62], but again this energy often changes with the introduction of an object and is object-specific. This also leads to challenges when one wants to model the reconstructed attenuation with some fitting functions. If the exact effective energy of the reconstruction is unknown, then calculating energy-dependent model coefficients becomes ambiguous. Also, if cupping or streaking exist then the affected regions will not represent the required accurate attenuation values. Beam hardening artifacts are difficult to remove, but through the methods outlined in [2] one can generate equivalent monoenergetic attenuation tomograms at any energy free from beam hardening artifacts.

Scattering is the most common photon interaction at higher energies in the medically relevant range. Scattering is a statistical process where the deflected photon is sent in a random direction. Because of this, scattered photons can reach the detector leading to additional counts not modeled in the image reconstruction algorithm. These additional counts will lead to decreased attenuation values and the result is often similar to beam hardening as cupping or streaking artifacts are seen after reconstruction. These artifacts result from the change in scatter fraction from angle to angle throughout the CT scan. The scattered intensity remains rather constant regardless of CT angle, but the primary intensity changes with projection angle. This makes the influence of scatter greater for some projections than others. Similar challenges to beam hardening exist when attempting to model data

with scatter as the reconstructed attenuation values will deviate from expectation. However, scatter is an easier problem to correct for as various hardware-based methods exist for scatter rejection [59] and software-based methods exist for reducing its effect [36].

4.6 Chapter Summary

In this chapter, some of the basics of computed tomography were described for a simple 2D object with parallel x-rays through the Radon and inverse Radon transforms. The more general description of the computed tomography problem was then presented in matrix form. Our computed tomography simulation tool was described with some specifics on source, object and detector modeling. Our laboratory benchtop micro-CT scanner was then discussed. Here we went over the system alignment procedure and some data acquisition strategies that provide good imaging performance as a guide to future users of our workbench or others. The more practical algorithm for image reconstruction of data collected from a cone beam system of 3D filtered backprojection was then discussed. Finally, challenges in computed tomography of beam hardening and scatter that result in artifacts in image reconstruction were presented.

Chapter 5

Material Decomposition

5.1 General Description

Material decomposition is the process of solving for material specific images of a multi-material object using spectral x-ray measurements. This separation process hinges on the fact that the attenuation of each voxel can be written as a linear combination of all the materials that comprise said voxel. In a more general sense, material decomposition is an inverse problem where the multi-energy attenuation data is fit with a model comprised of material properties (x-ray attenuation) of each of the constituent materials of the problem. The unknowns or parameters (material volume fractions) are the spatial material distributions and concentrations of each of the materials. Obtaining the parameters that best model the data is done by various matrix inversion techniques. If the number of unknowns and equations are the same, then numerical inversion techniques for square matrices like lower-upper (LU) decomposition and back-substitution can be used. However, this is not generally the case for material decomposition problems which are often overdetermined. For overdetermined problems, least squares techniques are commonly used. In this dissertation, a bounded variable least squares technique is used because we solve for volume fraction images which are conveniently bounded by zero and one [18]. A general depiction of an image domain material decomposition process is demonstrated via schematic in Fig. 5.1 using the multi-material phantom described in Sec. 7.1 as an example.

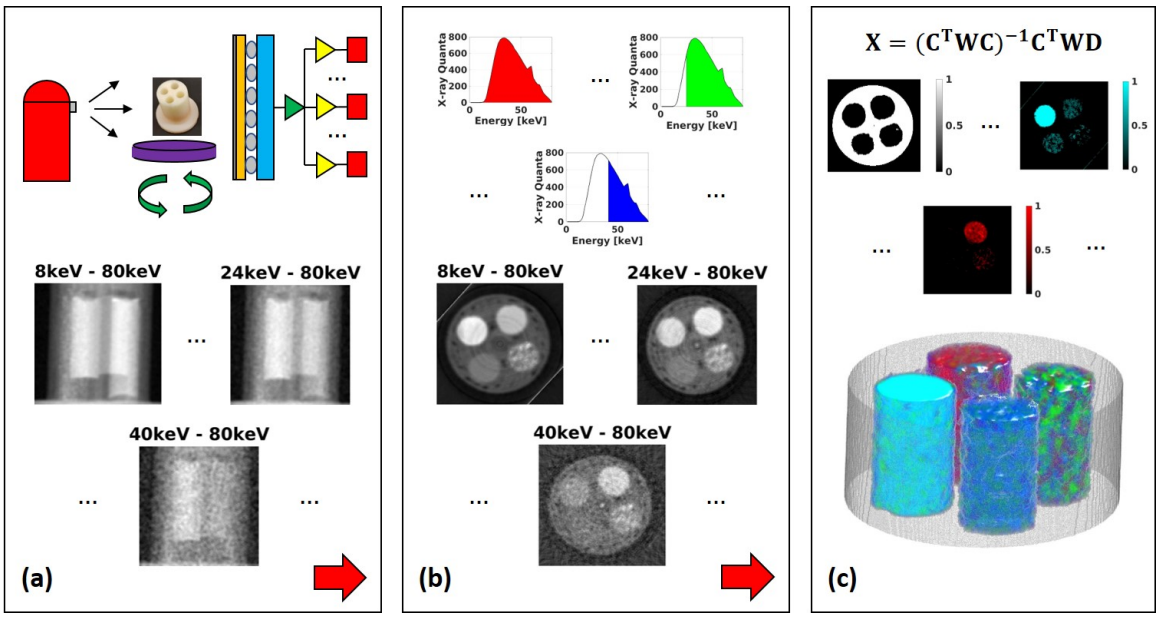

Figure 5.1: (a) Multi-energy CT data is collected with a PCD. (b) The multi-energy projections are reconstructed into multi-energy CT images. (c) Material decomposition is conducted to resolve 3D material distributions.

5.2 Physics-Based Approach

Alvarez and Macovski [2] generated empirical models of photoelectric absorption and Compton scattering through measurement of many tissue-like materials. The determined model for the total linear attenuation, $\mu(E)$, can be described by

$$\mu(E) = a_1 \frac{1}{E^3} + a_2 f_{\mathrm{KN}}(E), \tag{5.1}$$

where a_1 and a_2 are physical constants dependent on the properties of the imaged material and $1/E^3$ and $f_{\mathrm{KN}}(E)$ are the physics models for the photoelectric and Compton effects, respectively. The energy-dependent basis for Compton scattering, $f_{\mathrm{KN}}(E)$ as seen in

$$f_{\mathrm{KN}}(\alpha) = \frac{1+\alpha}{\alpha^2}\left[\frac{2(1+\alpha)}{1+2\alpha} - \frac{1}{\alpha}\ln(1+2\alpha)\right] + \frac{1}{2\alpha}\ln(1+2\alpha) - \frac{(1+3\alpha)}{(1+2\alpha)^2}, \tag{5.2}$$

represents the Klein-Nishina function [47]. In Eqn. 5.2, α equals the ratio of the photon energy to the rest mass of an electron of 511 keV. The physical constants from Eqn. 5.1

are defined as

$$a_1 \approx K_1 \frac{\rho}{A} Z^n, \tag{5.3}$$

and

$$a_2 \approx K_2 \frac{\rho}{A} Z, \tag{5.4}$$

where K_1 and K_2 are constants, ρ is mass density, A is atomic weight and Z is atomic number. In Eqn. 5.3, the exponent n is approximately equal to 4. From these equations, a linear system of equations can be written with each equation representing a different energy. This system forms a matrix equation of the form of $\mathbf{Ax} = \mathbf{b}$ where $\mathbf{A}$ is the matrix of energy-dependent coefficients [$1/E^3$ and $f_{KN}(E)$], $\mathbf{x}$ are the spatially-dependent unknowns (a_1 and a_2) and $\mathbf{b}$ is the attenuation data [$\mu(E)$]. Solving this system of equations through matrix inversion techniques yields spatial maps representing the fractions of photoelectric absorption, a_1, and Compton scattering, a_2. Because there are only two main physical interactions being considered, this method is limited the separation of only two materials. Notice that the energy-dependent function for the photoelectric term does not model K-edges as it was generated from measurements of tissue-like materials. If a material with a K-edge is present in the object, a third term can be added representing the K-edge material, such as seen in

$$\mu(E) = a_1 \frac{1}{E^3} + a_2 f_{\text{KN}}(E) + a_3 f_{\text{K-edge}}(E), \tag{5.5}$$

where $f_{\text{K-edge}}(E)$ is a function that captures the discontinuity of the contrast agent and a_3 represents its spatial distribution [1]. As an alternative to this physics models based approach to material decomposition, materials can be separated using their mass or linear attenuation coefficients as basis functions [52]. This second approach will be the primary focus of rest of this dissertation.

5.3 Materials-Based Approach

In the materials-based approach to material decomposition similar to [51, 49, 50, 1, 48, 54, 68], the spatial distributions of basis materials are found using the energy-dependent attenuation coefficients as basis functions. This process can be conducted from spectral measurements obtained from dual energy or photon counting approaches as in the physics-based method. For N available energy bins indexed by j, one can reconstruct N spectrally varying CT images of the object and one additional CT image representing the conservation of volume constraint. If we represent these multi-energy 3D attenuation maps as $\vec{\mu}(E_j, \vec{r})$ and assume that the material is composed of M basis materials, one can write the decomposition model as:

$$\vec{\mu}(E_j, \vec{r}) = \sum_{i=1}^{M} \mu_i(E_j) \vec{f}_i(\vec{r}), \tag{5.6}$$

where $\vec{f}_i(\vec{r})$ denotes the respective volume fractions for each basis material i and $\vec{r}$ is the spatial variable. In Eqn. 5.6 for an energy binned mode dataset, E_j represents the energy corresponding to the median counts within bin j based on the x-ray energy spectrum. For an counts-over-threshold mode dataset, E_j represents the threshold energy used in the CT acquisition as described in Sec. 5.9. In either case E_j is the look-up energy used to calculate the corresponding energy-dependent attenuation of each material which form the elements of the material decomposition system matrix. In our experiments, these threshold energies are chosen to be equally spaced with respect to energy such that more thresholds are acquired than materials within the sample providing an over-determined system. When K-edges are present in the sample, projection data is acquired at energies higher and lower than all K-edges. This materials-based approach can also be formulated using the energy-dependent material mass attenuation coefficients as basis functions with the spatial unknowns representing the material densities. In a single-step, materials-based decomposition technique, one attempts to solve for the volume fraction maps of all the basis materials at once using a technique like the least squares method. In the event of unequal counts in each bin, energy bin weighting schemes based on the CNR of the background region can be

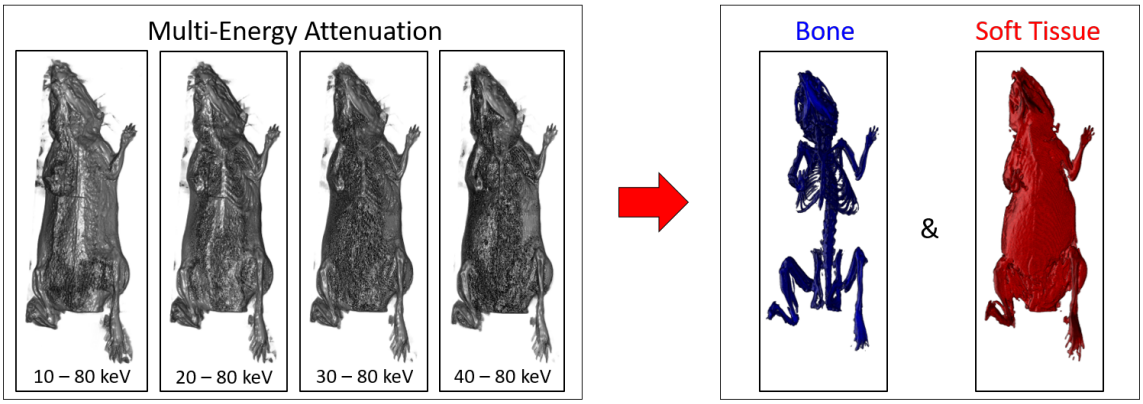

Figure 5.2: General depiction of the mouse material decomposition problem where the multi-energy CT reconstructions are separated into 3D images of bone and soft tissue.

used to improve decomposition accuracies and reduce noise. An example of a two-material decomposition where spectral x-ray images of a mouse have been separated into images of bone and soft tissue is shown in Fig. 5.2 to further illustrate the single-step decomposition approach.

5.4 Background

To provide some historical perspective, the use of spectral x-ray measurements from a dual energy imaging system to virtually distinguish materials in an object was first proposed by Alvarez and Macovski [2] in their seminal work in 1976. In this work, two empirical models were discussed to capture the physical phenomena that govern x-ray interactions in the range of medical imaging of photoelectric absorption and Compton scattering. In the following year, Brooks [8] adapted the decomposition equations for tomographic image domain. In an even later work by Lehmann [52], another method by which a multi-material object can be separated into material specific images using their energy-dependent linear attenuations as basis functions was proposed. This work also showed that the two methods (the physics-based decomposition approach and the materials-based decomposition approach) are equivalent. Since these initial works, many papers have been published for projection domain [51, 2, 76, 99] and image domain [51, 65, 55, 54] decompositions. In the projection

domain approach, one attempts to resolve the object into basis material thickness maps knowing these constituent material concentrations or densities [51, 2, 76, 99]. These approaches have been executed using both dual energy strategies [2, 99] and PCDs [51, 76]. In image domain methods, the 3D spectral attenuation maps of the composite materials are first obtained. This information is then used for decomposition [51, 65, 55, 54]. A third approach, such as the ones explained in [10, 56, 5, 16], can be used to directly estimate basis material images from binned raw projection data. However, because of the two physical processes that govern x-ray imaging in the diagnostic energy range, the number of materials that can be accurately separated is limited to two. If a contrast agent is introduced, the number of basis function can be extended to three by the addition of a third term which captures the K-edge discontinuity [1]. Therefore, there's interest in developing methods that can solve for more than two or three materials in decomposition problems [64, 56, 98, 24].

5.5 Traditional Dual Energy Approaches

There are two major ways to acquire spectral x-ray measurements: the more traditional dual energy approaches and those that utilize photon counting detectors. The former utilizes energy integrating detectors and represents a more mature technology. More dual energy systems exist in clinics (or conventional systems can be easily retrofitted), so there exist much interest in developing techniques for material decomposition suited for dual energy systems. One such example by Zamyatin, Natarajan and Zou [100] proposes a multi-material decomposition method that plots the relationship between the attenuation of the low and high energy images and then uses the different clustering patterns to separate materials in dual-energy CT. Another article by Mendonca et al. [64] propose a technique for dual energy multi-material decomposition where mass conservation and volume conservation are used to form the ideal solution assumption. This assumption is used to define a library of triplets which captures the attenuation values of all likely three material combinations based on the constituent materials in the problem. Any material that exists in or near the pre-selected library is uniquely identified.

Long and Fessler [56] build on the technique by Mendonca and add statistical image reconstruction to the decomposition where an objective function formed as the sum of the likelihood and penalty terms is indirectly minimized through the use of surrogate functions. The technique repeatedly solves the forward problem of image generation and inverse problem of image reconstruction and decomposition. Xue et al. [98] also build on the multi-material decomposition technique proposed by Mendonca and apply it to an image domain statistical decomposition. However, Xue's method is implemented completely in the image domain and the forward process of image generation is only simulated (measured) once. Ding's method is also implemented in image domain and makes use of the complementary information between different material images such as material boundaries and edges and enforces the sparsity of materials contained in each voxel. Statistical approaches such as Long, Xue and Ding require the specification of tunable parameters such as regularization and edge-preserving coefficients which are difficult to determine without trial and error. In addition, these approaches are more computationally complex and require iteration increasing solution times. Most current dual energy material characterization techniques can accurately separate two [2, 65, 57, 101] or three [55, 99, 37] materials. So the need for a simple, robust algorithm for multi-material decomposition adapted for photon counting detectors is desired.

5.6 Photon Counting Approaches

The alternative approach involves photon counting detector technologies which are still in their infancy, because the ability to grow high purity, high atomic number sensors with large fields of view still remains a challenge. However, semiconductor fabrication processes continue to improve and prototype chip arrays where many small sensors are combined to form one larger detector have been accomplished [4, 42]. Predicting these technological advances, many have begun developing material decomposition techniques adapted for photon counting imaging systems. One such example by Le and Molloi [49, 50] proposes the idea of separating the decomposition into two steps of a segmentation step and a quantification

step. The former limits the number of materials contained in each voxel to the single most likely material and the latter quantifies the concentration of the identified material of each voxel. This process showed the ability to distinguish up to four materials of calcium, iodine, adipose and glandular tissues in mastectomy specimens. A follow-up paper by Alessio and MacDonald [1] extended the method to include material classes such that one voxel need not be limited to 100% of a single material. This paper also explored two decomposition methods of the physics basis function and material basis function techniques both with only single material voxels and with material classes allowing for multi-material voxels. The materials of interest were similar as calcium and iodine were suspended in water and oil solutions and embedded in plastic phantoms. The results were also similar as successful decomposition of four materials was displayed.

Another group (MARS Bioimaging Ltd., Christchurch, New Zealand) displayed the ability to quantify concentrations of calcium, iron and iodine using a constrained least squares decomposition technique based on information entropy and degrees of freedom [71]. A succeeding paper by the same group [6] proposed another two-step approach which uses a classification step to categorize each voxel as air, soft-tissue-like or high-atomic number and then solves different least squares problems based on each category to quantify material concentrations with each voxel. This paper shows the decomposition of a six-material phantom and two multi-concentration phantoms, although decomposition errors can be high. Most current photon counting material characterization techniques can accurately separate three [54, 51, 48, 71, 46] or four [49, 50, 1, 46] materials. Therefore, again there is a need for a decomposition algorithm that can accurately separate multiple materials with high accuracies from data collected with a photon counting detector.

5.7 Applications of Material Decomposition

Some of the other current applications are breast imaging [49, 50, 51, 15], brain and skull imaging [2, 65, 100, 98, 25], characterization of arterial plaques [1, 71], quantification of liver iron overload [55, 54], heart and chest imaging [76, 27, 57], kidney stone composition analysis

[76], abdomen imaging [17, 64] and joint and pelvis imaging [98, 101]. These decomposition techniques can be applied in the clinical setting or to small animal imaging [57, 71, 37, 58, 96]. Outside of medical imaging, their exist many applications of material decomposition as well. These uses include airport security [84, 40], shipping port security [81, 80], detecting land mines [40, 84], monitoring spent nuclear fuel [7, 63], analysis of geological sample compositions [67, 35], chemical analysis of fuel cells [69] and non-destructive testing [39].

5.8 Limitations of Current Material Decomposition Techniques

As described in Chap. 2, the attenuation characteristics of many materials of interest in medical imaging can be rather similar. This makes distinguishing between these materials rather challenging and causes the inverse problem of material decomposition to be ill-conditioned. The ill-conditioning spans from the challenges related to representing models for similar materials in a matrix which leads to dependencies between the columns of the matrix. These columns become nearly copies of one another leading to numerical instabilities where errors in the observations cause large errors in the parameters. There are also only two major contributors to x-ray attenuation in medical imaging. This means that the energy-dependent behavior of all materials only depends on two phenomena and therefore, only two unique models can be used to represent most materials. With the addition of contrast agents or by utilizing the refraction of x-rays, perhaps one additional model can be added to the system. In addition, it could be possible to model Rayleigh scattering in the decomposition. However, the more models added to the system and the larger the system matrix becomes, the more complex the inversion becomes and the higher the chance of further ill-conditioning. Thus, most current material decomposition techniques are limited to two or three materials.

5.9 Energy Function Calculation for Threshold Projections

In some simulations and all experiments (described in Chap. 7), we must generate suitable basis functions representing the counts-over-threshold data. Operating on the raw

counts-over-threshold data without differentiation does result in a change in the decomposition equations. The energy-dependent terms in the decomposition for binned data are simply the linear attenuation coefficients of each material. However for counts-over-threshold data, these terms are instead related to the energy-dependent trends in the threshold energy bins. To estimate these energy-dependent functions, the same simulation tool as described in Sec. 4.2 was used. The source was modeled using the TASMIP method with the corresponding tube peak voltage of the simulation or measurement. Each of the materials of our decomposition phantoms was separately modeled as a one-dimensional (1D), single-material slab. The detector was modeled to represent the sensor type (Si or CdTe) and thickness of the detector used in the experiments. Projections of the slabs were then simulated at every keV from the lowest threshold energy to kVp. Flat-field and object data at each keV was then summed into bins from the lower bound to the kVp, resembling data collected from the Medipix detector.

In order to compute the energy-dependent functions required for material decomposition, the simulation data described in the previous paragraph is first converted into projected attenuation data through flat-field correction and the negative logarithm operation as seen in

$$\mu_I(E_j) = -\log\left[\frac{\int_{E_j}^{\mathrm{kVp}} \Phi(E) e^{-\mu(E)t} D(E) dE}{\int_{E_j}^{\mathrm{kVp}} \Phi(E) D(E) dE}\right] / t. \tag{5.7}$$

In Eqn. 5.7, $\mu_I(E_j)$ is the simulated, projected attenuation for counts-over-threshold data for energy E_j and t and $\mu(E)$ are the projected thickness and linear attenuation coefficient of the single-material slab, respectively. As in Sec. 3.3, $\Phi(E)$ is the spectrally dependent incident x-ray flux and $D(E)$ is the detector response function. The average projected thickness of the phantom can be used as the assumed thickness of the single-material slab, t, in Eqn. 5.7. By including a model of the attenuation through the single material slabs in Eqn. 5.7 and integrating over energy, we can model beam hardening effects in our basis functions. This can lead to better agreement between the attenuation data and basis functions and thus, better decomposition performance.

5.10 Chapter Summary

In this chapter, the fundamentals of material decomposition were presented with examples of two techniques based either on models of the x-ray interactions or based on the properties of the materials in the imaged object. Next, some of the origins of virtual material separation were discussed where the techniques were separated into two groups of dual energy strategies and photon counting strategies based on the type of detector available. The difference between the two forms of data from a PCD (binned versus counts over threshold) was stressed. This chapter was concluded by a section on a method for computing the energy-dependent models for counts-over-threshold data.

Chapter 6

Novel Multi-Step Decomposition

6.1 The Multi-Step Method

In a multi-step decomposition method, we propose that the material decomposition can now be computed in a series of steps, each separating one new material from the same multi-bin data. We describe the method with an example of a four-material decomposition (6.1). Successful results from six-material and mixed-material decompositions are shown in Sec. 6.5.3 and Sec. 6.5.4. Descriptions of these problems can be seen in Fig. 6.2 and 6.3. In Fig. 6.3, the multi-color circles indicate a 50%/50% mixture by volume of the two materials that fills the entire well. They are not meant to indicate the spatial distribution of the two materials within the well. In most simulations presented in this chapter unless otherwise specified, the synthetic PCD data was generated with 110 μm pixels in a 256 $\times$ 256 grid. Images of the phantom were then reconstructed to 119 μm isotropic voxels yielding multi-energy 3D attenuation images with 200 $\times$ 200 $\times$ 200 voxels.

In our four-material model problem, the chosen materials are water, calcium, iodine and gold. Water represents the background breast tissue, calcium represents breast microcalcifications and gold and iodine are contrast agents. The model geometry is composed of a water background with columns of calcium, iodine and gold. Figure 6.1(a) shows a cross section of this phantom. In initial separation steps, the focus is examining how distinct the material is from the other materials based on the linear attenuation versus energy curves

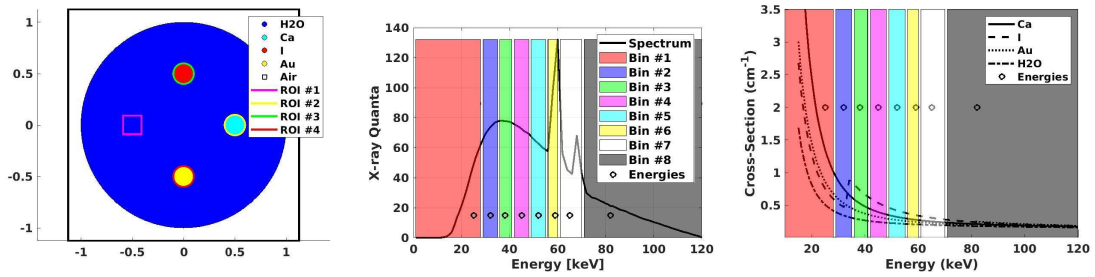

(a) (b) (c)

Figure 6.1: (a) Layout of materials for the four-material model. (b) 120 kVp x-ray source spectrum divided into eight equal count energy bins. (c) Attenuation curves for Ca, I, Au and H2O.

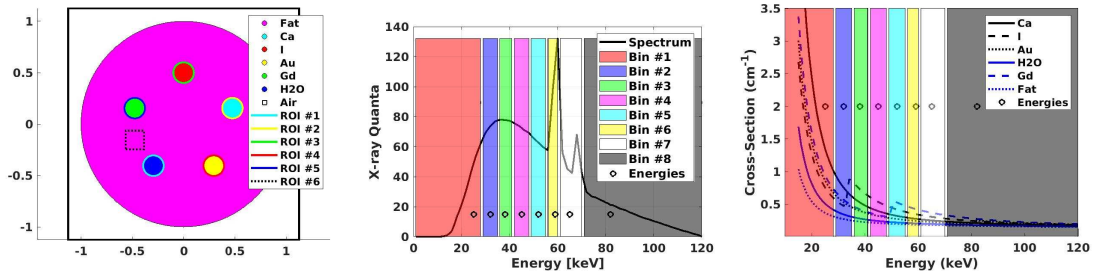

(a) (b) (c)

Figure 6.2: (a) Layout of materials for the six-material model. (b) 120 kVp x-ray source spectrum divided into eight equal count energy bins. (c) Attenuation curves for Ca, I, Au, H2O, Gd and Fat.

[13, 12]. In earlier steps, materials with similar attenuation properties can be grouped together to form a pseudo material. This pseudo material is modeled to have the average attenuation properties of the materials in the group. This step of forming pseudo material groups reduces the number of solution unknowns allowing for the separation of the most distinct material first. In this particular example, we virtually group calcium and gold together to form a pseudo material to first allow for the efficient separation of water which is the most abundant and lowest attenuating material. Next, the contrast agent materials can be separated due to their unique energy-dependent x-ray properties. Finally, the remaining materials can be separated in order of decreasing attenuation. In summary, when decomposing multi-material objects, we find that the following decomposition strategy consistently provides good results:

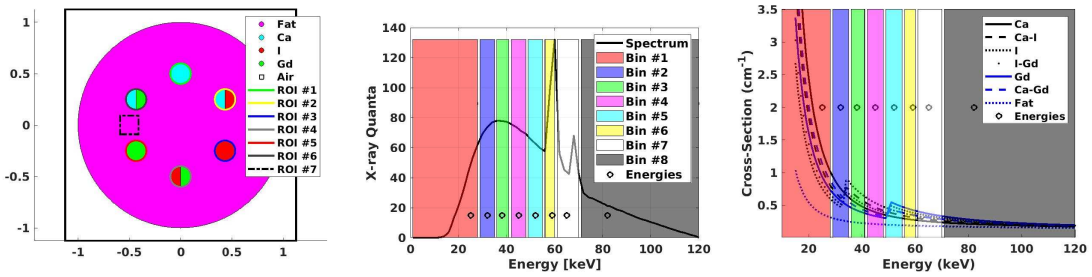

(a) (b) (c)

Figure 6.3: (a) Layout of materials for the four-material, mixed-materials model. (b) 120 kVp x-ray source spectrum divided into eight equal count energy bins. (c) Attenuation curves for Ca, Ca-I, I, I-Gd, Gd, Ca-Gd and Fat.

1. First, focus on accurately recovering the background or most abundant material using low energy bins.

2. Next, decompose materials with K-edges in the diagnostic range in order of decreasing attenuation using energy bins just higher in energy than these K-edge energies.

3. Next, decompose materials without K-edges in the diagnostic range in order of decreasing attenuation using low energy bins.

The first step of a multi-step decomposition for a four-material problem determines the volume fraction of material 1 (water), $\vec{f}_1(\vec{r})$, as seen in

$$\vec{\mu}(E_j, \vec{r}) = \mu_1(E_j)\vec{f}_1(\vec{r}) + \mu_2(E_j)\vec{f}_2(\vec{r}) + \bar{\mu}_{3,4}(E_j)\bar{\vec{f}}_{3,4}(\vec{r}). \tag{6.1}$$

The volume fraction of material 2 (iodine), $\vec{f}_2(\vec{r})$, and the volume fraction of the average of materials 3 and 4 (calcium and gold), $\bar{\vec{f}}_{3,4}(\vec{r})$, are also determined in this step. However, this step is optimized in terms of energy bins used for the separation of material 1, so these other volume fractions are discarded. In Eqn. 6.1, E_j represents the energy values used to calculate the model linear attenuation coefficients, $\mu_1(E_j)$, $\mu_2(E_j)$ and $\bar{\mu}_{3,4}(E_j)$, of materials 1, 2 and the average of 3 and 4, respectively. In the second step, the K-edge agent

of material 2 is separated from the remaining three-material mixture as shown in

$$\vec{\mu}(E_j,\vec{r}) - \mu_1(E_j)\vec{f_1}(\vec{r}) = \mu_2(E_j)\vec{f_2}(\vec{r}) + \bar{\mu}_{3,4}(E_j)\bar{\vec{f}}_{3,4}(\vec{r}). \tag{6.2}$$

The pseudo material with the average attenuation properties of materials 3 and 4 is maintained in this step. In implementing the least squares solution to Eqn. 6.2, one assumes the knowledge of material 1 obtained from step 1 as a prior information as shown on the left-hand side. The solution yields a map of material 2 and a map of the pseudo material for materials 3 and 4, which is discarded when proceeding to the next step. In step 3, we separate the next most attenuating material of material 3 from the remaining two-material mixture as seen in

$$\vec{\mu}(E_j,\vec{r}) - \mu_1(E_j)\vec{f_1}(\vec{r}) - \mu_2(E_j)\vec{f_2}(\vec{r}) = \mu_3(E_j)\vec{f_3}(\vec{r}) + \mu_4(E_j)\vec{f_4}(\vec{r}). \tag{6.3}$$

In the final step, material 4 is refined to improve its decomposition accuracy as displayed in

$$\vec{\mu}(E_j,\vec{r}) - \mu_1(E_j)\vec{f_1}(\vec{r}) - \mu_2(E_j)\vec{f_2}(\vec{r}) - \mu_3(E_j)\vec{f_3}(\vec{r}) = \mu_4(E_j)\vec{f_4}(\vec{r}). \tag{6.4}$$

At each step, the respective equation (Eqn. 6.1, 6.2, 6.3 or 6.4) is solved using multiple energy bin data ($j = 1, 2, ..., 8$) collected via the initial, single acquisition with a PCD. This same original multi-bin data can be reformulated in later steps to reduce the number of bins and improve count statistics. Depending on the problem, a conservation of volume constraint indicating that the domain is comprised of only the known four materials can be included in each step of multi-step and single-step, as described by

$$\sum_{i=1}^{M} \vec{f_i}(\vec{r}) = 1, \tag{6.5}$$

where i is the material index of the M total materials. The left hand side of this constraint equation represents a binary image of the object which has values of one for voxels occupied by the phantom and zero for air only regions. This image serves as the data term for the

conservation of volume constraint. This constraint image can be obtained by measuring the outside dimensions of the object or by thresholding the lowest energy attenuation image. With the addition of Eqn. 6.5, the system of energy based equations (based on Eqn. 6.1, 6.2, 6.3 or 6.4) can be solved for material volume fractions using a bounded variable least squares approach.

In implementing this step-by-step approach, the system of equations solved in each step becomes smaller and better conditioned allowing for the accurate separation of more materials than conventional single-step techniques. This is because most soft-tissue-like materials (such as plastics, fat, muscle, water, etc.) and some contrast agents with similar atomic numbers (such as iodine and barium) possess similar attenuations over the medically relevant energy range. If we represent each material independently in larger matrix for a four or more material problem, we will likely have materials that are linearly related. In this case, the columns of our inversion matrix become nearly linear combinations of one another (or even repeated) and this leads to a nearly singular matrix with a high condition number. This ill-conditioned matrix causes small errors in the observations (attenuation data) to lead to large errors in the parameters (material maps) after inversion. The multi-step method reduces the chance of materials becoming linearly related by grouping like materials and only representing the group rather than each material separately. Therefore, matrix columns should be less linearly related to each other and the matrix will be smaller (have less columns) and better conditioned. In each step of multi-step, the number of unknowns is limited to three or less materials/pseudo materials. Three-material decomposition when considering an object with contrast agents is known to be possible [1].

6.2 Energy Bin Selection Strategy

In accordance with the itemized list shown in Sec. 6 which provides a general formula for the multi-step strategy, the energy bins used in each step of the multi-step algorithm can be selected. We maintain the same material numbering scheme (1 = water, 2 = iodine, 3 = calcium and 4 = gold) and multi-step strategy as described in Sec. 6. As displayed in Fig.

6.1(b), Fig. 6.2(b) and Fig. 6.3(b), the eight energy bins simulated for each of these example problems represent [1,28], [29,35], [36,41], [42,48], [49,55], [56,60], [61,70] and [71,120] keV, respectively. The representative energies corresponding to the median counts within each of these bins are [25,32,38,45,52,59,65,82] keV, respectively. These representative energies were used to determine the linear attenuation coefficients of the inversion matrices used in decomposition. Bin selection rules can follow general trends detailed here, but one must exclude bins with extremely low counts.

For the example detailed above, in step 1, we use only bins 1-3 as there are three unknowns and material 1 has its highest contrast from the remaining materials at low energies. In step 2, we separate material 2 using bins 3 and 4 because these bins are just higher in energy than the K-edge (33.2 keV) where material 2 is the most distinguishable from the remaining materials. In step 3, we use bins 1 and 2 as there are two unknowns and material 2 has its highest contrast at low energies. In the final step, we use only bin 1 and ignore the K-edge of material 4 as we do not have low noise data for energies above this K-edge. When decomposing our experimental phantoms, using nearly all energy bins at all steps provided the best results. The energy-dependent attenuations of each of the materials extracted from data collected from our Medipix3RX detectors is much smoother than that of our simulations because of the limited detector energy resolution. Because of this, there are less identifying features in the data and more energy bins are required to fully capture the energy-dependent behavior of the materials.

6.3 Contrast to Noise Ratio Weighting

Energy bin weighting is performed in each step of the multi-step method to provide high accuracy decompositions with low noise similar to [45, 74, 75, 9]. For any given step, the energy weighting factor is estimated from the CNR of the material under focus estimated for each energy bin. This is a benefit of the multi-step technique that is not possible in a single-step approach. The relationship for calculating the weights for each step based on

the signal and background of the decomposed material is

$$\mathrm{CNR}_j = \frac{\mu_{\mathrm{signal},j} - \mu_{\mathrm{background},j}}{\sqrt{\sigma^2_{\mathrm{signal},j} + \sigma^2_{\mathrm{background},j}}}, \tag{6.6}$$

where j represents the energy bin used for the calculation. In most steps, $\mu_{\mathrm{signal},j}$ and $\sigma^2_{\mathrm{signal},j}$ are treated as the mean and variance in the attenuation in the small region occupied by the material under focus in that step [ROI#2, ROI#3 and ROI#4 for the four-material problem seen in Fig. 6.1(a), ROI#1, ROI#2, ROI#3, ROI#4 and ROI#5 for the six-material problem seen in Fig. 6.2(a) or ROI#1, ROI#3 and ROI#5 for the mixed-material problem seen in Fig. 6.3(a)] and $\mu_{\mathrm{background},j}$ and $\sigma^2_{\mathrm{background},j}$ are the mean and variance in the attenuation in the water or fat based on the primary material of the phantom cylinder. When decomposing the water or fat, $\mu_{\mathrm{signal},j}$ and $\sigma^2_{\mathrm{signal},j}$ are taken as the mean and variance in the water or fat and $\mu_{\mathrm{background},j}$ and $\sigma^2_{\mathrm{background},j}$ are taken as the mean and variance in the region surrounding the phantom. The entire water or fat region was used in the calculation of all weights. These CNRs form the diagonal elements of a weighting matrix which is applied to the inversion matrix and the attenuation data during the least squares solution. In practice, these weights can be computed from calibration vials included in the field of view during the acquisition of the unknown decomposition phantom. ROIs selected within reconstructed slices of these calibration vials can be used to define CNR weights as well as calibrated basis functions for the decomposition of the unknown object.

The resulting decomposed material maps after each decomposition step were thresholded to reduce noise in the results. More aggressive threshold application is justified in the first step of multi-step because this step decomposes the background which is assumed to be a pure material with a uniform volume fraction of one. Less aggressive application of thresholds is performed on the other material maps to reduce the impact of noise. Not using thresholds would slightly increase the quantitative errors in both single-step and multi-step, but overall the multi-step method still yields better results than single-step.

6.4 Quantitative Analysis Metrics

The material decomposition results were first evaluated qualitatively by visual inspection to make sure they were logical. This preliminary analysis was followed by a more rigorous investigation using quantitative metrics. Quantitation was assessed based on four criteria: percent error (PE), CNR, noise standard deviation (NSD) and accuracies with confidence intervals (ACIs). The relationship for calculating PE is

$$\mathrm{PE}_{\mathrm{ROI},i} = \frac{|f_{\mathrm{ROI},i} - f_{\mathrm{ROI},i,\mathrm{true}}|}{f_{\mathrm{ROI},i,\mathrm{true}}} \times 100\%, \tag{6.7}$$

where $f_{\mathrm{ROI},i}$ represents the mean volume fraction in region of interest (ROI) i and $f_{\mathrm{ROI},i,\mathrm{true}}$ represents the true volume fraction in ROI i. In the case of PEs calculated in regions of a material map not occupied by said material, the volume fraction, $f_{\mathrm{ROI},i}$, in percent is reported as the PE rather than through computation using Eqn. 6.7. The relationship for calculating CNR is

$$\mathrm{CNR}_{\mathrm{ROI},i} = \frac{f_{\mathrm{ROI},i} - f_{\mathrm{Rest}}}{\sqrt{\sigma^2_{\mathrm{ROI},i} + \sigma^2_{\mathrm{Rest}}}}, \tag{6.8}$$

where $\sigma^2_{\mathrm{ROI},i}$ represents the variance in the volume fractions in ROI i and σ^2_{Rest} represents the variance in the volume fractions of the rest of the image. For the background region, only the square ROIs [Fig. 6.1(a), 6.2(a) and 6.3(a)] were used to calculate the mean and variance for ROI i, but the remaining background material region was excluded from the calculations of the mean and variance of the rest of the image. The relationship for calculating NSD is

$$\mathrm{NSD}_{\mathrm{ROI},i} = \sqrt{\frac{1}{V-1}\sum_{v=1}^{V}(f_{\mathrm{ROI},v,i} - \bar{f}_{\mathrm{ROI},i})^2} \times 100\%, \tag{6.9}$$

where V is the number of voxels in ROI i indexed by v and $\bar{f}_{\mathrm{ROI},i}$ is the mean volume fraction in ROI i. For some of the experimental results, accuracies and corresponding confidence intervals are presented. These accuracies are either presented in percent with the corresponding confidence intervals also in percent and as densities [g/mL] with the

corresponding confidence intervals in units of density. The confidence interval is calculated as

$$\left(\bar{x} - t^* \frac{s}{\sqrt{n}}, \bar{x} + t^* \frac{s}{\sqrt{n}}\right), \tag{6.10}$$

where $\bar{x}$ is the sample mean, s is the sample standard deviation and n is the sample size. These three parameters were calculated from the material regions of one slice of the phantoms. t^* represents the critical value extracted from the t-distribution table. Here we use the two-sided t-distribution assuming a 95% confidence level and number of degrees of freedom equal to $n - 1$.

In the experimental results presented in Chap. 7, the entire background region was used in the computation of all PEs, CNRs, NSDs and ACIs. For the five-material phantoms, ROIs were defined based on the five materials of the phantom. ROI#1 encompassed the entire ABS plastic background region. ROI#2 through ROI#5 were defined as circular regions within each of the materials (ROI#2 = I, ROI#3 = Gd, ROI#4 = HA, ROI#5 = H2O). The ROIs were used in both the CNR weighting and analysis of results for these five-material problems.

6.5 Multi-Material Phantom Results from Synthetic Data

6.5.1 Four-Material Phantom

The model geometry consists of a 2 cm diameter cylinder of water with 2 mm diameter columns of calcium, iodine and gold. The background is pure water and the concentrations of calcium, iodine and gold are 140 mg/mL, 18 mg/mL and 8 mg/mL, respectively. A diagram of the four-material problem can be seen in Fig. 6.1(a) along with the ROIs used in the analysis of the results. For comparison, the results of the new multi-step method will be compared with the results of the single-step method.

The decomposition problem was solved with single-step in accordance with Eqn. 5.6 and with multi-step in accordance with Eqn. 6.1, 6.2, 6.3 and 6.4. For this problem, the

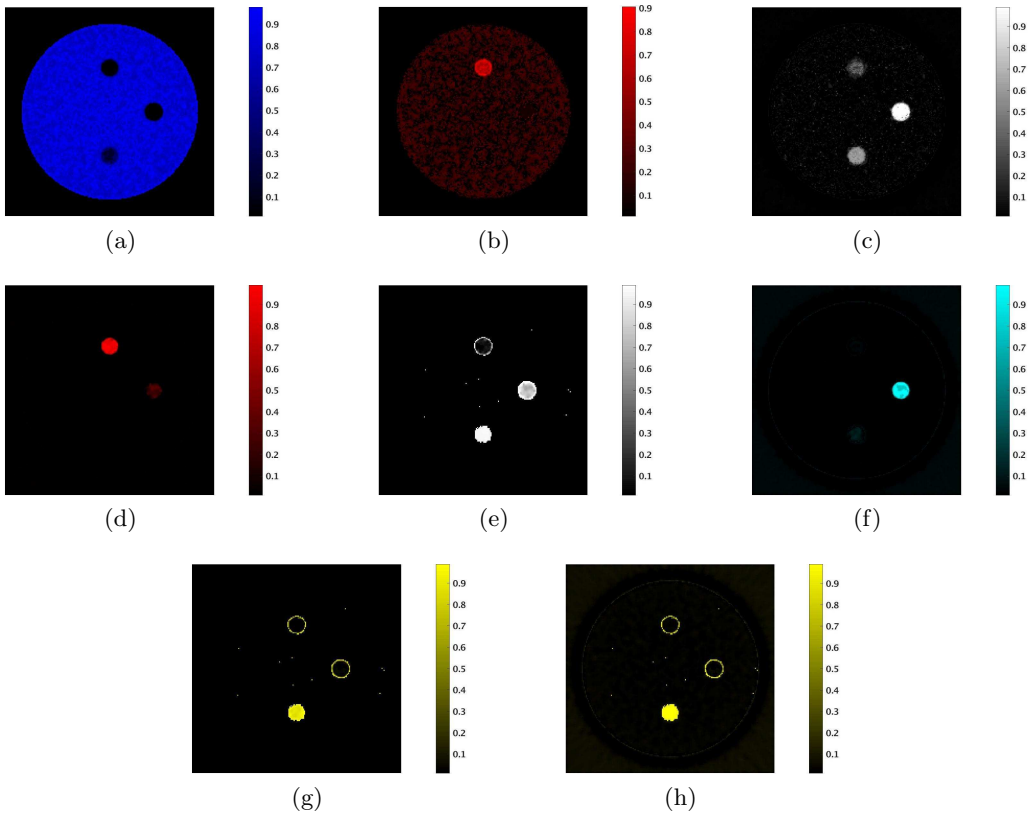

Figure 6.4: Material maps resulting from each step of multi-step material decomposition for the four-material problem.

background material water is material 1, iodine is material 2, calcium is material 3 and gold is material 4. After each step of multi-step and single-step, a threshold was applied to reduce the impact of noise and improve the decomposition results. Thresholds of 0.25 and 0.75 were used for steps 2, 3 and 4 of multi-step and for all material maps of single-step. A threshold of 0.6 was used for the first step of multi-step.

Figure 6.1 shows the energy bins chosen based on equal mean flat-field counts overlaid on (b) the x-ray source spectrum and (c) linear attenuation curves for the four materials in this problem. The representative energies for each bin are also displayed as the open circles. These linear attenuation curves were generated based on the maximum concentrations expected in the sample. This knowledge would be available to the experimenter as they would know the base concentration injected into the patient. This kind of *a priori* information is essential to the success of most decomposition techniques as it reduces the

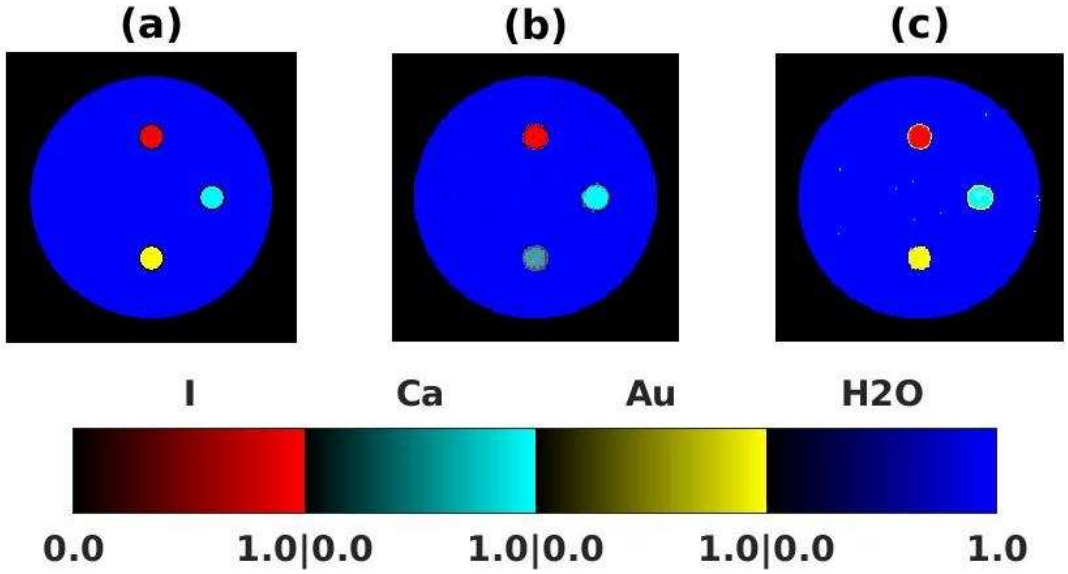

Figure 6.5: Color coded (a) ground truth, (b) single-step decomposition results and (c) multi-step decomposition results for the four-material problem.

solution space to a manageable set of likely solutions. All material maps generated during the multi-step material decomposition process can be seen in Fig. 6.4. (a), (b) and (c) are the water map (under focus), the iodine map (discarded) and the average of calcium and gold map (discarded) from step 1, respectively. (d) and (e) are the iodine map (under focus) and the average of calcium and gold map (discarded) from step 2, respectively. (f) and (g) are the calcium map (under focus) and the gold map (discarded) from step 3, respectively. (h) is the gold map (under focus) from step 4. These results correspond to the ground truth image shown in Fig. 6.5(a). The combined final results for multi-step can be seen in Fig. 6.5(c). The energy bins and bin weighting used in each step are optimized for the focus material of that decomposition step. This leads to improvement in the iodine region from steps 1 [Fig. 6.4(b)] to 2 [Fig. 6.4(d)] and the gold region from steps 3 [Fig. 6.4(g)] to 4 [Fig. 6.4(h)] because of this optimal weighting. Energy bin weighting based on the water region was conducted for the single-step results shown in Fig. 6.5(b) for the sake of comparison.

The combined final results for the four-material problem for single-step and multi-step can be seen in Fig. 6.5 and the quantitation can be seen in Tab. 6.1 and 6.2. Table

Table 6.1: PEs in each ROI (ROI#1, ROI#2, ROI#3, ROI#4) for single-step and multi-step for the four-material problem.

	Single-Step	Multi-Step
Water Map	**0.2**, 0.1, 1.6, 37.4	**0.0**, 0.0, 0.0, 7.8
Calcium Map	0.0, **5.6**, 0.0, 22.9	0.0, **6.4**, 0.0, 0.0
Iodine Map	0.0, 0.0, **8.3**, 0.0	0.0, 8.9, **11.7**, 0.0
Gold Map	0.0, 3.1, 0.5, **70.3**	0.0, 6.3, 11.2, **7.8**

6.1 displays percent errors (PEs) in the calculated volume fractions of each ROI (ROI#1, ROI#2, ROI#3, ROI#4) for each material map generated using the single-step and multi-step material decomposition techniques for the four-material problem described in Fig. 6.1. The bold values are of most interest as these represent the percent errors in a material ROI in its respective map. Table 6.2 displays the contrast to noise ratios (CNRs) and noise standard deviations (NSDs) in percent in each ROI (ROI#1, ROI#2, ROI#3, ROI#4) for each material map generated using the single-step and multi-step material decomposition techniques for the four-material problem described in Fig. 6.1. The bold values are of most interest as these represent the CNRs and NSDs in a material ROI in its respective map. The multi-step method clearly outperforms the single-step method. This can be seen in the gold region in Fig. 6.5 and in the percent errors in Tab. 6.1. The percent error is 70.3% for single-step versus 7.8% for multi-step. By examining the images in Fig. 6.5 and the CNRs in Tab. 6.2, we can see an improvement in noise, especially in the water region. This is evidenced by a CNR of 20.8 for single-step versus 32.9 for multi-step. Also, the weighted matrices of linear attenuation coefficients for the four-material problem do indeed become better conditioned as the condition numbers are 21161 for single-step versus 152, 134, 73 and 1 for the four consecutive steps of the multi-step method. The computational times in seconds for single-step and multi-step for the four-material problem are 93.3 and 235.5, respectively.

6.5.2 Benefits of Material Map Thresholding

To investigate the impact of thresholding in decomposition, we examine the decomposition results for the four-material problem with and without thresholding in Fig. 6.6. In this

Table 6.2: CNRs and NSDs in each ROI (ROI#1, ROI#2, ROI#3, ROI#4) for single-step and multi-step for the four-material problem.

	Single-Step		Multi-Step	
	CNR	NSD	CNR	NSD
Water Map	**20.8**	**2.3**, 1.8, 7.5, 5.7	**32.9**	**0.0**, 0.0, 0.0, 26.9
Calcium Map	**6.6**	0.0, **14.0**, 0.0, 13.6	**5.8**	0.0, **16.0**, 0.0, 0.0
Iodine Map	**5.2**	0.0, 0.0, **17.5**, 0.0	**3.5**	0.0, 13.9, **25.0**, 0.0
Gold Map	**12.8**	0.0, 9.0, 3.5, **1.3**	**3.4**	0.0, 16.2, 24.1, **26.9**

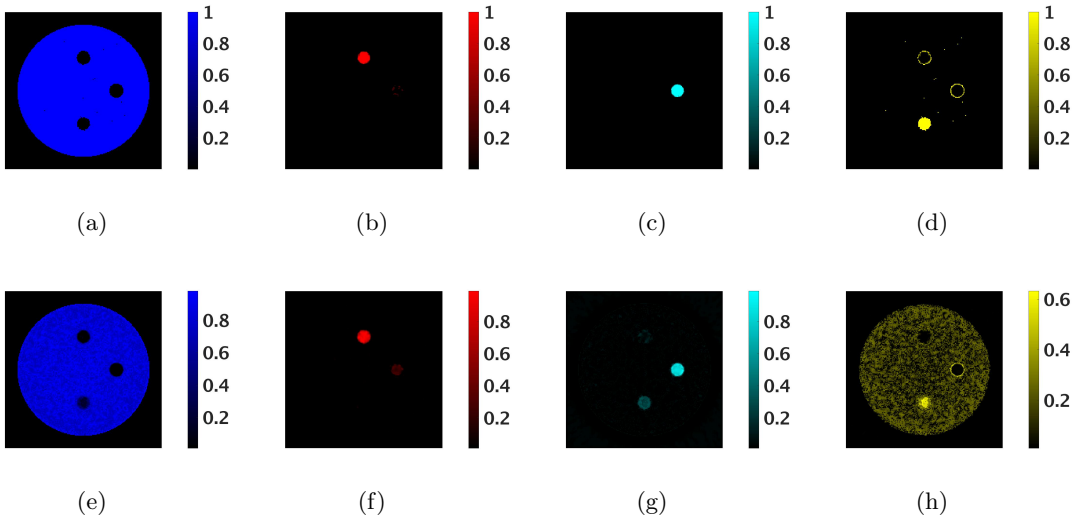

Figure 6.6: (a), (b), (c) and (d) represent the multi-step decomposition results with thresholding. (e), (f), (g) and (h) represent the multi-step decomposition results without thresholding.

figure, (a) and (e) represent the water map, (b) and (f) represent the iodine map, (c) and (g) represent the calcium map and (d) and (h) represent the gold map. From Fig. 6.6, it can be noticed that the noise in the water region of both the water and gold maps is nearly eliminated after thresholding. Also, the errors in the separation of iodine and calcium and calcium and gold are also reduced through thresholding.

6.5.3 Six-Material Phantom

A six-material case was chosen to display the ability of the method to handle more challenging decomposition problems. Here, gadolinium and adipose are added to the model. Gadolinium is another contrast agent with a K-edge. Adipose is a low contrast material significant to the breast imaging problem. In this problem, the background was adipose and

water was made one of the columns. The adipose background was 2 cm in diameter and the columns of all other materials were 2 mm in diameter. The concentration of gadolinium was 18 mg/mL. The adipose material properties were collected from ICRU-44 [97]. A diagram of this six-material problem can be seen in Fig. 6.2(a) along with the ROIs used to compute the quantitative results.

A similar approach of decomposing the background first, followed by the contrast agents and then the remaining materials was taken to achieve the goal of accurate separation of all six materials. A description of the material maps acquired in each step of multi-step material decomposition for the six-material problem along with the energy bins used can be seen in the flowchart in Fig. 6.7. In this figure, blue arrows indicate inputs to decomposition steps and red arrows indicate outputs of decomposition steps. The key describing the inputs, outputs and steps of the decomposition can be seen below the flowchart. The discarded material maps labeled with multiple materials represent a single pseudo material map representing the average of the group. The colored material maps represent the material under focus during the current decomposition step which are maintained throughout the process as final results. The materials are decomposed in the following order: (1) adipose, (2) iodine, (3) gadolinium, (4) calcium, (5) gold and (6) water. In early steps, iodine and gadolinium are grouped together and calcium, gold and water are grouped together to reduce the number of unknowns and provide a better conditioned system of equations. Examination of the attenuation curves for these six materials, shown in Fig. 6.2(c), justifies the order that we separate materials and the energy bins used in each step. In the first step, we have three unknowns and the most distinct material, adipose, has its highest contrast from the other materials at low energies. For this reason, we choose the three lowest energy bins. In the second step, we separate iodine which has its highest contrast for energy values slightly above its K-edge. For this reason, we choose bins 3, 4 and 5 for step 2. Gadolinium has its highest contrast above its K-edge, so we choose bins 6 and 7 for step 3. There are only two unknowns in step 3, so we choose only two energy bins. Calcium is the highest attenuating material of the remaining materials and its contrast is highest at

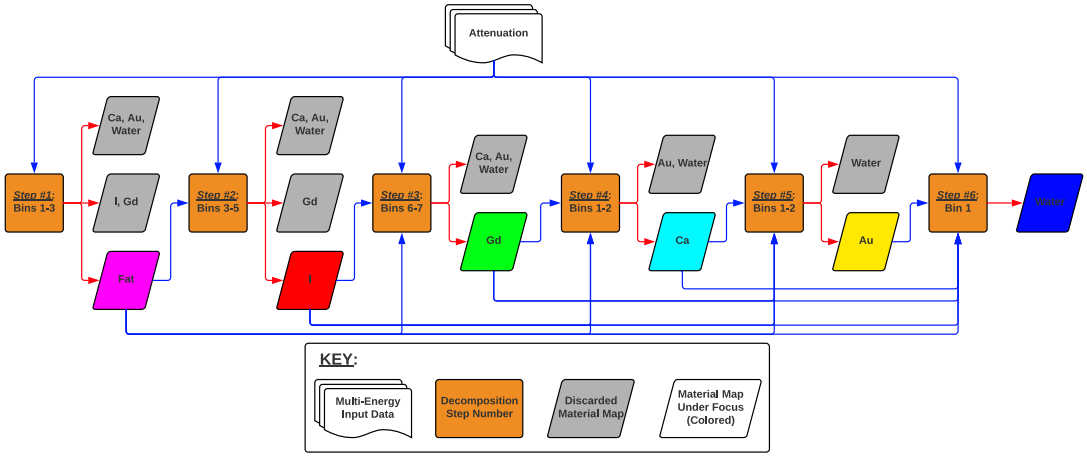

Figure 6.7: Flowchart describing the steps of a multi-step material decomposition for the six-material problem.

low energies, so we use bins 1 and 2 for step 4. Gold is the next most attenuating material and has its highest contrast at low energies, so we again choose bins 1 and 2 for this step. Finally, we choose bin 1 for water as it is the lowest attenuating material with maximum contrast at low energies. The same conservation of volume constraint seen in Eqn. 6.5 was applied to each step of the six-material problem. Bounded variable least squares was again used to solve this inverse problem. Bounds of zero and one were applied to all of the unknowns. Thresholds were again applied after each step of the multi-step process and to the single-step results used for comparison. A threshold of 0.85 was used for the first step of multi-step and thresholds of 0.25 and 0.75 were applied to all other steps of multi-step and to all material maps of single-step.

All material maps generated during the multi-step material decomposition process are shown in Fig. 6.8. (a), (b) and (c) are the adipose map (under focus), the average of iodine and gadolinium map (discarded) and the average of calcium, gold and water map (discarded) from step 1, respectively. (d), (e) and (f) are the iodine map (under focus), the gadolinium map (discarded) and the average of calcium, gold and water map (discarded) from step 2, respectively. (g) and (h) are the gadolinium map (under focus) and the average of calcium, gold and water map (discarded) from step 3, respectively. (i) and (j) are the calcium map (under focus) and the average of gold and water map (discarded) from step

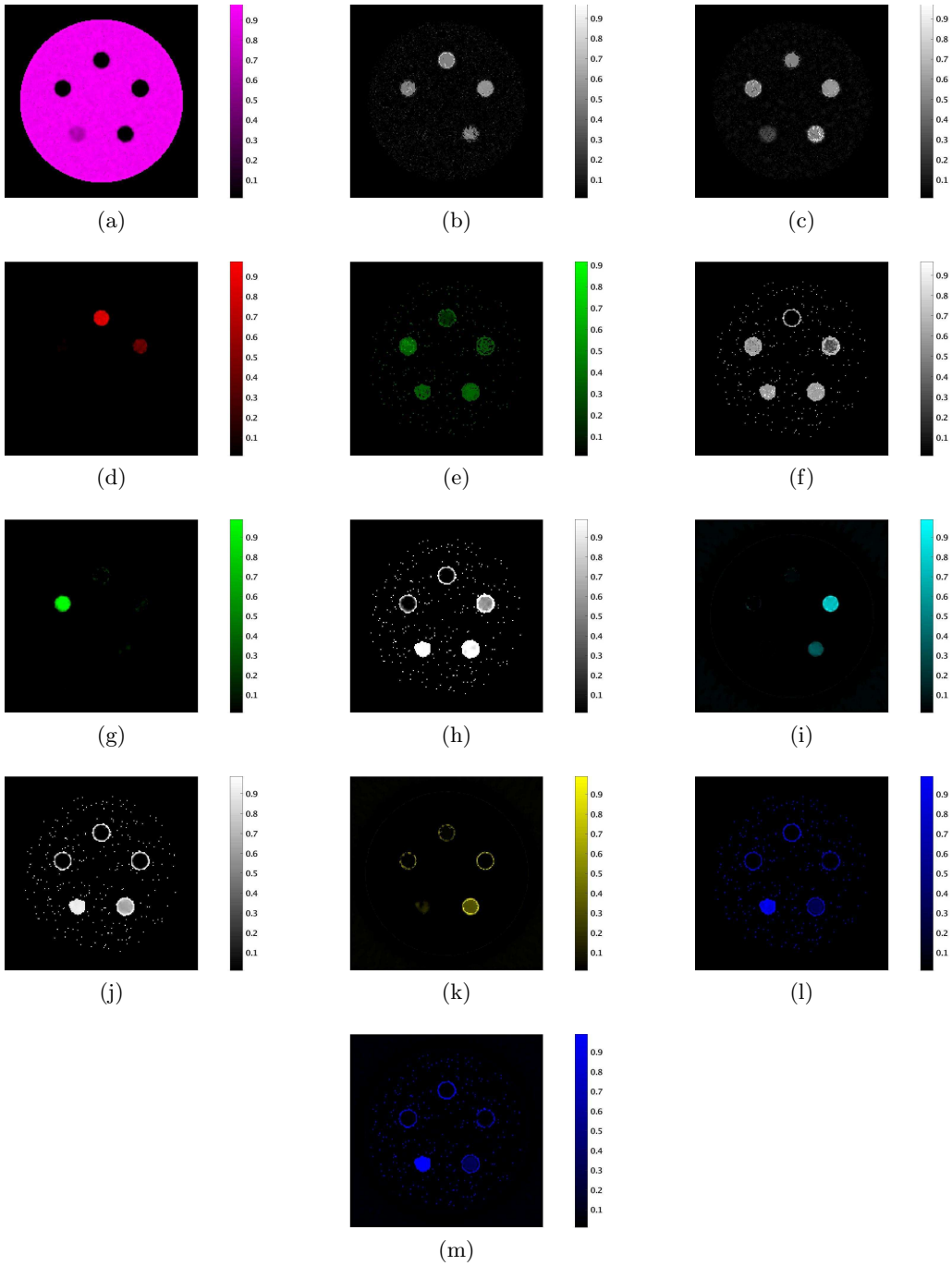

Figure 6.8: Material maps resulting from each step of multi-step material decomposition for the six-material problem.

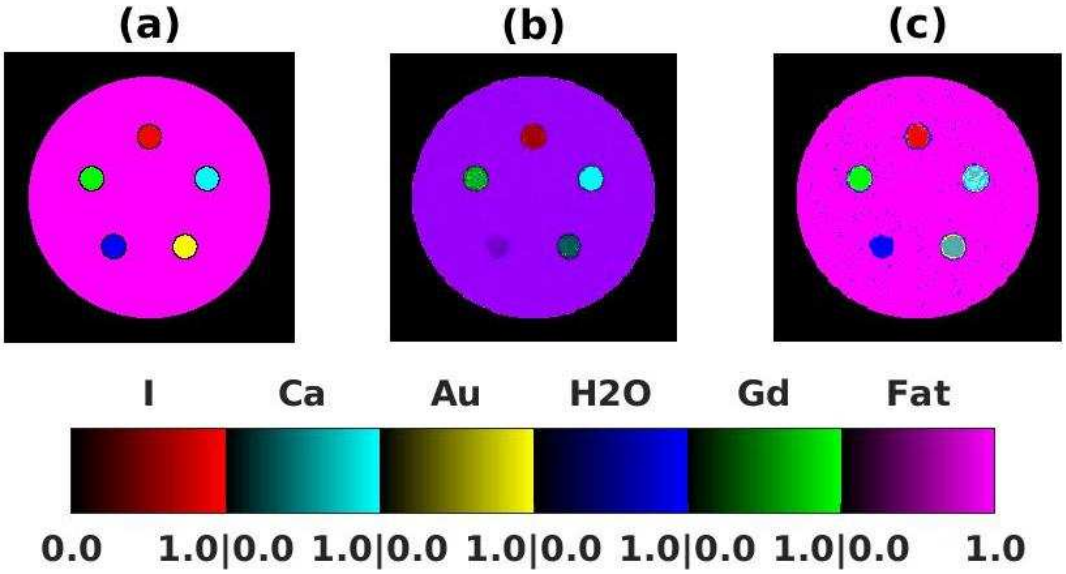

Figure 6.9: Color coded (a) ground truth, (b) single-step decomposition results and (c) multi-step decomposition results for the six-material problem.

4, respectively. (k) and (l) are the gold map (under focus) and the water map (discarded) from step 5, respectively. (m) is the water map (under focus) from step 6. The results shown here correspond to the ground truth image shown in Fig. 6.9(a). The combined final results for multi-step can be seen in Fig. 6.9(c). Similar to the four-material problem, the energy bins and bin weighting used in each step are optimized for the focus material of that decomposition step. This leads to improvement in the gadolinium region from steps 2 [Fig. 6.8(e)] to 3 [Fig. 6.8(g)] and the water region from steps 5 [Fig. 6.8(l)] to 6 [Fig. 6.8(m)] because of this optimal weighting. Energy bin weighting based on the adipose region was conducted for the single-step results shown in Fig. 6.9(b).

The combined final results for the six-material problem for single-step and multi-step can be seen in Fig. 6.9 and the quantitation can be seen in Tab. 6.3 and 6.4. Table 6.3 displays percent errors (PEs) in the calculated volume fractions of each ROI (ROI#1, ROI#2, ROI#3, ROI#4, ROI#5, ROI#6) for each material map generated using the single-step and multi-step material decomposition techniques for the six-material problem described in Fig. 6.2. The bold values are of most interest as these represent the percent errors in a material ROI in its respective map. Table 6.4 displays the contrast to noise ratios

Table 6.3: PEs in each ROI (ROI#1, ROI#2, ROI#3, ROI#4, ROI#5, ROI#6) for single-step and multi-step for the six-material problem.

	Single-Step	Multi-Step
Water Map	**64.4**, 0.0, 0.0, 2.3, 0.0, 38.7	**7.2**, 4.2, 6.2, 30.2, 3.9, 2.5
Calcium Map	0.0, **6.4**, 0.1, 28.9, 10.3, 0.0	0.0, **15.8**, 0.0, 25.4, 0.1, 0.0
Iodine Map	0.0, 0.0, **34.9**, 0.0, 0.0, 0.0	0.0, 28.9, **12.3**, 0.0, 0.0, 0.0
Gold Map	0.0, 0.1, 0.0, **99.4**, 0.0, 0.0	0.0, 1.3, 4.7, **55.2**, 6.1, 0.0
Gadolinium Map	0.0, 0.0, 0.0, 0.0, **46.3**, 0.0	0.0, 0.0, 0.7, 0.0, **10.6**, 0.0
Adipose Map	47.8, 0.0, 0.5, 3.5, 0.6, **39.8**	7.2, 0.0, 0.0, 0.0, 0.0, **2.5**

(CNRs) and noise standard deviations (NSDs) in percent in each ROI (ROI#1, ROI#2, ROI#3, ROI#4, ROI#5, ROI#6) for each material map generated using the single-step and multi-step material decomposition techniques for the six-material problem described in Fig. 6.2. The bold values are of most interest as these represent the CNRs and NSDs in a material ROI in its respective map. It is also clear for the six-material case that the multi-step method outperforms the single-step method. This can be seen in nearly all regions in Fig. 6.9 and in the percent errors in Tab. 6.3. For example, the percent error for water is 64.4% for single-step versus 7.2% for multi-step. The percent error for adipose is 39.8% for single-step versus 2.5% for multi-step. Error propagates from step to step in the multi-step process. Problems with more materials and hence more steps, have more error especially in later decomposition steps. This also results in decreased CNRs in later steps. The six-material case also displays similar noise properties for the two methods as evidenced by Fig. 6.9 and the CNRs in Tab. 6.4. This is evidenced by an average CNR of the six material regions of 4.1 for single-step versus 4.0 for multi-step. Water is separated first in the four-material case with more aggressive thresholding and last in the six-material case with less aggressive thresholding. The noise in the water region is very different between the two problems after this thresholding and this explains why the CNRs for water in both problems are so different. And again, the weighted matrices of linear attenuation coefficients for the six-material problem become better conditioned as the condition numbers are 9737867 for single-step versus 669, 403, 183, 37, 86 and 1 for the six consecutive steps of multi-step. The computational times in seconds for single-step and multi-step for the six-material problem are 97.2 and 288.2, respectively.

Table 6.4: CNRs and NSDs in each ROI (ROI#1, ROI#2, ROI#3, ROI#4, ROI#5, ROI#6) for single-step and multi-step for the six-material problem.

	Single-Step		Multi-Step	
	CNR	NSD	CNR	NSD
Water Map	**0.8**	**1.7**, 0.0, 0.0, 7.6, 0.0, 1.5	**3.2**	**26.0**, 11.2, 18.0, 13.4, 13.3, 15.6
Calcium Map	**5.7**	0.0, **16.2**, 2.0, 12.6, 14.3, 0.0	**5.0**	0.0, **16.8**, 0.0, 14.3, 2.0, 0.0
Iodine Map	**4.7**	0.0, 0.0, **14.0**, 0.0, 0.0, 0.0	**3.6**	0.0, 16.4, **24.5**, 0.0, 0.0, 0.0
Gold Map	**0.2**	0.0, 1.8, 0.0, **3.8**, 0.0, 0.0	**1.9**	0.0, 5.9, 11.8, **23.8**, 14.2, 0.0
Gadolinium Map	**2.7**	0.0, 0.0, 0.0, 0.0, **20.0**, 0.0	**4.3**	0.0, 0.0, 4.5, 0.0, **20.6**, 0.0
Adipose Map	**10.7**	3.1, 0.0, 3.8, 9.6, 4.1, **1.6**	**6.1**	26.0, 0.0, 0.0, 0.0, 0.0, **15.6**

6.5.4 Four-Material, Mixed-Materials Phantom

To display the ability of the multi-step method to handle a problem where different materials are mixed together in different concentrations, we show a four-material, mixed material problem. In this problem, there are six contrast elements embedded in an adipose background as shown in the ground truth image in Fig. 6.3(a). Starting from the top material and working around the circular array clockwise the mixtures are: 140 mg/mL calcium in water, 70 mg/mL calcium / 9 mg/mL iodine in water, 18 mg/mL iodine in water, 9 mg/mL iodine / 9 mg/mL gadolinium in water, 18 mg/mL gadolinium in water and 70 mg/mL calcium / 9 mg/mL gadolinium in water. The adipose material properties were again collected from ICRU-44 [97]. The corresponding 120 kVp spectrum and linear attenuation curves for these materials are shown in Fig. 6.3(b) and 6.3(c). Similar to the six-material problem the materials were decomposed in the following order: (1) adipose, (2) iodine, (3) gadolinium and (4) calcium. A description of the steps of the multi-step method and energy bins used at each step for the four-material, mixed-material problem are shown in Fig. 6.10. In this figure, blue arrows indicate inputs to decomposition steps and red arrows indicate outputs of decomposition steps. The key describing the inputs, outputs and steps of the decomposition can be seen below the flowchart. The discarded material maps labeled with multiple materials represent a single pseudo material map representing the average of the group. The colored material maps represent the material under focus during the current decomposition step which are maintained throughout the process as final results. The maximum concentrations of calcium, iodine and gadolinium mentioned

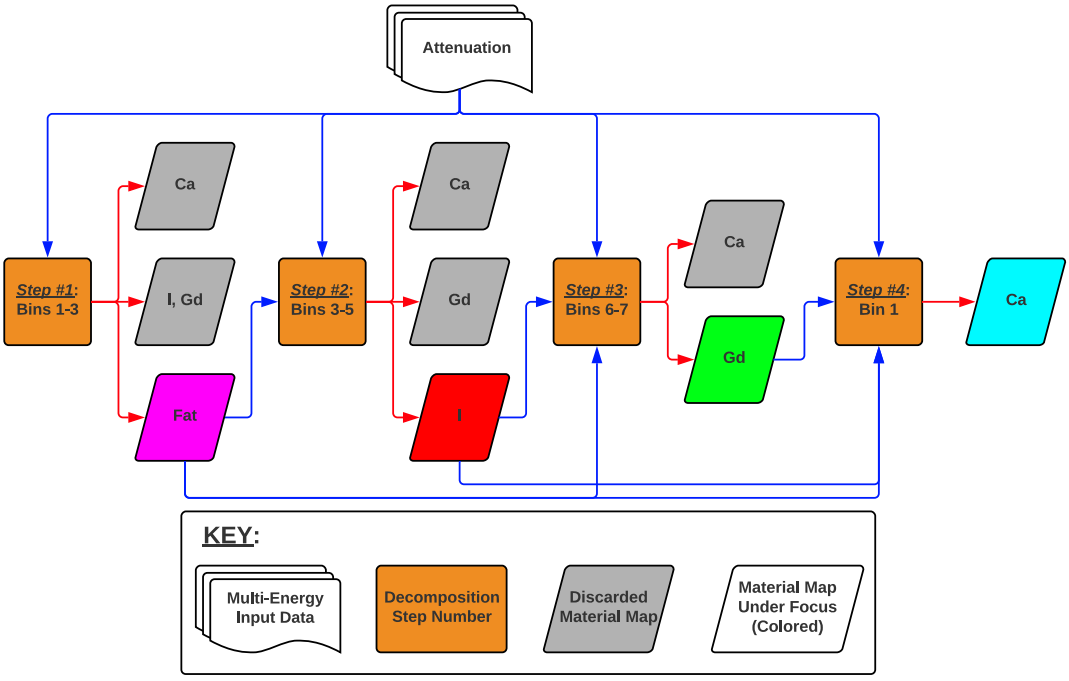

Figure 6.10: Flowchart describing the steps of a multi-step material decomposition for the four-material, mixed-materials problem.

above were used as basis functions and weighting based on the CNRs of these material regions was used during the weighted least squares solution. Since similar materials and concentrations to the six-material problem were used in this mixed-material problem, a similar decomposition strategy was employed. The three groups of the background, the contrast agents with K-edges and the non-contrast agents were maintained in this problem. Energy bins were again selected to maximized contrast between the focus material and the remaining, undecomposed materials. The same conservation of volume constraint seen in Eqn. 6.5 was applied to each step of this mixed-material problem. Bounded variable least squares was used to solve this inverse problem. Bounds of zero and one were applied to all of the unknowns. A threshold of 0.6 was applied to the adipose map after the first step of the multi-step process and thresholds of 0.25 and 0.75 were applied to the adipose map of the single-step results used for comparison. No other thresholds were applied during the solution of other steps of the multi-step method or to any of the other maps of single-step.

All material maps generated during the multi-step material decomposition process can

be seen in Fig. 6.11. (a), (b) and (c) are the adipose map (under focus), the average of iodine and gadolinium map (discarded) and the calcium map (discarded) from step 1, respectively. (d), (e) and (f) are the iodine map (under focus), the gadolinium map (discarded) and the calcium map (discarded) from step 2, respectively. (g) and (h) are the gadolinium map (under focus) and the calcium map (discarded) from step 3, respectively. (i) is the calcium map (under focus) from step 4. These results correspond to the ground truth image shown in Fig. 6.12(a). The combined final results for multi-step can be seen in Fig. 6.12(c). Similar to the six-material problem, the energy bins and bin weighting used in each step are optimized for the focus material of that decomposition step. This leads to improvement in the gadolinium region from steps 2 [Fig. 6.11(e)] to 3 [Fig. 6.11(g)] and the calcium regions from earlier steps 1-3 [Fig. 6.11(c), 6.11(f) and 6.11(h)] and 4 [Fig. 6.11(i)] because of this optimal weighting. Energy bin weighting based on the adipose region was conducted for the single-step results shown in Fig. 6.12(b).

The combined final results for the four-material, mixed-material problem for single-step and multi-step are displayed in Fig. 6.12 and the quantitation are shown in Tab. 6.5, 6.6 and 6.7. Table 6.5 displays percent errors (PEs) in the calculated volume fractions of each ROI (ROI#1, ROI#2, ROI#3, ROI#4, ROI#5, ROI#6, ROI#7) for each material map generated using the single-step and multi-step material decomposition techniques for the four-material, mixed-materials problem described in Fig. 6.3. The bold values are of most interest as these represent the percent errors in a material ROI in its respective map. Table 6.6 displays the contrast to noise ratios (CNRs) in the form CNR (ROI#) that correspond to a particular material in its respective material map generated using the single-step and multi-step material decomposition techniques for the four-material, mixed-materials problem described in Fig. 6.3. The ROI# listed next to each CNR and the rest of the image not containing the material of interest are used to calculate the CNR for each material region in accordance with Eqn 6.8. Table 6.7 displays the noise standard deviations (NSDs) in percent in each ROI (ROI#1, ROI#2, ROI#3, ROI#4, ROI#5, ROI#6, ROI#7) for each material map generated using the single-step and multi-step material decomposition

Table 6.5: PEs in each ROI (ROI#1, ROI#2, ROI#3, ROI#4, ROI#5, ROI#6, ROI#7) for single-step and multi-step for the four-material, mixed-materials problem.

	Single-Step	Multi-Step
Adipose Map	1.6, 3.4, 4.5, 5.4, 8.1, 4.6, **0.0**	0.0, 0.0, 0.0, 0.5, 0.4, 0.0, **0.0**
Calcium Map	**9.2**, **1.7**, 11.8, 19.8, 23.4, **13.1**, 0.3	**10.5**, **4.6**, 16.4, 19.3, 14.4, **9.7**, 1.1
Iodine Map	0.2, **30.4**, **33.0**, **11.8**, 2.3, 5.2, 4.7	17.4, **5.9**, **25.0**, **24.2**, 1.1, 2.3, 1.0
Gadolinium Map	6.6, 23.6, 15.1, **18.7**, **40.6**, **26.6**, 1.7	1.4, 1.5, 3.2, **1.3**, **17.2**, **11.8**, 1.0

Table 6.6: CNRs in the form CNR (ROI#) generated using single-step and multi-step for the four-material, mixed-materials problem.

	Single-Step	Multi-Step
Adipose Map	**28.5** (#7)	**97.6** (#7)
Calcium Map	**6.4** (#1), **4.9** (#2), **5.0** (#6)	**12.0** (#1), **5.1** (#2), **6.3** (#6)
Iodine Map	**3.6** (#2), **5.4** (#3), **4.6** (#4)	**2.2** (#2), **2.9** (#3), **2.0** (#4)
Gadolinium Map	**5.5** (#4), **3.3** (#5), **6.1** (#6)	**2.7** (#4), **3.5** (#5), **2.3** (#6)

techniques for the four-material, mixed-materials problem described in Fig. 6.3. The bold values are of most interest as these represent the NSDs in a material ROI in its respective map. It is also clear for this mixed-material case that the multi-step method outperforms the single-step method. This can be seen in the calcium and gadolinium regions which are incorrectly identified in the single-step method, but correctly identified in the multi-step method as shown in Fig. 6.12 and in the percent errors in Tab. 6.5. Out of the ten most significant regions (shown in bold in Tab. 6.5), six show a decrease in error, one remains the same and three show an increase in error from single-step to multi-step. Because this problem only has four materials and four steps, less error propagates through the solution and lower errors and higher CNRs can be achieved than the six-material problem. The mixed-material case also displays a similar improvement in noise as evidenced by Fig. 6.12 and the CNRs in Tab. 6.6. This is evidenced by an increase in CNR in the adipose region for multi-step over the single-step baseline. In this case, the weighted matrices of linear attenuation coefficients for the mixed-material problem remain similarly conditioned as the condition numbers are 577 for single-step versus 549, 988, 297, and 1 for the four consecutive steps of multi-step. The computational times in seconds for single-step and multi-step for this mixed-material problem are 92.5 and 237.7, respectively.

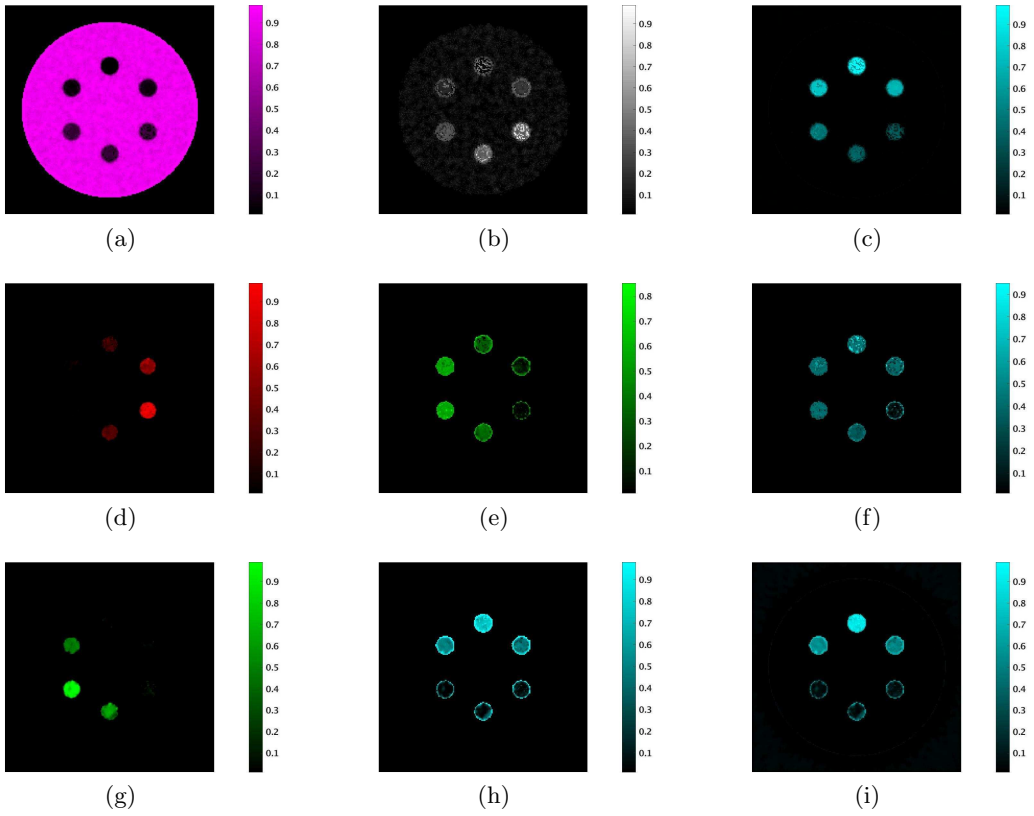

Figure 6.11: Material maps resulting from each step of multi-step material decomposition for the four-material, mixed-materials problem.

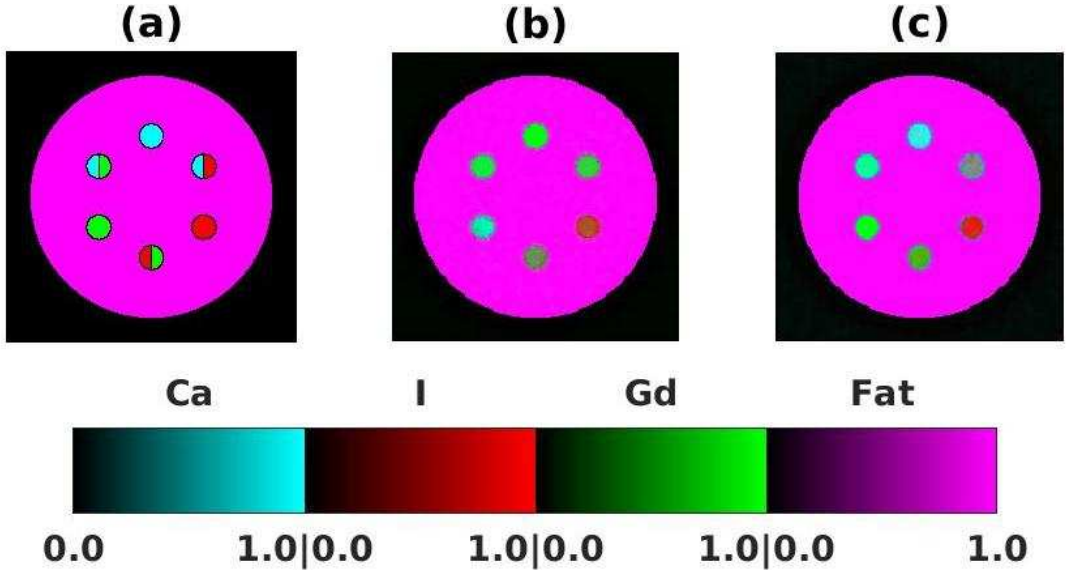

Figure 6.12: Color coded (a) ground truth, (b) single-step decomposition results and (c) multi-step decomposition results for the four-material, mixed-materials problem.

Table 6.7: NSDs in each ROI (ROI#1, ROI#2, ROI#3, ROI#4, ROI#5, ROI#6, ROI#7) for single-step and multi-step for the four-material, mixed-materials problem.

	Single-Step	Multi-Step
Adipose Map	7.2, 10.6, 12.1, 13.1, 16.8, 12.2, **0.0**	0.0, 0.0, 0.0, 6.8, 6.7, 0.0, **0.0**
Calcium Map	**13.7**, **9.9**, 5.1, 5.2, 7.1, **12.3**, 0.8	**5.6**, **9.5**, 14.7, 16.2, 13.7, **8.1**, 0.3
Iodine Map	1.1, **3.8**, **11.5**, **7.2**, 4.5, 3.7, 1.7	11.0, **19.4**, **25.4**, **12.1**, 0.6, 2.8, 0.0
Gadolinium Map	5.6, 2.9, 3.8, **5.2**, **17.6**, **3.0**, 1.0	1.5, 1.6, 3.9, **17.4**, **23.2**, **16.1**, 0.0

6.5.5 Effects of Projection Filtering (Four-Material Phantom)

The effects of filtering in the projection domain were explored with a Wiener filter of differing kernel sizes. The goal was to determine the effects of noise reduction in the projection domain via a common filter on material decomposition. It is expected that there is an optimal amount of filtering due to the kernel size where noise is sufficiently reduced while edges are maintained, and this study aimed to find it. In all cases, the projection data was generated based on simulations of the four-material model represented in Fig. 6.1 with 110 μm $\times$ 110 μm pixels. Poisson noise was added and then the noisy projections were filtered using differing kernel size Wiener filters. These kernel sizes were 1$\times$1 (no filter), 3$\times$3, 5$\times$5, 7$\times$7, 9$\times$9 and 11$\times$11. The filtered projections were then reconstructed using filtered back projection to a voxel size of 118.75 μm $\times$ 118.75 μm $\times$ 118.75 μm. Material decomposition was then calculated using the single and multi-step methods and the results (Fig. 6.13). The maximum decomposition errors increased with increasing kernel size. Therefore, filtering with a small kernel Wiener filter yielded the best results. This is because the Wiener filter introduces more rounding of edges as the kernel size increases and this rounding decreases accuracies. The much greater accuracy of the multi-step method led to greater CNRs than the single-step technique and the multi-step method outperformed the single-step method in terms of percent errors and CNRs.

6.5.6 Effects of Projection Pixel Binning (Four-Material Phantom)

The effects of binning the projection data from smaller to larger pixels before reconstruction versus acquiring data with larger pixels directly on material decomposition were investigated. This study attempts to understand if the noise in the projections can be

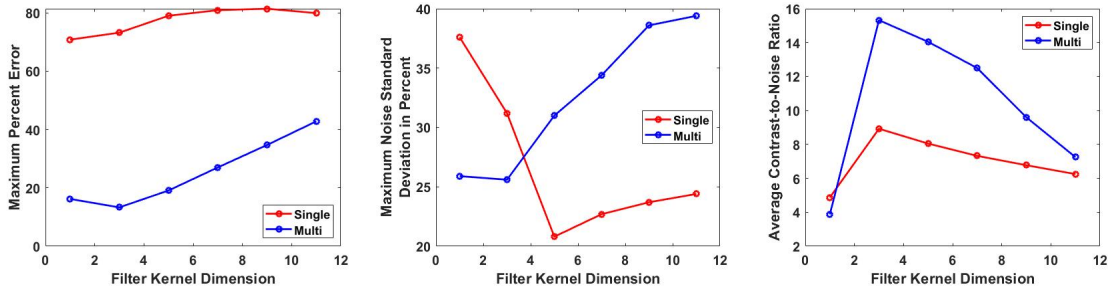

(a) (b) (c)

Figure 6.13: Filtering effects on material decomposition examined through single-step and multi-step. (a) Displays the maximum PEs, (b) displays the maximum NSDs and (c) displays the average CNRs.

improved by combining every four pixels (through averaging) thereby improving the pixel statistics over the baseline where no binning is performed. To test this, projection data was generated from four-material models based on Fig. 6.1 with five different pixel sizes of 55 μm $\times$ 55 μm, 110 μm $\times$ 110 μm, 220 μm $\times$ 220μm, 440 μm $\times$ 440 μm and 880 μm $\times$ 880 μm. The data with the four smallest pixels sizes was then binned in a 2$\times$2 fashion. The four binned datasets and the four larger pixel size datasets were then reconstructed to slightly larger voxels of 118.75 μm $\times$ 118.75 μm $\times$ 118.75 μm, 237.5 μm $\times$ 237.5 μm $\times$ 237.5 μm, 475 μm $\times$ 475 μm $\times$ 475 μm and 950 μm $\times$ 950 μm $\times$ 950 μm via filtered back projection. Single and multi-step material decomposition were then performed on both datasets. Images with equivalent effective voxels sizes were then compared (Fig. 6.14). In this figure, "Recon" denotes a larger pixel acquisition where as "Bin" denotes a smaller pixel acquisition with binning. The maximum errors increase as the effective voxel size increases. This is effectively a sampling problem as fewer voxels are used to represent a material region as voxel size increases leading to a higher fraction of the total voxels in the region capturing the transition between materials and resulting in lower accuracies. Acquiring data with larger pixels directly produces decomposition results with lower errors, but the errors are very similar for the two decomposition methods. Overall, single and multi-step decomposition show similar performance in terms of binning as displayed in the percent errors and CNRs.

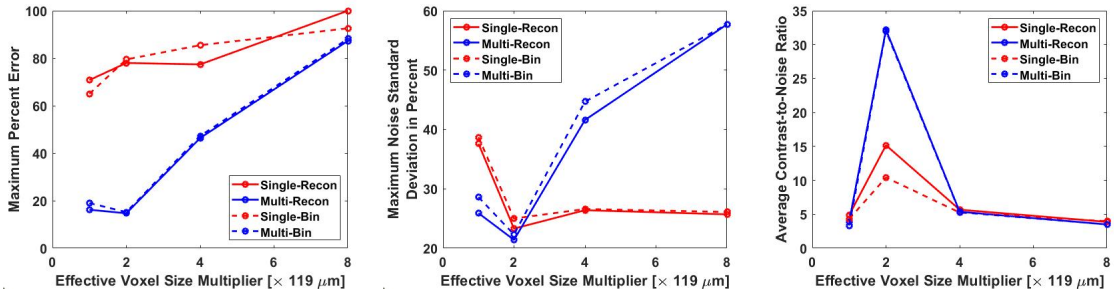

(a) (b) (c)

Figure 6.14: Binning effects on material decomposition examined through single-step and multi-step. (a) Displays the maximum PEs, (b) displays the maximum NSDs and (c) displays the average CNRs.

6.5.7 Effects of Signal Size (Four-Material Phantom)

Next, the effects of signal size on material decomposition were explored. It is expected that there is a spatial resolution limit for the modeled 110 μm $\times$ 110 μm pixel size detector for a 7.92 mGy measurement and it is desired to explore this limit with respect to material decomposition. Therefore, four-material models based on Fig. 6.1 were constructed with varying signal sizes of 0.5 mm, 1.0 mm, 2.0 mm, 3.0 mm, 4.0 mm, 5.0 mm and 6.0 mm. These models were used to generate projection data and then this data was reconstructed using filtered back projection. Material decomposition was performed using single and multi-step decomposition techniques. The decomposition results for the differing signal size problems can be seen in Fig. 6.15. As the signal size increases, the error decreases, and the standard deviation remains relatively constant. However, the error changes very little for signal sizes of 1.0 mm and above indicating that this may be the limiting size for this pixel size and dose combination. The reason for this trend can be explained again by sampling as signal size increases more voxels lie within the material region leading to a more accurate representation of the mean in the region. The CNRs decrease as signal size increases. This is probably due to the slight increase in noise in the signal and background regions as the signals become larger. Thresholding and flexibility in the choice of number and location of energy bins used in the multi-step method allow for CNRs greater than single-step. The multi-step method clearly out performs single-step as evidenced by the lower maximum

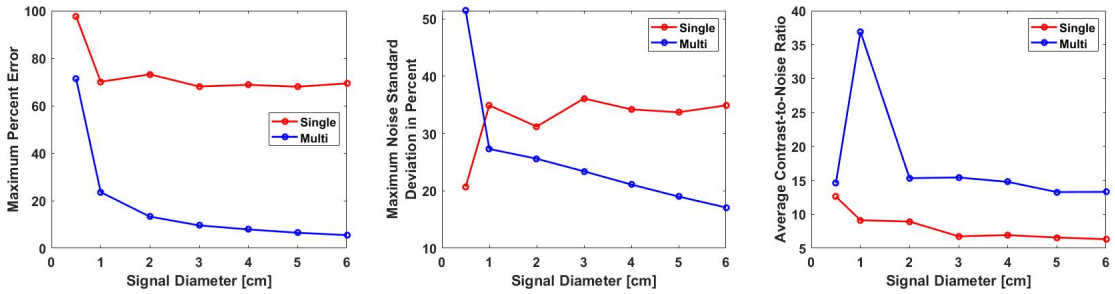

(a) (b) (c)

Figure 6.15: Signal size effects on material decomposition examined through single-step and multi-step. (a) Displays the maximum PEs, (b) displays the maximum NSDs and (c) displays the average CNRs.

errors and higher average CNRs for all signal sizes.

6.5.8 Effects of Energy Bin Overlap (Four-Material Phantom)

Finally, the effects of energy bin overlap or spacing on material decomposition were explored. As the bins become wider and overlap more, each bin becomes less unique from its neighbor and the system becomes more under-determined. As the bins become narrower with greater spacing, bins are more unique, but count statistics get worse. So, it was desired to discover this trade-off and find an optimal configuration. The energy-resolved data was generated with equal width bins with 1 keV spacing (-1 keV overlap) as [9,22], [23,36], [37,50], [51,64], [65,78], [79,92], [93,106] and [107,120] keV, respectively. Additional four-material models based on Fig. 6.1 were constructed with varying amounts of overlap of -9 keV, -5 keV, -1 keV, 1 keV, 5 keV, 9 keV, 13 keV, 17 keV, 21 keV, 25 keV and 29 keV. These projection datasets were then reconstructed using FBP and decomposition using both techniques was performed. Energy weighting based on the signal-to-noise ratio (SNR) of each region of the data was used in the multi-step decomposition and weighting based on the SNR of the water region was used for single-step decomposition. The decomposition results for the differing amounts of energy bin overlap were then summarized (Fig. 6.16). In these graphs, negative overlap indicates that the energy bins were separated by the given amount. Increasing the overlap decreases the decomposition errors until 17 keV for

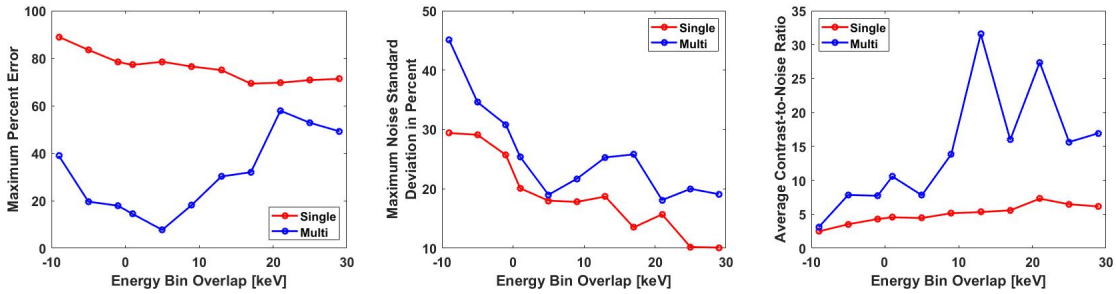

(a) (b) (c)

Figure 6.16: Energy bin overlap effects on material decomposition examined through single-step and multi-step. (a) Displays the maximum PEs, (b) displays the maximum NSDs and (c) displays the average CNRs.

single-step and 5 keV for multi-step. Therefore, it seems that some overlap can successfully improve photon statistics without creating too much data redundancy. The errors are much larger for single-step. The multi-step CNR exceeds the single-step CNRs. The multi-step method clearly out performs single-step as evidenced by the lower maximum errors and higher average CNRs for all amounts of energy bin overlap.

6.6 Discussion of Multi-Material Phantom Results from Synthetic Data

The proposed multi-step material decomposition method is demonstrated using simulated spectral CT images. We have shown decomposition of up to six materials with superior results in comparison to a conventional single step decomposition method. We have also shown the ability of the method to handle a four-material problem with mixed-materials and multiple concentrations. As shown here, performing the decomposition in multiple steps allows for flexibility in bin selection for each step where bins can be chosen to maximize quantitative accuracy for the material under focus in that step. Energy bins of the original data can be combined in several ways throughout the multi-step process to improve photon economy. Preferential bin weighting can also be performed to maximize contrast between the material being decomposed and the remaining materials in the mixture. Thresholding operations performed after each decomposition step serve to improve material separation and reduce noise. The quantitative maps have been obtained in terms of volume fractions

of each material in a given voxel. Formulating the problem in this manner allows for setting convenient bounds of zero and one for all variables in the bounded least squares solution. This technique also allows for the addition of a conservation of volume constraint that can be applied to certain problems to help stabilize the solution.

6.7 Chapter Summary

In this chapter, we begin by describing our novel contribution to the field of medical imaging of a multi-step method for material decomposition with guidance on how to choose energy bins, how to calculate bin weights and how to use thresholds for optimal utility of the new method. Next, the metrics we used to evaluate the performance of our decomposition techniques were summarized. This was followed by initial simulation studies with multi-material phantoms to explore the new method with problems of increasing complexity. Finally, the multi-step method was explored for various combinations of parameters to further display the superiority of the technique over an existing technique. In these studies, optimal filtering kernel dimension, effects of pixel binning, effects of phantom signal size and effects of energy bin overlap were examined using our four-material problem.

Chapter 7

Experimental Validation of the Multi-Step Method

Single-step and multi-step decomposition were performed using the method described in Chap. 5 for two multi-material phantoms. Three-dimensional rendering of multi-step decomposition results for the three, five-material phantoms can be seen in Fig. 7.1. In this figure, (a) corresponds to the data collected with the silicon detector in SPM-FPM, (b) corresponds to the data collected with the cadmium telluride WidePix detector in SPM-FPM and (c) corresponds to the data collected with the cadmium telluride WidePix detector in SPM-CM. The multi-step method was also able to decompose a biological specimen of a chicken heart with two contrast agents injected.

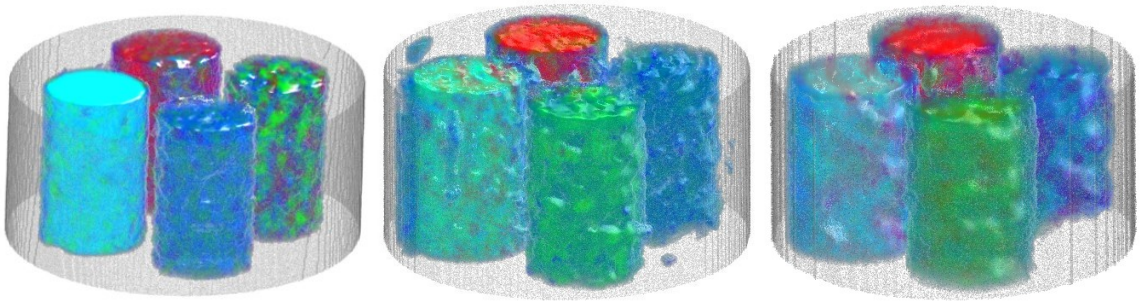

(a) (b) (c)

Figure 7.1: Three-dimensional renderings of three, five-material phantom decomposition results.

7.1 Five-Material Phantom Measured with Silicon Detector

This five-material phantom data was collected with the silicon detector in SPM-FPM because of the improved spatial resolution in FPM. We have also found that the spatial resolution of our Medipix3RX detectors is often better in SPM than in CSM [94]. In this experiment, the PCD data was collected with a Medipix detector with an effective pixel size of 55 μm with 256 $\times$ 256 pixels. The multi-energy 3D attenuation images were then reconstructed to 87 μm isotropic voxels with 200 $\times$ 200 $\times$ 200 voxels. A comparison between the attenuation curves for counts-over-threshold data for each of the material regions extracted from one slice versus the basis function generated from our analytical simulation tool used in material decomposition is shown in Fig. 7.2. All material maps from all multi-step decomposition steps for the five-material phantom data collected with the silicon detector operated in SPM-FPM are shown (Fig. 7.3). In this figure, (a) is the ABS plastic (under focus), (b) is the average of gadolinium and iodine mixtures (discarded) and (c) the average of the hydroxyapatite mixture and water (discarded) for step 1, respectively. (d) is the iodine mixture (under focus), (e) is the gadolinium mixture (discarded) and (f) is the average of the hydroxyapatite mixture and water (discarded) for step 2, respectively. (g) is the gadolinium mixture (under focus) and (h) is the average of the hydroxyapatite mixture and water (discarded) for step 3, respectively. (i) is the hydroxyapatite mixture (under focus) and (j) is water (discarded) for step 4. (k) is water (under focus) for step 5. The material maps under focus from each step have been combined into one color-coded image shown in Fig. 7.4(c). The improvement in the gadolinium decomposition from steps 2 to 3 and in the water decomposition from steps 4 to 5 is evident in Fig. 7.3. This is because optimal bins and bin weights have been chosen for gadolinium in step 3 and water in step 5 which is not the case for steps 2 and 4.

The ground truth and combined decomposition results for single-step and multi-step are displayed in Fig. 7.4 for the five-material phantom collected with the silicon detector. The quantitation of these decomposition results can be seen in Tab. 7.1 and 7.2. Table 7.1 displays the percent errors (PEs) in each ROI (ROI#1, ROI#2, ROI#3, ROI#4, ROI#5)

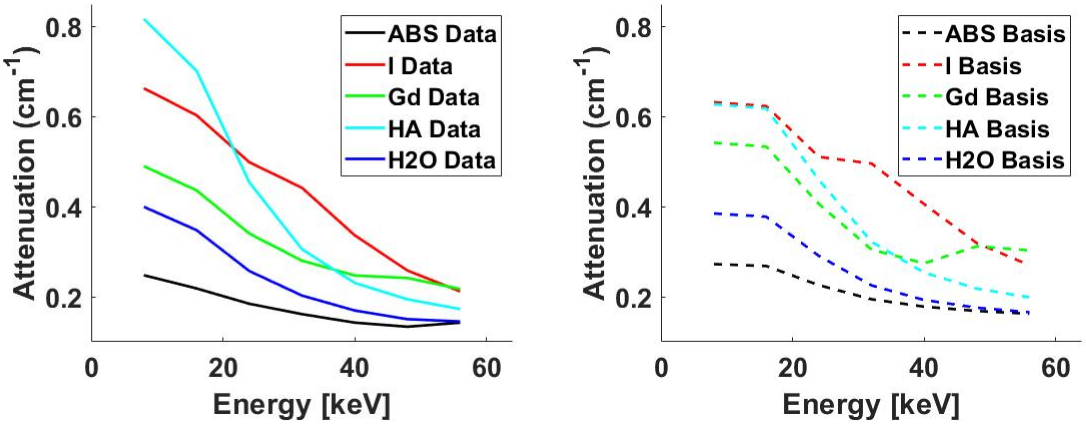

(a) (b)

Figure 7.2: (a) Attenuation curves extracted from the counts-over-threshold data and (b) the model basis functions used in decomposition for the five-material phantom data collected with the silicon detector in SPM-FPM.

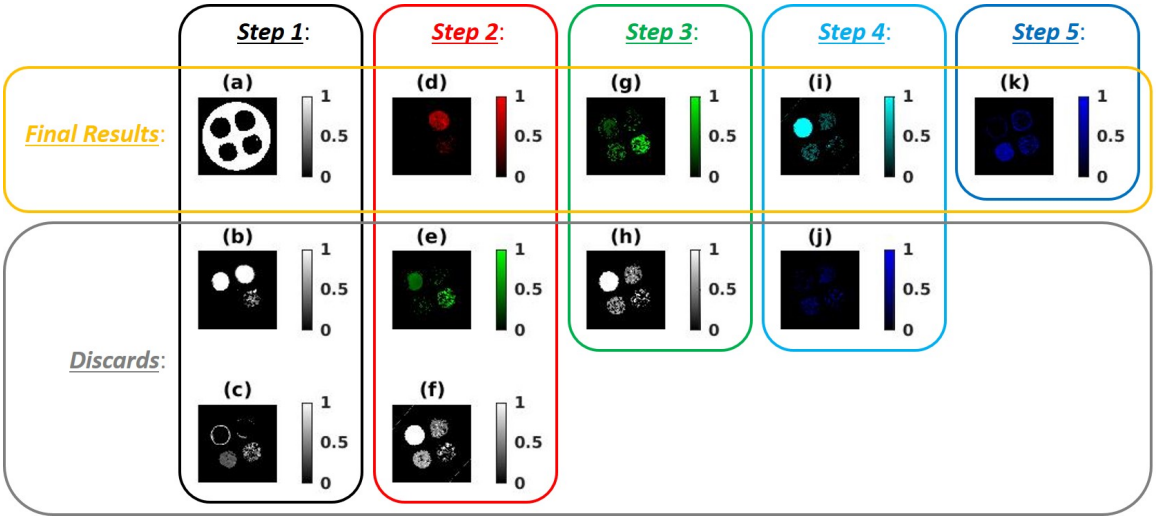

Figure 7.3: Material maps resulting from each step of multi-step material decomposition for the five-material phantom measured with the silicon detector in SPM-FPM.

for each material map generated using the single-step and multi-step material decomposition techniques for the ABS phantom data collected with the silicon detector in SPM-FPM. The bold values are of most interest as these represent the PEs in a material ROI in its respective map. Table 7.2 displays the contrast to noise ratios (CNRs) and noise standard deviations (NSDs) in percent in each ROI (ROI#1, ROI#2, ROI#3, ROI#4, ROI#5) for each material map generated using the single-step and multi-step material decomposition techniques for the ABS phantom data collected with the silicon detector in SPM-FPM. The bold values are of most interest as these represent the CNRs and NSDs in a material ROI in its respective map. Table 7.3 displays the accuracies in percent and corresponding confidence intervals in percent for a material ROI in its respective map generated using the single-step and multi-step material decomposition techniques for the ABS phantom data collected with the silicon detector in SPM-FPM. From the qualitative results, it can be seen that the hydroxyapatite region is mostly misidentified as iodine in single-step, whereas in multi-step hydroxyapatite is more accurately recovered. The quantitative results also show that the multi-step method outperforms single-step. This is evidenced by the worst-case error of 75.6% for single-step versus 46.8% for multi-step. In addition, CNRs improve from single-step to multi-step as the average CNR for single-step is 2.54 versus 4.52 for multi-step. Because of the large number of voxels in each material region, the 95% confidence intervals are rather tight with little overlap of the ranges between single-step and multi-step indicating that the performance benefit in multi-step is significant. Also, the weighted matrices of linear attenuation coefficients for the five-material problem do become better conditioned as the condition numbers are 1434733 for single-step versus 3388, 2203, 366, 2357 and 1 for the five consecutive steps of the multi-step method.

7.1.1 Determining Sufficient CT Arc Sampling

To study the effects of changes to our decomposition strategy and to justify our methods, several exploratory calculations were conducted. To determine sufficient sampling of the CT scan arc required for accurate material decomposition, we examine this multi-material

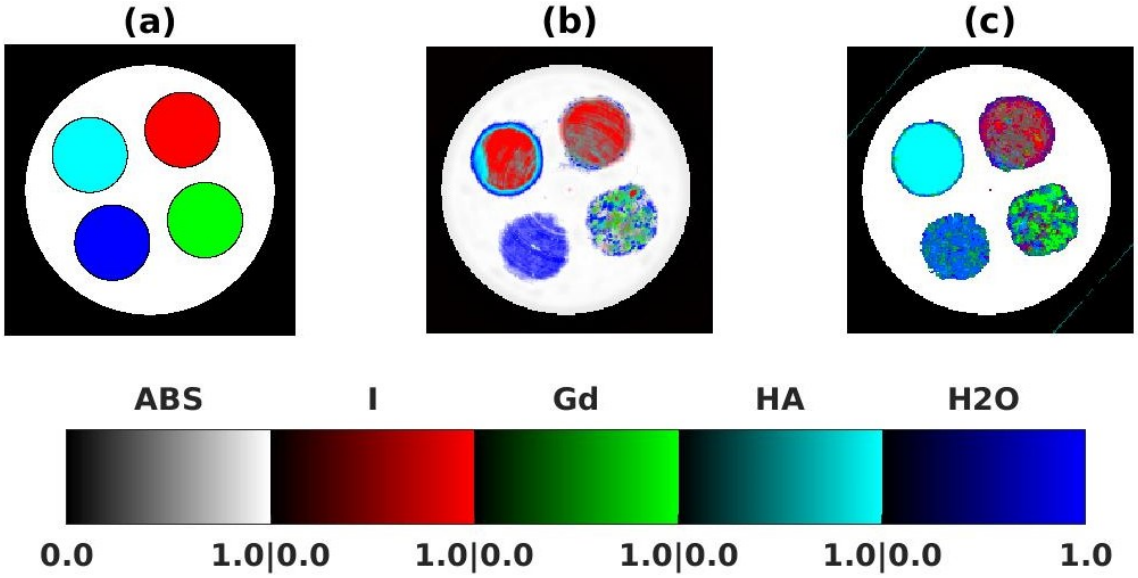

Figure 7.4: Color-coded (a) ground truth and combined material decomposition results for the (b) single-step and (c) multi-step techniques for the five-material phantom data collected with the silicon detector in SPM-FPM.

Table 7.1: PEs in each ROI (ROI#1, ROI#2, ROI#3, ROI#4, ROI#5) for single-step and multi-step for the ABS phantom measured with the silicon detector in SPM-FPM.

	Single-Step	Multi-Step
ABS Map	**2.0**, 1.0, 25.5, 0.0, 27.5	**0.8**, 0.0, 0.7, 0.0, 0.1
Iodine Map	0.1, **26.7**, 12.4, 72.4, 0.2	0.2, **42.4**, 8.3, 0.0, 0.1
Gadolinium Map	0.0, 1.0, **75.6**, 0.0, 0.4	0.1, 3.7, **46.8**, 15.0, 19.2
Hydroxyapatite Map	0.0, 23.6, 12.9, **72.7**, 0.3	0.0, 20.0, 6.2, **0.2**, 21.5
Water Map	0.4, 1.1, 24.8, 0.9, **28.4**	0.4, 10.1, 29.1, 0.0, **43.5**

Table 7.2: CNRs and NSDs in each ROI (ROI#1, ROI#2, ROI#3, ROI#4, ROI#5) for single-step and multi-step for the ABS phantom measured with the silicon detector in SPM-FPM.

	Single-Step		Multi-Step	
	CNR	NSD	CNR	NSD
ABS Map	**3.8**	**3.6**, 2.5, 19.0, 0.1, 12.2	**4.2**	**8.8**, 0.0, 8.5, 0.0, 3.6
Iodine Map	**3.0**	1.0, **16.8**, 13.3, 31.2, 0.7	**3.5**	2.6, **15.6**, 14.7, 0.0, 2.0
Gadolinium Map	**1.1**	0.4, 2.7, **21.6**, 0.0, 1.8	**1.4**	2.4, 11.7, **36.6**, 14.8, 24.2
Hydroxyapatite Map	**0.9**	0.3, 15.0, 14.1, **29.1**, 0.9	**10.6**	0.7, 16.0, 14.5, **2.8**, 19.2
Water Map	**3.9**	3.0, 2.7, 24.2, 3.7, **13.0**	**2.9**	5.1, 16.2, 26.8, 0.0, **12.8**

Table 7.3: ACIs in percent for a material ROI in its respective map for single-step and multi-step for the ABS phantom measured with the silicon detector in SPM-FPM.

	Ground Truth	Single-Step	Multi-Step
ABS Map	**100.00±0.00**	**97.98±0.07**	**99.23±0.17**
Iodine Map	**100.00±0.00**	**73.35±0.84**	**57.65±0.78**
Gadolinium Map	**100.00±0.00**	**24.36±1.09**	**53.25±1.85**
Hydroxyapatite Map	**100.00±0.00**	**27.28±1.46**	**99.81±0.14**
Water Map	**100.00±0.00**	**71.61±0.65**	**56.50±0.64**

phantom measured with the silicon detector where the scan was conducted over a complete 360° arc with 1° spacing between the projections. By selecting a subset of equally spaced projections from the original 360, we can see when decomposition accuracies start to significantly degrade. This is shown in Fig. 7.5 through four parameters of percent error (PE), contrast to noise ratio (CNR), noise standard deviation (NSD) and condition number. In this multi-material problem, there are five materials and five steps of the multi-step decomposition method yielding many PEs, CNRs and NSDs for each material region of each material map and five condition numbers corresponding to each step. Here we have reduced the data to the maximum PEs, minimum CNRs and maximum NSDs considering only a particular material region in its the respective material map and the maximum condition numbers of the five steps of the multi-step decomposition. These (a) maximum PEs, (b) minimum CNRs, (c) maximum NSDs and (d) maximum condition numbers have been plotted against the number of projections sampled from the original 360 for three reconstruction algorithms of the Feldkamp, Davis, Kress algorithm [28], the simultaneous iterative reconstruction technique (SIRT) and the conjugate gradient least squares (CGLS) algorithm. In all cases, reconstruction was conducted with 120 iterations of SIRT and 10 iterations of CGLS. These methods are implemented in the ASTRA toolbox [91]. This is the only place in this dissertation where SIRT and CGLS are used. Otherwise, FDK was the primary reconstruction algorithm used throughout this work. As the number of projections used for reconstruction and decomposition decreases, noise is expected to increase. The improvement gained from iterative reconstruction algorithms is more apparent when noise is higher, so different reconstruction algorithms were explored to see if their decomposition

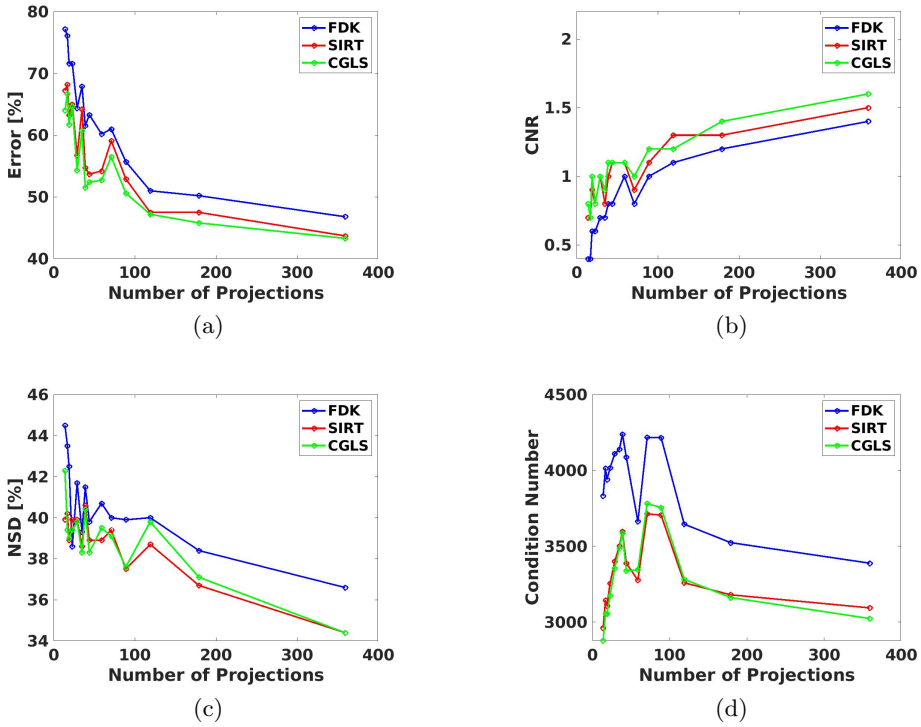

Figure 7.5: Maximum PEs, minimum CNRs, maximum NSDs and maximum condition numbers resulting from multi-step decomposition when CT scan arc sampling varies.

performances differed for different projection samplings. From Fig. 7.5 it can be noticed that all four parameters (PE, CNR, NSD and condition number) show little change for 120 to 360 projections. The SIRT and CGLS algorithms produce decompositions with lower errors, higher CNRs, lower NSDs and lower condition numbers than FDK as expected. From this we can conclude that acquiring CT projections with 3° spacing over a full 360° arc is about as sparse of sampling as one would want to obtain to maintain decent decomposition performance.

7.1.2 Comparing Decomposition with Binned Vs. Counts-Over-Threshold Mode Data

To investigate the benefits of working with data in counts-over-threshold mode versus data in binned mode, we compared the multi-material decomposition results using both approaches. As an example, we present a comparison of the data (in either mode) versus

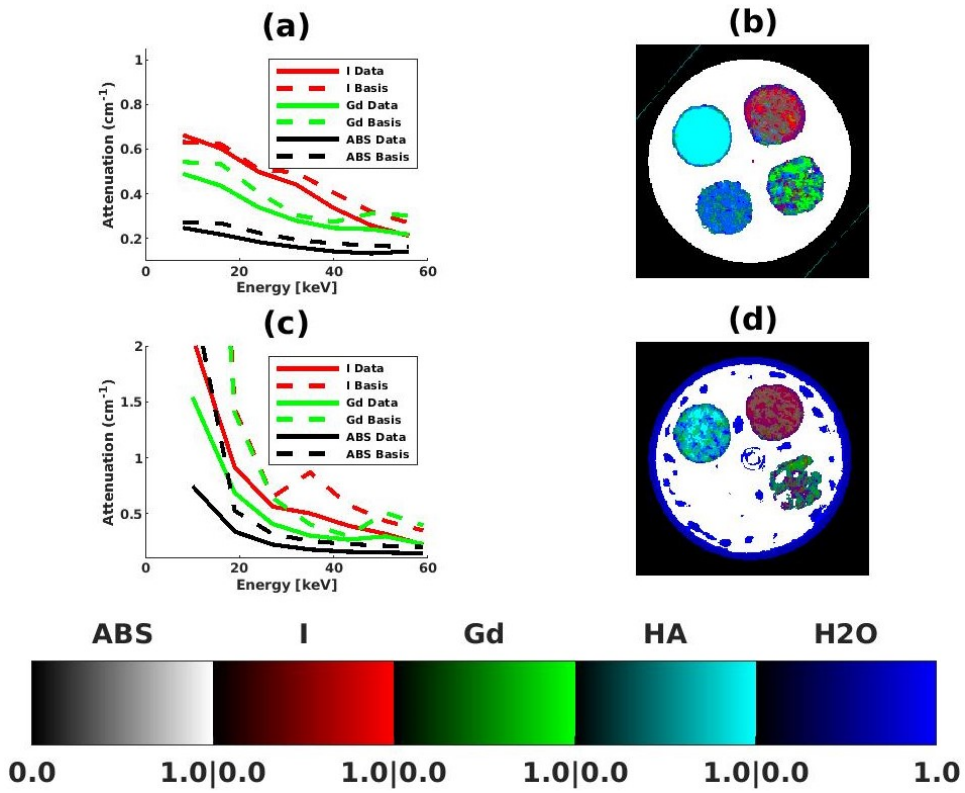

Figure 7.6: Comparison of data versus basis functions in counts-over-threshold and binned modes along with corresponding multi-step decomposition results.

the corresponding basis functions for a few select materials (I, Gd and ABS plastic) in Fig. 7.6(a) (counts over threshold) and Fig. 7.6(c) (binned). In this same figure, we also present the combined final multi-step decomposition results for either mode [Fig. 7.6(b) (counts over threshold) and Fig. 7.6(d) (binned)]. As can be seen in these attenuation curves, the match between the data and corresponding basis curve is better in counts-over-threshold mode. This leads to superior decomposition results as well as all materials are distinguished in counts-over-threshold mode and are not in binned mode. Specifically, in binned mode the multi-step algorithm fails to separate water and ABS plastic as the water region is almost completely misidentified as ABS plastic and specks of water are dispersed throughout the ABS background region due to the increased noise of this mode. The hydroxyapatite and gadolinium regions are also better identified in the counts-over-threshold mode case as gadolinium and water are present in the hydroxyapatite region of the binned mode cases and ABS plastic is present in the gadolinium region.

7.1.3 Determining the Benefits of Energy Bin Weighting

The effects of energy bin weighting can be seen in Fig. 7.7 which represent the multi-material phantom measured with the silicon detector. (a) and (f) represent the ABS plastic map, (b) and (g) represent the iodine map, (c) and (h) represent the gadolinium map, (d) and (i) represent the hydroxyapatite map and (e) and (j) represent the water map. Because we generated energy bins with nearly equal counts in our multi-material phantom simulations, the effects of this CNR weighting are not as prominent for those examples. Therefore, to better illustrate the benefits of this CNR weighting we present one of our experimental results where energy bins with unequal statistics have been measured. In Fig. 7.7, the ABS map [(a) versus (f)] and the water map [(e) versus (j)] are much better recovered when CNR weighting is applied versus when it is not. Specifically, a more uniform ABS background in seen in the case with CNR weighting and less voxels in this region are incorrectly decomposed as water as seen in the case without weighting. In addition, the phantom boundary shows up incorrectly as a ring in the gadolinium map of the case without weighting and not in the case with CNR weighting. The superiority of the case with weighting is also confirmed by the quantitative errors as the maximum error is reduced from 64.0% to 46.8% when the CNR weighting is applied. Because of the increased accuracies due to the CNR weighting, the average CNR of the resulting material maps also increase from 3.02 to 4.52 when the CNR weighting is applied.

7.1.4 Determining the Benefits of Selective Application of the Conservation of Volume Constraint

The conservation of volume constraint can serve as an additional equation during the material decomposition process. In a multi-step decomposition, selective application of this constraint during decomposition steps focusing on low contrast materials and not during steps focusing on high contrast materials has proven to be a reliable strategy. The best results for each material map represented as the top row are found through this selective process (Fig. 7.8). In Fig. 7.8, (a), (f) and (k) represent the ABS plastic map from step

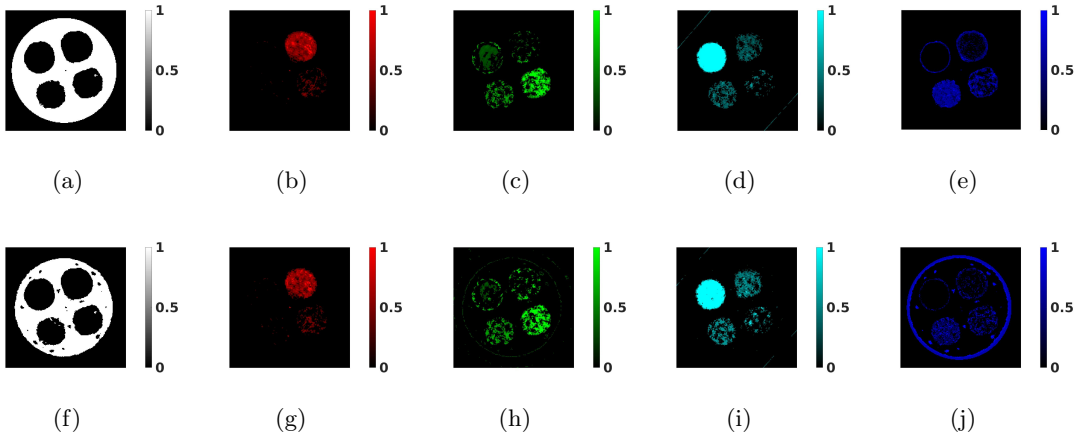

Figure 7.7: (a), (b), (c), (d) and (e) represent the multi-step decomposition results with CNR energy bin weighting. (f), (g), (h), (i) and (j) represent the multi-step decomposition results without energy bin weighting.

one, (b), (g) and (l) represent the iodine map from step 2, (c), (h) and (m) represent the gadolinium map from step 3, (d), (i) and (n) represent the hydroxyapatite map from step 4 and (e), (j) and (o) represent the water map from step 5. (a), (b), (c), (d) and (e) represent the case with selective application of the constraint, (f), (g), (h), (i) and (j) represent the case where the constraint is applied to all steps and (k), (l), (m), (n) and (o) represent the case where the constraint is not applied to any steps. The constraint serves to force the sum of all volume fractions within a voxel to sum to one. This often has the effect of elevating the calculated volume fraction of the focus material. This is helpful when decomposing low contrast materials because they have low attenuations which yield small volume fractions after decomposition. This can be observed in (k) for the case without the constraint where the very little ABS plastic is identified in the background region. This region is instead decomposed as a mixture of iodine, gadolinium and water. For high contrast materials with high attenuations, the constraint is unnecessary an often leads to other material regions being misidentified as the high contrast material. This can be seen in (g) as the hydroxyapatite region is misidentified as iodine. If the constraint is applied during the last step, any remaining void is filled with the last material to complete the voxel. This can be seen in (e) and (j) as water fills any remaining voids in the domain.

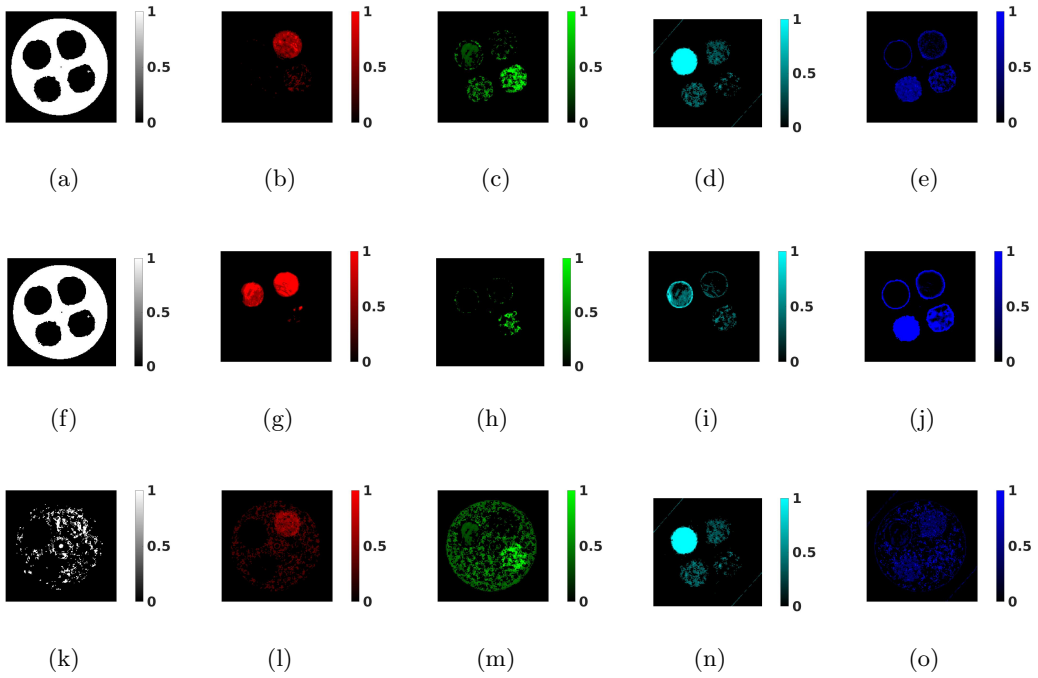

Figure 7.8: The top row is the results with selective application of the constraint, the middle row is the results where the constraint is always applied and the bottom row are the results where the constraint is never applied.

7.2 Five-Material Phantom Measured with Cadmium Telluride WidePix Detector in SPM-FPM

This five-material phantom data was gathered with the cadmium telluride WidePix detector in SPM-FPM because of the improved spatial resolution in FPM. We have also found that the spatial resolution of our Medipix3RX detectors is often better in SPM than in CSM [94]. In this experiment, the PCD data was collected with a Medipix detector with an effective pixel size of 55 μm with 256 $\times$ 256 pixels. The multi-energy 3D attenuation images were then reconstructed to 80 μm isotropic voxels with 200 $\times$ 200 $\times$ 200 voxels. A comparison between the attenuation curves for counts-over-threshold data for each of the material regions extracted from one slice versus the basis function generated from our analytical simulation tool used in material decomposition is shown in Fig. 7.9. All material maps from all multi-step decomposition steps for the five-material phantom data collected with the cadmium telluride WidePix detector operated in SPM-FPM are shown in Fig.

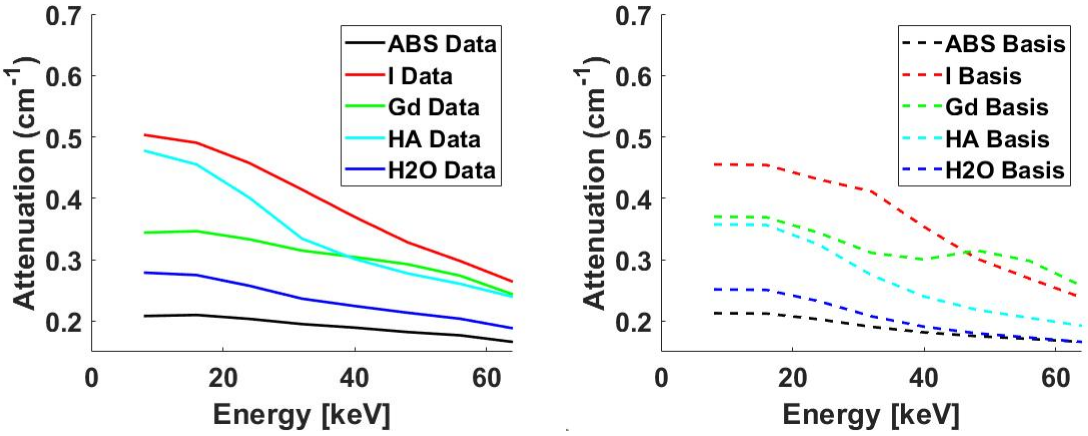

(a) (b)

Figure 7.9: (a) Attenuation curves extracted from the counts-over-threshold data and (b) the model basis functions used in decomposition for the five-material phantom data collected with the cadmium telluride WidePix detector in SPM-FPM.

7.10. In this figure, (a) is the ABS plastic (under focus), (b) is the average of gadolinium and iodine mixtures (discarded) and (c) the average of the hydroxyapatite mixture and water (discarded) for step 1, respectively. (d) is the iodine mixture (under focus), (e) is the gadolinium mixture (discarded) and (f) is the average of the hydroxyapatite mixture and water (discarded) for step 2, respectively. (g) is the gadolinium mixture (under focus) and (h) is the average of the hydroxyapatite mixture and water (discarded) for step 3, respectively. (i) is the hydroxyapatite mixture (under focus) and (j) is water (discarded) for step 4. (k) is water (under focus) for step 5. The material maps under focus from each step have been combined into one color-coded image shown in Fig. 7.11(c). The improvement in the gadolinium decomposition from steps 2 to 3 and in the water decomposition from steps 4 to 5 is evident in Fig. 7.10. This is because optimal bins and bin weights have been chosen for gadolinium in step 3 and water in step 5 which is not the case for steps 2 and 4.

The ground truth and combined decomposition results for single-step and multi-step are displayed in Fig. 7.11 for the five-material phantom data collected with the cadmium telluride WidePix detector operated in SPM-FPM. The quantitation of these decomposition results can be seen in Tab. 7.4 and 7.5. Table 7.4 displays the percent errors (PEs) in each ROI (ROI#1, ROI#2, ROI#3, ROI#4, ROI#5) for each material map generated using the

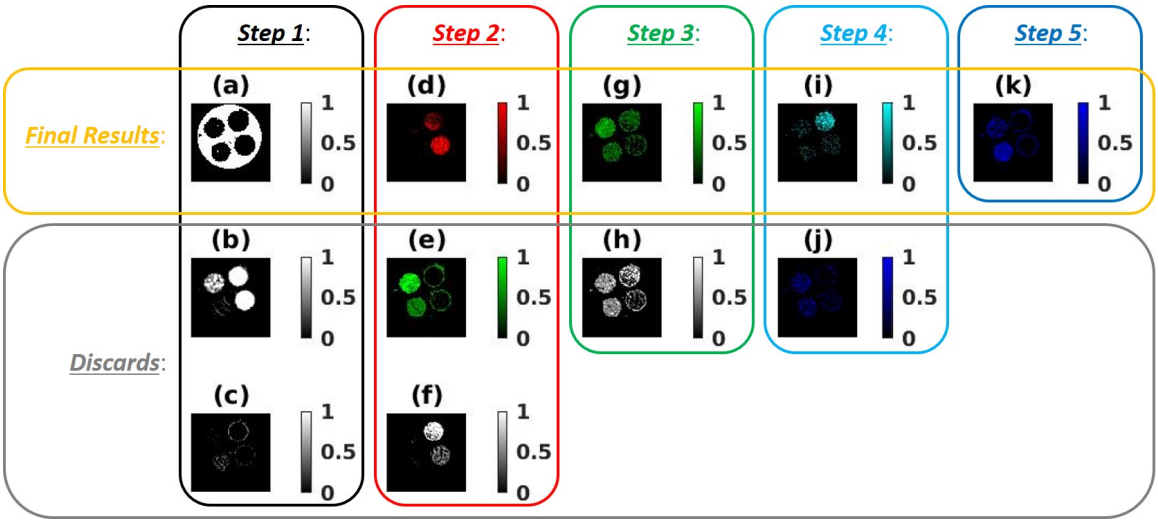

Figure 7.10: Material maps resulting from each step of multi-step material decomposition for the five-material phantom measured with the cadmium telluride WidePix detector in SPM-FPM.

single-step and multi-step material decomposition techniques for the ABS phantom data collected with the cadmium telluride WidePix detector in SPM-FPM. The bold values are of most interest as these represent the PEs in a material ROI in its respective map. Table 7.5 displays the contrast to noise ratios (CNRs) and noise standard deviations (NSDs) in percent in each ROI (ROI#1, ROI#2, ROI#3, ROI#4, ROI#5) for each material map generated using the single-step and multi-step material decomposition techniques for the ABS phantom data collected with the cadmium telluride WidePix detector in SPM-FPM. The bold values are of most interest as these represent the CNRs and NSDs in a material ROI in its respective map. Table 7.6 displays the accuracies in percent and corresponding confidence intervals in percent for a material ROI in its respective map generated using the single-step and multi-step material decomposition techniques for the ABS phantom data collected with the cadmium telluride WidePix detector in SPM-FPM. From the qualitative results, it can be noticed that the hydroxyapatite and gadolinium regions are misidentified as iodine in single-step, whereas in multi-step hydroxyapatite and gadolinium are more accurately recovered. In addition, much of the water region is misidentified as ABS plastic in single-step, but is more accurately recovered in multi-step. The quantitative results also display that the multi-step method outperforms single-step. This is evidenced by the

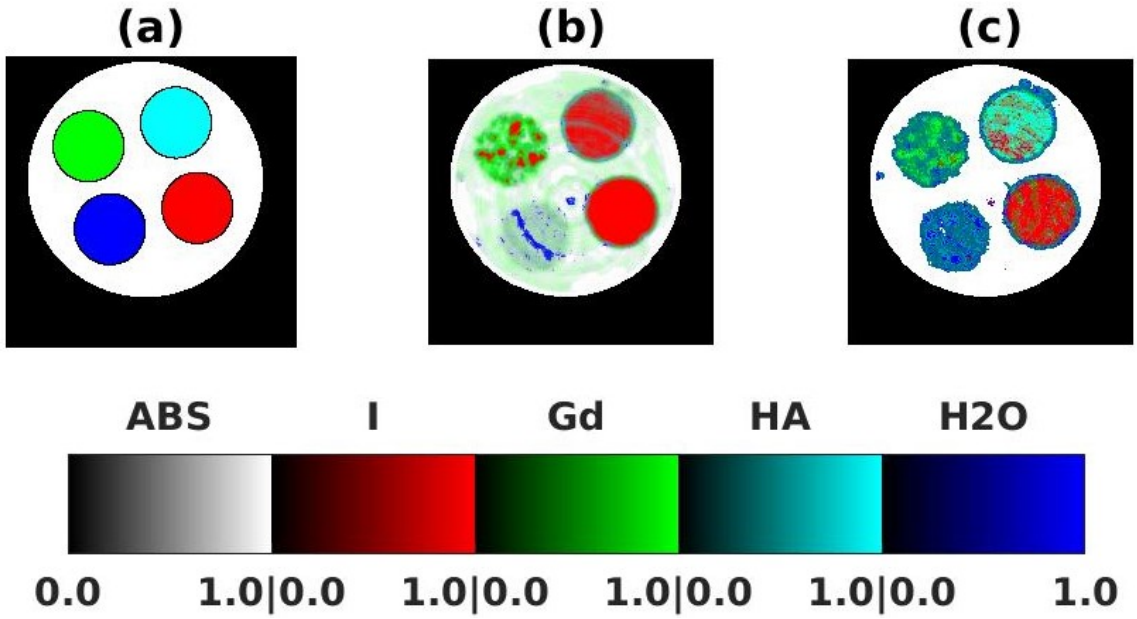

Figure 7.11: Color-coded (a) ground truth and combined material decomposition results for the (b) single-step and (c) multi-step techniques for the five-material phantom data collected with the WidePix detector in SPM-FPM.

Table 7.4: PEs in each ROI (ROI#1, ROI#2, ROI#3, ROI#4, ROI#5) for single-step and multi-step for the ABS phantom measured with the WidePix detector in SPM-FPM.

	Single-Step	Multi-Step
ABS Map	**12.4**, 0.1, 15.6, 1.5, 48.7	**1.6**, 0.0, 0.1, 0.0, 0.7
Iodine Map	1.3, **0.6**, 21.1, 79.2, 7.9	0.0, **19.8**, 1.7, 32.0, 0.4
Gadolinium Map	7.9, 0.9, **43.9**, 2.7, 16.5	0.5, 7.8, **44.1**, 26.2, 33.0
Hydroxyapatite Map	1.2, 0.1, 2.9, **85.0**, 8.2	0.1, 7.1, 7.5, **44.6**, 6.7
Water Map	1.7, 0.1, 4.3, 1.6, **81.3**	1.0, 1.9, 31.7, 1.1, **41.1**

worst-case error of 85.0% for single-step versus 44.6% for multi-step. In addition, CNRs improve from single-step to multi-step as the average CNR for single-step is 2.42 versus 3.00 for multi-step. Because of the large number of voxels in each material region, the 95% confidence intervals are rather tight with little overlap of the ranges between single-step and multi-step indicating that the performance benefit in multi-step is significant. Also, the weighted matrices of linear attenuation coefficients for the five-material problem do become better conditioned as the condition numbers are 9924313 for single-step versus 15051, 2922, 682, 1134 and 1 for the five consecutive steps of the multi-step method.

Table 7.5: CNRs and NSDs in each ROI (ROI#1, ROI#2, ROI#3, ROI#4, ROI#5) for single-step and multi-step for the ABS phantom measured with the WidePix detector in SPM-FPM.

	Single-Step		Multi-Step	
	CNR	NSD	CNR	NSD
ABS Map	**3.0**	**10.1**, 0.8, 17.0, 1.3, 15.9	**3.7**	**12.6**, 0.0, 2.6, 0.0, 8.1
Iodine Map	**5.1**	1.3, **4.5**, 29.3, 12.1, 2.5	**3.7**	1.6, **19.4**, 7.1, 24.2, 3.3
Gadolinium Map	**2.1**	7.9, 2.0, **22.9**, 3.7, 8.2	**3.0**	4.5, 13.3, **12.5**, 15.9, 13.7
Hydroxyapatite Map	**1.1**	1.5, 1.4, 2.8, **12.9**, 2.4	**2.0**	1.5, 12.7, 12.7, **26.9**, 12.1
Water Map	**0.8**	4.7, 0.9, 4.1, 1.4, **22.5**	**2.6**	7.8, 7.2, 22.2, 6.0, **16.3**

Table 7.6: ACIs in percent for a material ROI in its respective map for single-step and multi-step for the ABS phantom measured with the WidePix detector in SPM-FPM.

	Ground Truth	Single-Step	Multi-Step
ABS Map	**100.00±0.00**	**87.56±0.19**	**98.38±0.24**
Iodine Map	**100.00±0.00**	**99.41±0.23**	**80.22±0.98**
Gadolinium Map	**100.00±0.00**	**56.08±1.15**	**55.86±0.63**
Hydroxyapatite Map	**100.00±0.00**	**15.00±0.65**	**55.39±1.35**
Water Map	**100.00±0.00**	**18.70±1.13**	**58.87±0.82**

7.2.1 Examining the Benefits of Spectral Correction

The effects of spectral correction were investigated to determine if it was truly necessary using this multi-material phantom data collected with the cadmium telluride WidePix detector. These results can be seen in Fig. 7.12 and are dramatic. In this figure, (a) and (c) show the comparison between the data and basis functions for a few select materials (I, Gd and ABS plastic) when spectral correction is applied and when it is not, respectively. (b) and (d) show the corresponding combined multi-step decomposition results again when spectral correction is applied versus when it is not, respectively. From Fig. 7.12(a) and (c) it can be noticed that a stronger agreement between the data and basis curves is achieved after spectral correction, especially for higher energies. Without spectral correction, the basis functions tend to overestimate the data and this leads to poorer decomposition results. The spectral correction elevates the attenuation of the data such that data and basis curves are in better agreement. This better agreement between the data and basis functions after spectral correction leads to better decompositions as the water of the phantom is more correctly identified with spectral correction versus without. The water and gadolinium regions

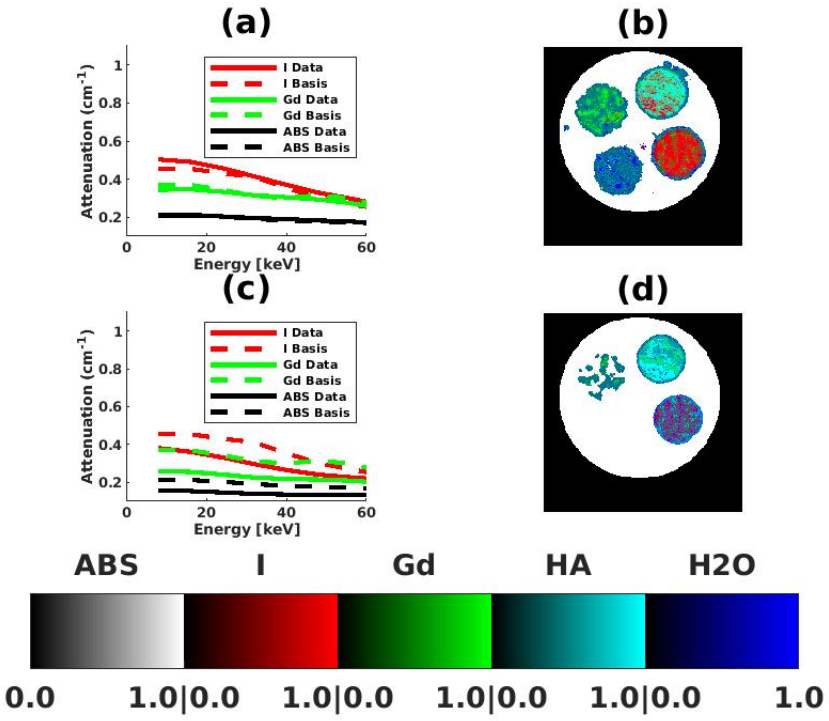

Figure 7.12: Comparison of data with and without spectral correction versus basis functions along with corresponding multi-step decomposition results.

of the case without spectral correction are nearly completely misidentified as ABS plastic. The iodine is also much better resolved with spectral correction versus without as the iodine region is misidentified as a mixture of iodine, hydroxyapatite and water in the case without spectral correction.

7.3 Five-Material Phantom Measured with Cadmium Telluride WidePix Detector in SPM-CM

This five-material phantom data was gathered with the cadmium telluride WidePix detector in SPM-CM because of the ability to acquire eight energy bins simultaneously in CM. We have also found that the spatial resolution of our Medipix3RX detectors is often better in SPM than in CSM [94]. In this experiment, the PCD data was collected with a Medipix detector with an effective pixel size of 110 μm with 128 $\times$ 128 pixels. The multi-energy 3D attenuation images were then reconstructed to 159 μm isotropic voxels

with 100 × 100 × 100 voxels. A comparison between the attenuation curves for counts-over-threshold data for each of the material regions extracted from one slice versus the basis function generated from our analytical simulation tool used in material decomposition is shown in Fig. 7.13. All material maps from all multi-step decomposition steps for the five-material phantom data collected with the cadmium telluride WidePix detector operated in SPM-CM are shown in Fig. 7.14. In this figure, (a) is the ABS plastic (under focus), (b) is the average of gadolinium and iodine mixtures (discarded) and (c) the average of the hydroxyapatite mixture and water (discarded) for step 1, respectively. (d) is the iodine mixture (under focus), (e) is the gadolinium mixture (discarded) and (f) is the average of the hydroxyapatite mixture and water (discarded) for step 2, respectively. (g) is the gadolinium mixture (under focus) and (h) is the average of the hydroxyapatite mixture and water (discarded) for step 3, respectively. (i) is the hydroxyapatite mixture (under focus) and (j) is water (discarded) for step 4. (k) is water (under focus) for step 5. The material maps under focus from each step have been combined into one color-coded image shown in Fig. 7.15(c). The improvement in the gadolinium decomposition from steps 2 to 3 and in the water decomposition from steps 4 to 5 is evident in Fig. 7.14. This is because optimal bins and bin weights have been chosen for gadolinium in step 3 and water in step 5 which is not the case for steps 2 and 4.

The ground truth and combined decomposition results for single-step and multi-step are displayed in Fig. 7.15 for the five-material phantom data collected with the cadmium telluride WidePix detector operated in SPM-CM. The quantitation of these decomposition results can be seen in Tab. 7.7 and 7.8. Table 7.7 displays the percent errors (PEs) in each ROI (ROI#1, ROI#2, ROI#3, ROI#4, ROI#5) for each material map generated using the single-step and multi-step material decomposition techniques for the ABS phantom data collected with the cadmium telluride WidePix detector in SPM-CM. The bold values are of most interest as these represent the PEs in a material ROI in its respective map. Table 7.8 displays the contrast to noise ratios (CNRs) and noise standard deviations (NSDs) in percent in each ROI (ROI#1, ROI#2, ROI#3, ROI#4, ROI#5) for each material map

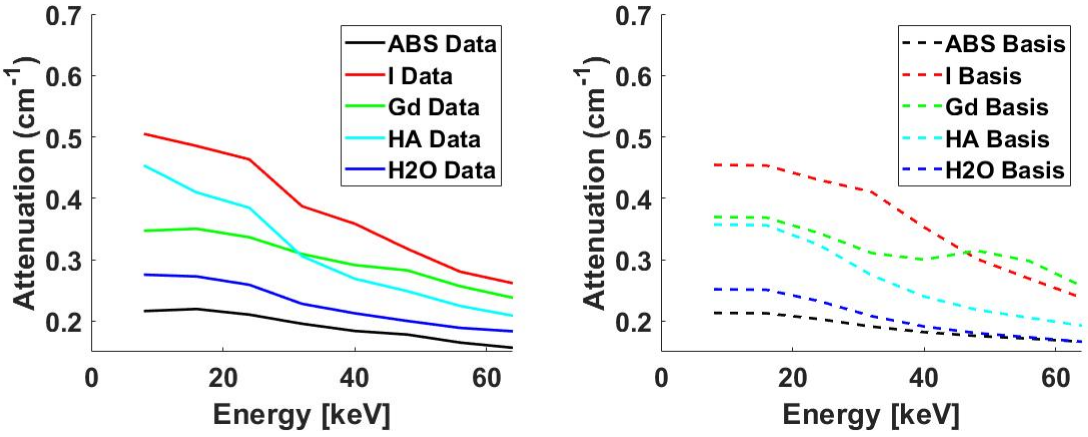

(a) (b)

Figure 7.13: (a) Attenuation curves extracted from the counts-over-threshold data and (b) the model basis functions used in decomposition for the five-material phantom data collected with the WidePix detector in SPM-CM.

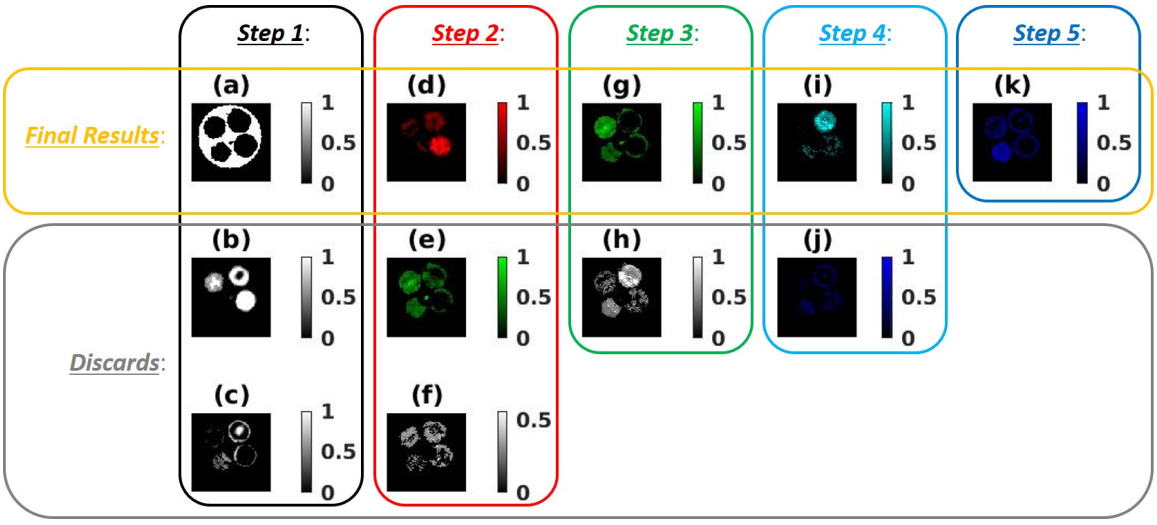

Figure 7.14: Material maps resulting from each step of multi-step material decomposition for the five-material phantom measured with the cadmium telluride WidePix detector in SPM-CM.

Table 7.7: PEs in each ROI (ROI#1, ROI#2, ROI#3, ROI#4, ROI#5) for single-step and multi-step for the ABS phantom measured with the WidePix detector in SPM-CM.

	Single-Step	Multi-Step
ABS Map	**15.4**, 0.2, 11.0, 0.7, 34.2	**9.8**, 0.0, 0.0, 0.0, 0.0
Iodine Map	2.2, **1.7**, 17.4, 51.8, 7.5	0.4, **14.8**, 15.0, 35.8, 4.3
Gadolinium Map	3.8, 1.0, **43.1**, 0.5, 7.4	4.0, 0.1, **42.0**, 0.6, 28.0
Hydroxyapatite Map	2.3, 0.9, 6.5, **57.6**, 10.4	0.3, 11.1, 0.4, **32.1**, 9.4
Water Map	6.8, 0.2, 8.2, 4.6, **59.5**	5.0, 2.1, 19.7, 2.8, **42.3**

generated using the single-step and multi-step material decomposition techniques for the ABS phantom data collected with the cadmium telluride WidePix detector in SPM-CM. The bold values are of most interest as these represent the CNRs and NSDs in a material ROI in its respective map. Table 7.9 displays the accuracies in percent and corresponding confidence intervals in percent for a material ROI in its respective map generated using the single-step and multi-step material decomposition techniques for the ABS phantom data collected with the cadmium telluride WidePix detector in SPM-CM. From the qualitative results, it can be observed that the hydroxyapatite region is mostly misidentified as iodine in single-step, whereas in multi-step hydroxyapatite is more accurately recovered. In addition, much of the water region is misidentified as ABS plastic in single-step, but is more accurately recovered in multi-step. The quantitative results also show that the multi-step method outperforms single-step. This is evidenced by the worst-case error of 59.5% for single-step versus 42.3% for multi-step. The CNRs remain rather similar from single-step to multi-step as the average CNR for single-step is 3.30 versus 3.26 for multi-step. Because of the large number of voxels in each material region, the 95% confidence intervals are rather tight with little overlap of the ranges between single-step and multi-step indicating that the performance benefit in multi-step is significant. Also, the weighted matrices of linear attenuation coefficients for the five-material problem do become better conditioned as the condition numbers are 10392192 for single-step versus 15321, 5934, 435, 1082 and 1 for the five consecutive steps of the multi-step method.

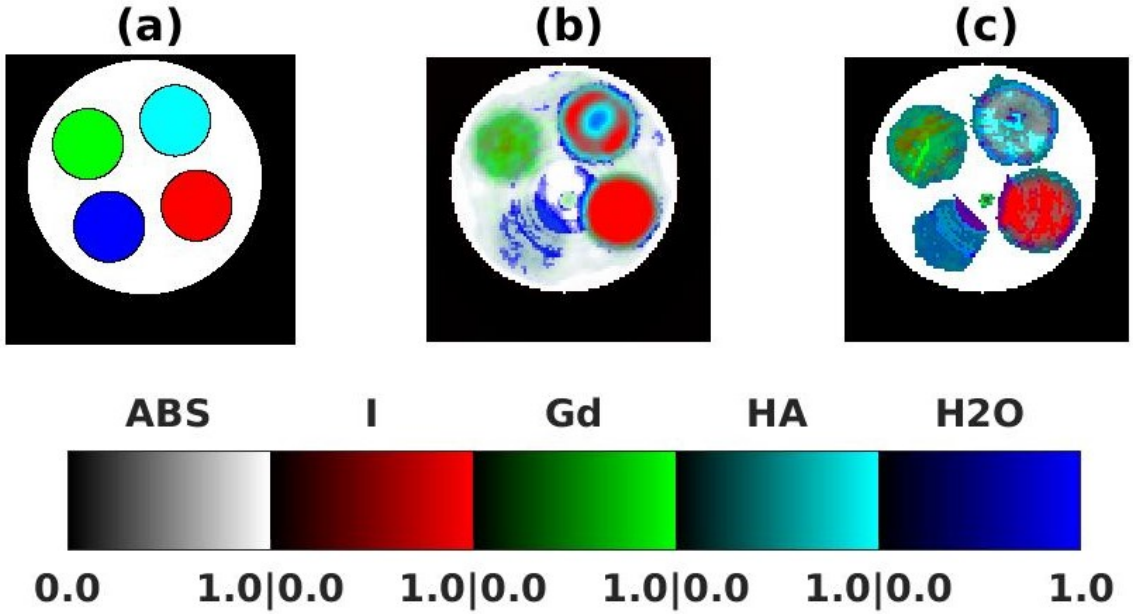

Figure 7.15: Color-coded (a) ground truth and combined material decomposition results for the (b) single-step and (c) multi-step techniques for the five-material phantom data collected with the WidePix detector in SPM-CM.

Table 7.8: CNRs and NSDs in each ROI (ROI#1, ROI#2, ROI#3, ROI#4, ROI#5) for single-step and multi-step for the ABS phantom measured with the WidePix detector in SPM-CM.

	Single-Step		Multi-Step	
	CNR	NSD	CNR	NSD
ABS Map	**3.0**	**18.6**, 0.6, 8.4, 0.8, 23.1	**2.7**	**29.7**, 0.0, 0.0, 0.0, 0.0
Iodine Map	**6.5**	2.5, **6.1**, 8.3, 32.6, 2.4	**4.3**	3.6, **16.5**, 16.6, 13.6, 12.0
Gadolinium Map	**4.3**	5.4, 2.6, **11.9**, 0.6, 3.6	**3.2**	13.3, 1.3, **13.0**, 4.3, 14.9
Hydroxyapatite Map	**1.5**	2.9, 4.3, 3.5, **27.1**, 3.1	**3.0**	3.6, 14.3, 3.3, **21.7**, 15.4
Water Map	**1.2**	15.0, 0.6, 4.5, 11.8, **28.6**	**3.1**	15.6, 7.5, 19.3, 11.0, **9.3**

Table 7.9: ACIs in percent for a material ROI in its respective map for single-step and multi-step for the ABS phantom measured with the WidePix detector in SPM-CM.

	Ground Truth	Single-Step	Multi-Step
ABS Map	**100.00±0.00**	**84.62±0.72**	**90.24±1.15**
Iodine Map	**100.00±0.00**	**98.34±0.62**	**85.25±1.67**
Gadolinium Map	**100.00±0.00**	**56.87±1.19**	**58.03±1.31**
Hydroxyapatite Map	**100.00±0.00**	**42.42±2.74**	**67.86±2.19**
Water Map	**100.00±0.00**	**40.54±2.89**	**57.72±0.94**

7.4 Chicken Heart with Injected Contrast Agents

Finally, the multi-step method was applied to the decomposition of a biological sample of a chicken heart with injected contrast agents (Fig. 7.16). The multi-energy chicken heart data was collected in CSM-FPM because of the improved spectral resolution in CSM and the improve spatial resolution in FPM. In this figure, (a) displays a front view of the chicken heart with muscle, tantalum and gadolinium regions identified. (b) is a 3D rendering of the decomposed chicken heart viewed from the front or positive z-direction based on the coordinate system shown in (a). The decomposition results have been color-coded with heart muscle tissue displayed in red, tantalum displayed in blue and gadolinium displayed in green. (c) is a front view cross section through the heart where both tantalum and gadolinium are present inside the heart chambers. (d) is a side view cross section [viewed from the positive x-direction based on the coordinate system in (a)] of the chicken heart which again shows the distribution of contrast agents within the chambers of the heart. In (b)-(d), the plastic case enclosing the chicken heart has been digitally removed from view leaving only the chicken heart and contrast agents. Several views can be seen in Fig. 7.16, but the distribution of both contrast agents is apparent in the front and side view cross sections. The Ta is mainly constrained to the top of the phantom where the left atrium and ascending aorta are located and the Gd is mainly contained in the bottom of the phantom where the left ventricle is located.

7.5 Discussion of Multi-Material Phantom Results from Experiments

Since we have measured similar phantoms across two different detectors and two different acquisition modes while maintaining otherwise similar experimental conditions, we can make some observations. First, after plotting the attenuation curves from regions corresponding to each material selected from one reconstructed slice (Fig. 7.2, 7.9 and 7.13), we can notice that the K-edge of iodine is much more identifiable in the silicon data. This identifying feature aids in the decomposition of iodine as less gadolinium is misidentified as iodine in

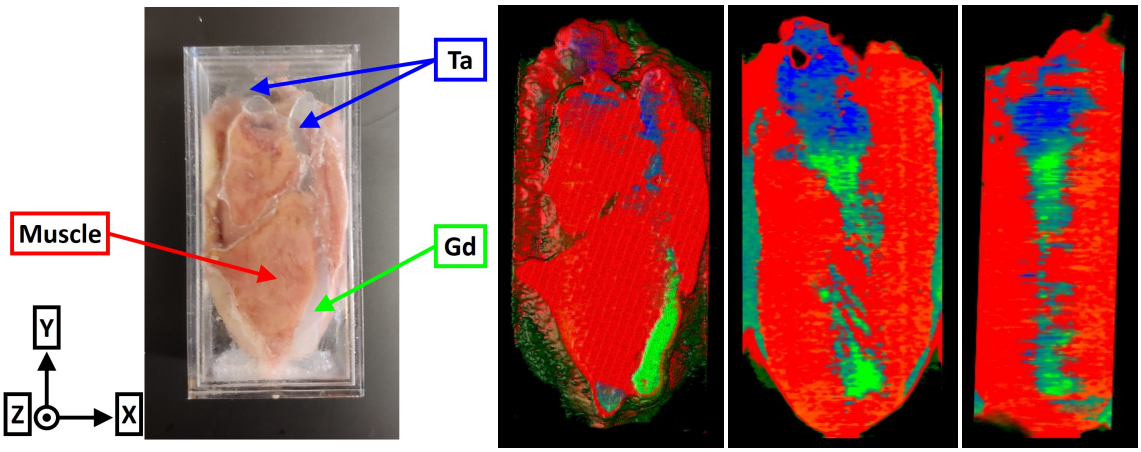

Figure 7.16: Multi-step material decomposition results for a chicken heart injected with two contrast agents of tantalum (Ta) and gadolinium (Gd).

the silicon data in comparison to the cadmium telluride WidePix data. The ability of the silicon detector to better resolve the K-edge of iodine is likely due to its lower atomic number than cadmium or tellurium. Due to its lower atomic number, silicon does not possess a K-absorption edge near the K-edge of iodine, whereas cadmium and tellurium do have K-edges in the energy range of the iodine edge. In the case of the cadmium telluride detector, this effectively decreases the number of photons or increases the attenuation below the iodine K-edge and smooths the iodine K-edge. In addition, the superior spatial and energy resolutions of the silicon detector (as described in Sec. 3.4 and Sec. 3.6, respectively) as compared with the WidePix detector also tend to improve the decomposition performance of the silicon data. As for spatial resolution, the more uniform response of the silicon detector across all pixels leads to reconstructions with less ring artifacts. And the superior energy resolution of the silicon detector probably produced energy bins with much sharper edges and less overlapping spectral information. This leads to more unique energy measurements and less dependencies between the equations of the linear system of equations in material decomposition. However, a competing effect involves the absorption efficiencies of the two sensor materials. Cadmium telluride has a much higher absorption efficiency than silicon and this results in improved pixel statistics for the same acquisition time measurements.

But overall, the performance of the two detectors seems rather similar with the cadmium telluride WidePix detector performing slightly better.

From some of our exploratory calculations, we have determined the maximum spacing between CT projections to maintain a low error decomposition using our multi-step method. This spacing was 3° over a full 360° arc. We have also displayed the noise and accuracy benefit when counts-over-threshold mode data is used in multi-step decomposition versus the more traditional binned mode. The benefit in decomposition performance of the multi-step technique when energy weighting based on material specific CNRs was displayed over when equal bin weighting was used. The importance of spectral correction to overcome detector distortions and object scatter was emphasized by the superior multi-step decomposition performance with spectral correction. Finally, the importance of selective application of the conservation of volume constraint during multi-step decomposition was emphasized.

7.6 Discoveries When Working With Real Data

When working with real data collected from a PCD, we made several changes to our multi-step method from our initial paper [31]. First, the spectral distortions which were only mentioned in the discussion of our initial work and were not modeled into the simulations had to be addressed when working with experimental data. For this reason, we add an additional step in the work flow for spectral correction. The empirical spectral correction technique that we employ is simple and can be applied to data collected in all modes of our Medipix detector. Without spectral correction, a larger mismatch between the measured attenuation of the objects and the basis functions calculated from our analytical simulation tool is expected leading to greater errors in decomposition. Second, because of decreased image quality when subtracting photon counting measurements, we opt to use the data in its raw form without subtraction. This resulted in a slightly more involved method for calculating basis functions for decomposition, but yielded lower noise results for the phantoms studied here. However, further investigation is required to determine whether this strategy will hold when several low contrast materials are of interest such as water, lipid

and protein. Third, when pre-processing our projection data we now filter the data with a bilateral filter rather than a Wiener filter. The bilateral filter provides a good compromise between edge preservation and smoothing and has been adopted by others [26, 41]. Finally, we have found that selective application of the conservation of volume constraint during the solution of soft materials (H2O, ABS plastic and chicken heart muscle) and not during the solution of high contrast materials (I, Gd and HA) yielded the lowest error decompositions. This has also been mentioned by others [6].

7.7 Chapter Summary

In this chapter, experimental validation of our multi-step method was conducted with various multi-material phantoms measured with different detectors and under different experimental conditions. Sufficient projection arc sampling and the benefits of working in counts-over-threshold mode, using optimal CNR weights, employing spectral correction and selectively applying the conservation of volume constraint were presented. Some explanation for performance differences between the multi-material phantom studies were summarized. Finally, some important updates to the multi-step method when moving from synthetic data to experiments were highlighted.

Chapter 8

Conclusions

The idea of performing material decomposition in multiple steps is novel and versatile. We have demonstrated the multi-step method in image domain, but it could also be applied in projection domain. Overall, the PEs, CNRs and NSDs of the multi-step method are similar to other studies [49, 50, 1, 98] and the possibility to decompose up to six materials has been demonstrated through simulated phantoms and five materials through physical phantoms. An anatomical phantom composed of a chicken heart with contrast agents extends the applicability of the technique to realistic *in vitro* specimens. Most other methods that display the ability to decompose six materials, such as the ones by Xue et al. [98] and Ding et al. [24], use complex statistical techniques requiring high computational time. We believe that our simple and robust multi-step decomposition method is computationally efficient and suitable for a range of decomposition problems involving complex imaging tasks with several materials. As multi-energy x-ray detection systems become more common and these systems are outfitted to handle material decomposition problems, we hope that our algorithm will be an attractive choice because of the simplicity of the technique which offers minimal tuning parameters. Combining statistical iterative methods with our multi-step technique has the potential for enhanced results with larger numbers of materials. While the method is shown for data from a photon counting detector, it can be generally applied to data from multi-bin acquisition methods (such as an extension of dual energy imaging) without a photon counting detector as well.

References

[1] Alessio, A. M. and L. R. MacDonald (2013). "Quantitative material characterization from multi-energy photon counting CT." *Med. Phys. 40*(3), 031108.

[2] Alvarez, R. E. and A. Macovski (1976). "Energy-selective reconstructions in x-ray computerized tomography." *Phys. Med. Biol. 21*(5), 733–744.

[3] Astromskas, V., E. N. Gimenez, A. Lohstroh, and N. Tartoni (2016). "Evaluation of polarization effects of e^- collection Schottky CdTe Medipix3RX hybrid pixel detector." *IEEE Trans. Nucl. Sci. 63*(1), 252–258.

[4] Ballabriga, R., J. Alozy, G. Blaj, M. Cambell, M. Fiederle, E. Frojdh, E. H. M. Heijne, X. Llopart, M. Pichotka, S. Procz, L. Tlustos, and W. Wong (2013). "The Medipix3RX: a high resolution, zero dead-time pixel detector readout chip allowing spectroscopic imaging." *J. Instrum. 8*, 1–15.

[5] Barber, R. F., E. Y. Sidky, T. G. Schmidt, and X. Pan (2016). "An algorithm for constrained one-step inversion of spectral CT data." *Phys. Med. Biol. 61*(10), 3784–3818.

[6] Bateman, C. J., D. Knight, B. Brandwacht, J. M. Mahon, J. Healy, R. Panta, R. Aamir, K. R. M. Moghiseh, M. Ramyar, D. Rundle, J. Bennett, N. de Ruiter, D. Smithies, S. T. Bell, R. Doesburg, A. Chernoglazov, V. B. H. Mandalika, M. Walsh, M. Shamshad, M. Anjomrouz, A. Atharifard, L. V. Broeke, S. Bheesette, T. Kirkbride, N. G. Anderson, S. P. Gieseg, T. Woodfield, P. F. Renaud, A. P. H. Butler, and P. H. Butler (2018).

"MARS-MD: rejection based image domain material decomposition." *J. Instrum. 13*(5), 1–14.

[7] Berdikov, V. V., O. I. Grigor'ev, and B. S. Iokhin (1982). "X-ray fluorescence determination of uranium and neighboring elements in solution." *J. Radioanal. Chem. 68*, 181–192.

[8] Brooks, R. (1977). "A quantitative theory of the Houndsfield unit and its application to dual energy scanning." *J. Comput. Assist. Tomogr. 1*(4), 487–493.

[9] Cahn, R. N., B. Cederström, M. Danielsson, A. Hall, M. Lundqvist, and D. Nygren (1999). "Detective quantum efficiency dependence on x-ray energy weighting in mammography." *Med. Phys. 26*(12), 2680–2683.

[10] Cai, C., T. Rodet, S. Legoupil, and A. Mohammad-Djafari (2013). "A full-spectral Bayesian reconstruction approach based on the material decomposition model applied in dual-energy computed tomography." *Med. Phys. 40*(11), 111916.

[11] Campbell, M. (2020). "Medipix3: learn about the Medipix3 collaboration." Retrieved from https://medipix.web.cern.ch/medipix3.

[12] Chantler, C. (1995). "Theoretical form factor, attenuation and scattering tabulation for Z=1-92 from E=1-10 eV to E=0.4-1.0 MeV." *J. Phys. Chem. Ref. Data 24*, 71–643.

[13] Chantler, C. (2000). "Detailed tabulation of atomic form factors, photoelectric absorption and scattering cross section, and mass attenuation coefficients in the vicinity of absorption edges in the soft x-ray (Z = 30-36, Z = 60-89, E = 0.1 keV-10 keV), addressing convergence issues of earlier work." *J. Phys. Chem. Ref. Data 29*(4), 597–1048.

[14] Cho, H.-M., H. Ding, B. P. Ziemer, and S. Molloi (2014). "Energy response calibration of photon-counting detectors using x-ray fluorescence: a feasibility study." *Phys. Med. Biol. 59*(23), 7211–7227.

[15] Choi, J., D. Kang, S. Kang, Y. Sung, and J. C. Ye (2013). "A unified statistical framework for material decomposition using multienergy photon counting x-ray detectors." *Med. Phys. 40*(9), 091913.

[16] Chung, J., J. G. Nagy, and I. Sechopoulos (2010). "Numerical algorithms for polyenergetic digital breast tomosynthesis reconstruction." *SIAM J. Imaging Sci. 3*(1), 135–152.

[17] Clark, D. P. and C. T. Badea (2014). "Spectral diffusion: an algorithm for robust material decomposition of spectral CT data." *Phys. Med. Biol. 59*(21), 6445–6466.

[18] Coleman, T. and Y. Li (1996). "A reflective newton method for minimizing a quadratic function subject to bounds on some of the variables." *SIAM J. Optim. 6*(4), 1040–1058.

[19] Das, M., H. Gifford, J. O'Connor, and S. Glick (2011). "Penalized maximum likelihood reconstruction for improved microcalcification detection in breast tomosynthesis." *IEEE Trans. Med. Imag. 30*(4), 904–914.

[20] Das, M. and Z. Liang (2014). "Approximated transport-of-intensity equation for coded-aperture x-ray phase-contrast imaging." *Opt. Lett. 39*(18), 5395–5398.

[21] Das, M. and Z. Liang (2014). "Spectral x-ray phase contrast imaging for single-shot retrieval of absorption, phase, and differential-phase imagery." *Opt. Lett. 39*(21), 6343–6346.

[22] Ding, H. and S. Molloi (2012). "Image-based spectral distortion correction for photon-counting x-ray detectors." *Med. Phys. 39*(4), 1864–1876.

[23] Ding, H., B. Zhao, P. Baturin, F. Behroozi, and S. Molloi (2014). "Breast tissue decomposition with spectral distortion correction: a postmortem study." *Med. Phys. 41*(10), 101901.

[24] Ding, Q., T. Niu, X. Zhang, and Y. Long (2018). "Image-domain multi-material decomposition for dual-energy CT based on prior information of material images." *Med. Phys. 45*(8), 3614–3626.

[25] Dong, X., T. Niu, and L. Zhu (2014). "Combined iterative reconstruction and image-domain decomposition for dual energy CT using total-variation regularization." *Med. Phys. 41*(5), 051909.

[26] Elad, M. (2002). "On the origin of the bilateral filter and ways to improve it." *IEEE Trans. Image Process. 11*(10), 1141–1151.

[27] Faby, S., S. Kuchenbecker, D. Simons, H. P. Schlemmer, M. Lell, and M. KachelrieB (2014). "CT calibration and dose minimization in image-based material decomposition with energy-selective detectors." presented at SPIE: Medical Imaging, San Diego, 2014. San Diego, CA: SPIE.

[28] Feldkamp, L. A., L. C. Davis, and J. W. Kress (1984). "Practical cone-beam algorithm." *J. Opt. Soc. Am. A 1*(6), 612–619.

[29] Feng, C., Q. Shen, K. Kang, and Y. Xing (2017). "Energy calibration of photon counting detectors using a single monochromatic source." *J. Instrum. 12*(6), 1–12.

[30] Fredette, N., A. Kavuri, and M. Das (2018). "A sensitivity analysis on parameters that affect a multi-step material decomposition for spectral CT." presented at SPIE: Medical Imaging, Houston, 2018. Houston, TX: SPIE.

[31] Fredette, N., A. Kavuri, and M. Das (2019). "Multi-step material decomposition for spectral computed tomography." *Phys. Med. Biol. 64*(14), 1–16.

[32] Fredette, N., C. Lewis, and M. Das (2017). "A multi-step method for material decomposition in spectral computed tomography." presented at SPIE: Medical Imaging, Orlando, 2017. Orlando, FL: SPIE.

[33] Fredette, N., S. Vespucci, and M. Das (2019). "Experimental validation of a multi-step material decomposition for spectral CT." presented at SPIE: Medical Imaging, San Diego, 2019. San Diego, CA: SPIE.

[34] Ge, Y., X. Ji, R. Zhang, K. Li, and G.-H. Chen (2018). "K-edge energy-based calibration method for photon counting detectors." *Phys. Med. Biol. 63*(1), 1–9.

[35] Geet, M. V., R. Swennen, and M. Wevers (2000). "Quantitative analysis of reservoir rocks by microfocus x-ray computerised tomography." *Sediment. Geol. 132*(1-2), 25–36.

[36] Glover, G. H. (1982). "Compton scatter effects in CT reconstructions." *Med. Phys. 9*(6), 860–867.

[37] Granton, P. V., S. I. Pollman, N. L. Ford, M. Drangova, and D. W. Holdsworth (2008). "Implementation of dual- and triple-energy cone-beam micro-CT for postreconstruction material decomposition." *Med. Phys. 35*(11), 5030–5042.

[38] Gursoy, D. and M. Das (2013). "Single-step absorption and phase retrieval with polychromatic x rays using a spectral detector." *Opt. Lett. 38*(9), 1461–1463.

[39] Hanke, R., T. Fuchs, and N. Uhlmann (2008). "X-ray based methods for non-destructive testing and material characterization." *Nucl. Instrum. Methods Phys. Res. A 591*(1), 14–18.

[40] Harding, G. (2004). "X-ray scatter tomography for explosives detection." *Radiat. Phys. Chem. 71*, 869–881.

[41] Holbrook, M., D. P. Clark, and C. T. Badea (2018). "Multiscale dual energy micro-CT for imaging using iodinated and gold nanoparticles." presented at SPIE: Medical Imaging, Houston, 2018. Houston, TX: SPIE.

[42] Jakubek, J., M. Jakubek, M. Platkevic, P. Soukup, D. Turecek, V. Sykora, and D. Vavrik (2014). "Large area pixel detector WIDEPIX with full area sensitivity composed of 100 Timepix assemblies with edgeless sensors." *J. Instrum. 9*(C04018), 1–9.

[43] Jun, K. and S. Yoon (2017). "Alignment solution for CT image reconstruction using fixed point and virtual rotation axis." *Sci. Rep. 7*(41218), 1–11.

[44] Kak, A. C. and M. Slaney (1988). Principles of Computerized Tomographic Imaging. New York: IEEE Press.

[45] Kalluri, K. S., M. Mahd, and S. J. Glick (2013). "Investigation of energy weighting using an energy discriminating photon counting detector for breast CT." *Med. Phys. 40*(8), 081923.

[46] Kappler, S., A. Henning, B. Krauss, F. Schoeck, K. Stierstorfer, T. Weidinger, and T. Flohr (2013). "Multi-energy performance of a research prototype CT scanner with small-pixel counting detector." presented at SPIE: Medical Imaging, Lake Buena Vista, 2013. Lake Buena Vista, FL: SPIE.

[47] Klein, O. and T. Nishina (1929). "Uber die streuung von strahlung durch freie elektronen nach der neuen relativistischen quantendynamik von dirac." *Zeitschrift fur Physik 52*(11-12), 853–868.

[48] Koenig, T., M. Zuber, E. Hamann, A. Cecilia, R. Ballabriga, M. Campbell, M. Ruat, L. Tlustos, A. Fauler, M. Fiederle, and T. Baumback (2014). "How spectroscopic x-ray imaging benefits from inter-pixel communication." *Phys. Med. Biol. 59*(20), 6195–6213.

[49] Le, H. Q. and S. Molloi (2011). "Least squares parameter estimation methods for material decomposition with energy discriminating detectors." *Med. Phys. 38*(1), 245–255.

[50] Le, H. Q. and S. Molloi (2011). "Segmentation and quantification of materials with energy discriminating computed tomography: a phantom study." *Med. Phys. 38*(1), 228–237.

[51] Lee, S., Y. Choi, and H. Kim (2014). "Quantitative material decomposition using spectral computed tomography with an energy-resolved photon-counting detector." *Phys. Med. Biol. 59*(18), 5457–5482.

[52] Lehmann, L. A., R. E. Alvarez, A. Macovski, W. R. Brody, N. J. Pelc, S. J. Riederer,

and A. L. Hall (1981). "Generalized image combinations in dual KVP digital radiography." *Med. Phys. 8*(5), 659–667.

[53] Li, T. and H. Feng (2009). "Comparison of different analytical edge spread function models for MTF calculation using curve-fitting." presented at SPIE: Medical Imaging, Lake Buena Vista, 2009. Lake Buena Vista, FL: SPIE.

[54] Li, Z., S. Leng, L. Yu, Z. Yu, and C. H. McCollough (2015). "Image-based material decomposition with a general volume constraint for photon-counting CT." presented at SPIE: Medical Imaging, Orlando, 2015. Orlando, FL: SPIE.

[55] Liu, X., L. Yu, A. Primak, and C. McCollough (2009). "Quantitative imaging of element composition and mass fraction using dual-energy CT: three-material decomposition." *Med. Phys. 36*(5), 1602–1609.

[56] Long, Y. and J. A. Fessler (2014). "Multi-material decomposition using statistical image reconstruction for spectral CT." *IEEE Trans. Med. Imag. 33*(8), 1614–1626.

[57] MaaB, C., M. Baer, and M. KachelrieB (2009). "Image-based dual energy CT using optimized precorrection functions: a practical new approach of material decomposition in image domain." *Med. Phys. 36*(8), 3818–3829.

[58] MaaB, N., S. Sawall, M. Knaup, and M. KachelrieB (2011). "Empirical multiple energy calibration (EMEC) for material-selective CT." presented at IEEE: Nuclear Science Symposium and Medical Imaging Conference, Valencia, 2011. Valencia, Spain: IEEE Press.

[59] Maier, A., S. Steidl, V. Christlein, and J. Hornegger (2018). Medical Imaging Systems: An Introductory Guide. Cham: Springer.

[60] McCollough, C. H., S. Leng, L. Yu, and J. G. Fletcher (2015). "Dual- and multi-energy CT: principles, technical approaches, and clinical applications." *Radiology 276*(3), 637–653.

[61] McCullough, E. C., H. L. Baker, O. W. Houser, and D. F. Reese (1974). "An evaluation of the quantitative and radiation features of a scanning x-ray traverse axial tomograph: the EMI scanner." *Radiot. Phys. 111*(3), 709–715.

[62] McCullough, E. C. (1975). "Photon attenuation in computed tomography." *Med. Phys. 2*(6), 307–320.

[63] McIntosh, K. G., S. D. Reilly, and G. J. Havrilla (2015). "Determination of plutonium in spent nuclear fuel using high resolution x-ray." *Spectrochim. Acta B 110*, 91–95.

[64] Mendonca, P. R. S., P. Lamb, and D. V. Sahani (2014). "A flexible method for multi-material decomposition of dual-energy CT images." *IEEE Trans. Med. Imag. 33*(1), 99–116.

[65] Niu, T., X. Dong, M. Petrongolo, and L. Zhu (2014). "Iterative image-domain decomposition for dual-energy CT." *Med. Phys. 41*(4), 041901.

[66] Panta, R. K., M. F. Walsh, S. T. Bell, N. G. Anderson, A. P. Butler, and P. H. Butler (2015). "Energy calibration of the pixels of spectral x-ray detectors." *IEEE Trans. Med. Imag. 34*(3), 697–706.

[67] Paziresh, M., A. M. Kingston, S. J. Latham, W. K. Fullagar, and G. M. Myers (2016). "Tomography of atomic number and density of materials using dual-energy imaging and the Alvarez and Macovski attenuation model." *J. Appl. Phys. 119*(21), 214901.

[68] Persson, M., B. Huber, S. Karlsson, X. Liu, H. Chen, C. Xu, M. Yveborg, H. Bornefalk, and M. Danielsson (2014). "Energy-resolving CT imaging with a photon-counting silicon-strip detector." *Phys. Med. Biol. 59*, 6709–6727.

[69] Pietsch, P. and V. Wood (2017). "X-ray tomography for lithium ion battery research: a practical guide." *Annu. Rev. Mater. 47*(1), 451–479.

[70] Ren, L., S. Tao, C. H. McCollough, and L. Yu (2019). "Material decomposition in

photon-counting-detector CT: threshold or bin images?" presented at SPIE: Medical Imaging, San Diego, 2019. San Diego, CA: SPIE.

[71] Ronaldson, J. P., R. Zainon, N. J. A. Scott, S. P. Gieseg, A. P. Bulter, P. H. Butler, and N. G. Anderson (2012). "Toward quantifying the composition of soft tissues by spectral CT with Medipix3." *Med. Phys. 39*(11), 6847–6857.

[72] Samei, E., N. T. Ranger, J. T. Dobbins III, and Y. Chen (2006). "Intercomparison of methods for image quality characterization. I. modulation transfer function" *Med. Phys. 33*(5), 1454–1465.

[73] Sarnelli, A., A. Taibi, A. Tuffanelli, G. Baldazzi, D. Bollini, A. E. C. Rodriguez, M. Gombia, F. Prino, L. Ramello, E. Tomassi, and M. Gambaccini (2004). "K-edge digital subtraction imaging based on a dichromatic and compact x-ray source." *Phys. Med. Biol. 49*(14), 3291–3305.

[74] Schmidt, T. G. (2009). "Optimal image-based weighting for energy-resolved CT." *Med. Phys. 36*(7), 3018–3027.

[75] Schmidt, T. G. (2010). "CT energy weighting in the presence of scatter and limited energy resolution." *Med. Phys. 37*(3), 1056–1067.

[76] Schmidt, T. G. and F. Petkas (2011). "Region-of-interest material decomposition from truncated energy-resolved CT." *Med. Phys. 38*(10), 5657–5666.

[77] Seibert, J. A. and J. M. Boone (2005). "X-ray imaging physics for nuclear medicine technologists. Part 2: x-ray interactions and image formation." *J. Nucl. Med. Technol. 33*(1), 3–18.

[78] Shikhaliev, P. M. (2012). "Photon counting spectral CT: improved material decomposition with k-edge-filtered x-rays." *Phys. Med. Biol. 57*(6), 1595–1615.

[79] Shikhaliev, P. M. (2015). "Soft tissue imaging with photon counting spectroscopic CT." *Phys. Med. Biol. 60*(6), 2453–2474.

[80] Shikhaliev, P. M. (2018a). "Large-scale MV CT for cargo imaging: a feasibility study." *Nucl. Instrum. Methods Phys. Res. A 904*, 35–43.

[81] Shikhaliev, P. M. (2018b). "Megavoltage cargo radiography with dual energy material decomposition." *Nucl. Instrum. Methods Phys. Res. A 882*, 158–168.

[82] Siewerdsen, J. H., L. E. Antonuk, Y. El-Mohri, J. Yorkston, W. Huang, J. M. Boudry, and I. A. Cunningham (1997). "Empirical and theoretical investigation of the noise performance of indirect detection, active matrix flat-panel imagers (AMFPIs) for diagnostic radiology." *Med. Phys. 24*(1), 71–89.

[83] Siewerdsen, J. H., A. M. Waese, D. J. Moseley, S. Richard, and D. A. Jaffray (2004). "Spektr: a computational tool for x-ray spectral analysis and imaging system optimization." *Med. Phys. 31*(11), 3057–3067.

[84] Singh, S. and M. Singh (2003). "Explosives detection systems (EDS) for aviation security." *Signal Process. 83*, 31–55.

[85] Skellam, J. G. (1946). "The frequency distribution of the difference between two Poisson variates belonging to different populations." *Journ. Roy. Statist. Soc. 109*(3), 296.

[86] Sprawls, P. (1993). Physical Principles of Medical Imaging. Gaithersburg: Aspen Publishers.

[87] Stark, G. (2020). "Xray: radiation beam." Retrieved from https://www.britannica.com/science/X-ray.

[88] Taba, S. T., T. E. Gureyev, M. Alakhras, S. Lewis, D. Lockie, and P. C. Brennan (2018). "X-ray phase-contrast technology in breast imaging: principles, options, and clinical application." *Am. J. Roentgenol. 211*(1), 133–145.

[89] Taguchi, K. and J. S. Iwanczyk (2013). "Vision 20/20: single photon counting x-ray detectors in medical imaging." *Med. Phys. 40*(10), 100901.

[90] Torrico, R., A. Kavuri, C. Lewis, and M. Das (2019). "Single-exposure contrast enhanced spectral mammography." presented at SPIE: Medical Imaging, San Diego, 2019. San Diego, CA: SPIE.

[91] van Aarle, W., W. J. Palenstijn, J. Cant, E. Janssens, F. Bleichrodt, A. Dabravolski, J. De Beenhouwer, K. J. Batenburg and J. Sijbers (2016). "Fast and flexible x-ray tomography using the ASTRA toolbox." *Opt. Express 24*(22), 25129-25147.

[92] Vazquez, I., N. Fredette, and M. Das (2019). "Quantitative phase retrieval of heterogeneous samples from spectral x-ray measurements." presented at SPIE: Medical Imaging, San Diego, 2019. San Diego, CA: SPIE.

[93] Vedula, A., S. Glick, and X. Gong (2003). "Computer simulation of CT mammography using a flat-panel imager." presented at SPIE: Medical Imaging, San Diego, 2003. San Diego, CA: SPIE.

[94] Vespucci, S. and M. Das (2018). "Spectrally varying spatial frequency properties of a small pixel photon counting detector." presented at SPIE: Medical Imaging, Houston, 2018. Houston, TX: SPIE.

[95] Vespucci, S., C. S. Park, R. Torrico, and M. Das (2019). "Robust energy calibration technique for photon counting spectral detectors." *IEEE Trans. Med. Imag. 38*(4), 968–978.

[96] Wang, X., D. Meier, K. Taguchi, D. J. Wagenaar, B. E. Patt, and E. C. Frey (2011). "Material separation in x-ray CT with energy resolved photon-counting detectors." *Med. Phys. 38*(3), 1534–1546.

[97] White, D., J. Booz., R. Griffith, J. Spokas, and I. Wilson (1989). "Tissue substitutes in radiation dosimetry and measurement." Technical Report ICRU-44, International Commission on Radiation Units and Measurements, Bethesda, MD.

[98] Xue, Y., R. Ruan, X. Hu, Y. Kuang, J. Wang, Y. Long, and T. Niu (2017). "Statistical

image-domain multimaterial decomposition for dual-energy CT." *Med. Phys. 44*(3), 886–901.

[99] Yu, L., X. Liu, and C. McCollough (2009). "Pre-reconstruction three-material decomposition in dual-energy CT." presented at SPIE: Medical Imaging, Lake Buena Vista, 2009. Lake Buena Vista, FL: SPIE.

[100] Zamyatin, A. A., A. Natarajan, and Y. Zou (2009). "Advanced material separation technique based on dual energy CT scanning." presented at SPIE: Medical Imaging, Lake Buena Vista, 2009. Lake Buena Vista, FL: SPIE.

[101] Zbijewski, W., G. J. Gang, J. Xu, A. S. Wang, J. W. Stayman, K. Taguchi, J. A. Carrino, and J. H. Siewerdsen (2014). "Dual-energy cone-beam CT with a flat-panel detector: effect of reconstruction algorithm on material classification." *Med. Phys. 41*(2), 021908.

[102] Zhu, Y., N. Samadi, M. Martinson, B. Bassey, Z. Wei, G. Belev, and D. Chapman (2014). "Spectral K-edge subtraction imaging." *Phys. Med. Biol. 59*(10), 2485–2503.